Low-Energy Event Physics with the T2K Neutrino Detector SuperFGD and Global Neutrino Data Fitting with GAMBIT

Chien Lin

Blackett Laboratory

Imperial College London

A thesis submitted to Imperial College London for the degree of Doctor of Philosophy

2024

Abstract

The field of neutrino oscillation physics has yielded numerous significant results in recent decades. The Japan-based long-baseline accelerator neutrino oscillation Tokai-to-Kamioka (T2K) experiment, renowned for its contributions to accelerator neutrino oscillation studies, is undergoing several upgrades to further advance high-impact measurements. Among the newly constructed subdetectors of the T2K off-axis near detector ND280 is the Super Fine-Grained Detector (SuperFGD), which was installed in 2023. It is a high-resolution particle tracker that is made up of approximately two million plastic scintillating cubes. Its novel design allows the detector to measure neutrino interactions with high precision, an essential key to reducing uncertainties of current and future neutrino experiments.

This thesis includes a brief summary of the SuperFGD design and the related calibration tasks. In particular, the charge and pedestal calibration for the Multi-Pixel Photon Counters (MPPCs) are described in detail. A neural network based on a Transformer architecture developed for general voxelised 3D detectors was utilised to increase calibration tolerance.

Finally, this thesis presents the development of a Standard Model three-neutrino oscillation global fit study within the GAMBIT software framework, where the incorporation of the likelihood functions of the NOνA, MINOS, and KamLAND experiments are detailed. Their validation results demonstrate good agreement with the experimental counterparts, but the limited public data and experiment information negatively affect the accuracy of the implementations. A preliminary scan, which included eight neutrino oscillation experiments that covered a wide range of measurement technologies, was also performed. In general, the early results are consistent with the existing neutrino global fits, and some noticeable deviations are discussed.

Declaration

This thesis represents my own work, built upon the contributions and efforts of many individuals over time. While the analyses and figures presented are my own, any external sources are appropriately cited. This thesis also includes collaborative efforts from larger groups, with all figures produced by me unless otherwise noted.

Chapters 2 and 3 provide a summary of the current state of neutrino physics and the T2K experiment. These chapters draw on the work of many physicists, with all contributions appropriately cited. They include detailed descriptions of the relevant neutrino experiments, as well as the theory and history behind neutrino oscillation.

Chapter 4 includes a detailed description of a new ND280 subdetector, the SuperFGD. Everything presented is the collaborative result of many T2K members, except the work on the SuperFGD charge and pedestal calibration in Section 4.2 and Section 4.3.1. The calibration methods, partly improved from those used by the SuperFGD prototype, and the software package that contains them were developed by me.

My work described in Chapter 5 is an extension work that utilises a machine learning algorithm developed by the SuperFGD reconstruction group based on the Transformer architecture. It includes the use of a dataset specific for the SuperFGD detector and a modified training method to enhance tolerance to calibration inaccuracies.

In Chapter 6, although I was not involved in the neutrino experiments described, I utilised the information, data, and results from these experiments to implement likelihood functions within the GAMBIT framework. This framework, developed by the GAMBIT collaboration, enabled the integration of these experimental outcomes. Additionally, I performed the joint fits and analyses in the chapter, but they also reflect contributions from various members of the GAMBIT collaboration.

I hereby certify that the thesis presented here is solely my own work, except where I have explicitly acknowledged the contributions of others. All material that is not my own work has been properly attributed. I also certify that the thesis has not been submitted for any other degree or purpose.

Copyright Declaration

"The copyright of this thesis rests with the author. Unless otherwise indicated, its contents are licensed under a Creative Commons Attribution-Non Commercial 4.0 International Licence (CC BY-NC). Under this licence, you may copy and redistribute the material in any medium or format. You may also create and distribute modified versions of the work. This is on the condition that: you credit the author and do not use it, or any derivative works, for a commercial purpose.

When reusing or sharing this work, ensure you make the licence terms clear to others by naming the licence and linking to the licence text. Where a work has been adapted, you should indicate that the work has been changed and describe those changes. Please seek permission from the copyright holder for uses of this work that are not included in this licence or permitted under UK Copyright Law."

Chien Lin

Acknowledgements

First and foremost, I would like to express my sincere gratitude to my supervisor, Prof. Yoshi Uchida, for his trust and confidence (and some might say a gamble), brought me into the group despite the mediocre-at-best undergraduate marks. His support, guidance, and encouragement have also been invaluable throughout my PhD journey.

I am also profoundly grateful to the many colleagues at the Imperial neutrino group, the T2K collaboration, and the GAMBIT neutrino workgroup, for the countless stimulating discussions and input. The technical assistance and expertise have been indispensable to me during the course of the PhD. In particular, I am indebted to Dr. Wilf Shorrock, Dr. Anders Kvellestad, Dr. Per Jonsson, Prof. Matsubara Tsunayuki, Dr. Tanigawa Hikaru, Dr. Tristan Doyle, Dr. Matthew Lawe, and Dr. Saúl Alonso-Monsalve for their collaboration, support, and the many insightful discussions we shared, which have greatly improved the quality of this research. Many of the results shown in this thesis were produced using the Cambridge Service for Data Driven Discovery (CSD3) and the EuroHPC supercomputer LUMI, for that I am thankful.

On a personal note, many thanks to Weijun, Jake, Koustubh, Patrick, Ichige-sensei, and many other friends I have met in London and Tokai; they have made these years stellar. And finally to my family, thank you for being my rock. I could not have done this without you, and you have made this life a reality.

Contents

Abstract i

Declaration ii

Acknowledgements iv

1 Introduction 1

2 Neutrino Physics 4

2.1 A Brief History of Neutrino Physics . . . 4

2.1.1 Discovery of the Three Types of Neutrino . . . 4

2.1.2 Neutrino Phenomena Outside the Standard Model . . . 5

2.2 Neutrino Oscillations . . . 6

2.2.1 The PMNS Matrix . . . 6

2.2.2 Three-Neutrino Oscillations in Vacuum . . . 7

2.3 Open Questions . . . 8

3 The T2K Neutrino Oscillation Experiment 10

3.1 The T2K Experiment . . . 10

3.2 The T2K Neutrino Beam . . . 11

3.3 The ND280 Near Detector after the 2020 Upgrade . . . 12

3.3.1 Components of ND280 . . . 12

3.4 The Super-Kamiokande Detector as the T2K Far Detector . . . 16

3.5 T2K Oscillation Ananlysis . . . 18

4 The Super Fine-Grained Detector 20

4.1 SuperFGD Components . . . 21

4.1.1 Plastic Scintillator Cubes . . . 21

4.1.2 Wavelength-Shifting (WLS) Fibres . . . 21

4.1.3 Multi-Pixel Photon Counters (MPPCs) . . . 21

4.1.4 SuperFGD Read-Out Electronics . . . 23

4.1.5 LED Calibration System . . . 24

4.2 SuperFGD Charge Calibration . . . 26

4.2.1 Extracting HG Calibration Constants . . . 27
4.2.2 Extracting Pedestal Calibration Constant . . . 29
4.2.3 Extracting LG Calibration Constants . . . 32
4.2.4 Extracting ToT Calibration Constants . . . 33
4.3 Other SuperFGD Calibration Tasks . . . 35
4.3.1 High-Voltage Trimming . . . 35
4.3.2 Cube-Related Calibration . . . 37
4.3.3 Fibre-Related Calibration . . . 37
4.3.4 Timing Calibration . . . 38
4.3.5 Detector Geometry Calibration . . . 38

5 Particle Activity at the Neutrino Interaction Vertex in the SuperFGD 39
5.1 Transformer Neural Network . . . 40
5.2 Vertex Activity Fitting Utilising Transformer Network . . . 42
5.2.1 The Transformer Neural Network Design . . . 42
5.2.2 A New Training Process . . . 44
5.3 Results . . . 47

6 Neutrino Oscillation Global Study within GAMBIT 51
6.1 A Brief Review of the Current Neutrino Oscillation Global Fit Studies . . . 52
6.2 The GAMBIT Package and the `NeutrinoBit` Module . . . 53
6.3 Methodology . . . 54
6.3.1 General Procedure . . . 54
6.3.2 Likelihood Method . . . 55
6.3.3 Scanner . . . 55
6.4 The NOνA Likelihood Functions in GAMBIT . . . 57
6.4.1 Reconstruction Functions . . . 60
6.4.2 Efficiency Functions . . . 60
6.4.3 Neutrino Interaction and Cross-sections . . . 61
6.4.4 Neutrino Oscillation Probability Calculations . . . 62
6.4.5 ν_μ and ν_e samples . . . 62
6.4.6 Validation of NOνA Likelihood Functions . . . 63
6.5 The MINOS Likelihood Functions in GAMBIT . . . 66
6.5.1 GAMBIT Prediction of MINOS Neutrino Energy Spectra . . . 67
6.5.2 Validation of MINOS Likelihood Functions . . . 68
6.6 The KamLAND Likelihood Functions in GAMBIT . . . 70
6.6.1 Neutrino Fluxes at KamLAND . . . 71
6.6.2 Reconstruction Functions . . . 73
6.6.3 Efficiency Function . . . 73
6.6.4 IBD Cross-sections . . . 73

6.6.5 Validation of KamLAND Likelihood Functions 74
6.7 Preliminary Global Fit Results 76
6.7.1 Comparing Best-fit $\sin^2(\theta_{12})$ 80
6.7.2 Comparing Best-fit $\sin^2(\theta_{13})$ 81
6.7.3 Comparing Best-fit $\sin^2(\theta_{23})$ 82
6.7.4 Comparing Best-fit Δm^2_{21} 83
6.7.5 Comparing Best-fit Δm^2_{32} 84
6.7.6 Comparing Best-fit δ_{CP} 85
6.8 A Discussion on Data Sharing 86

7 Conclusion **89**

A Additional Materials for the GAMBIT Neutrino Oscillation Project **92**
A.1 NOνA selection efficiency functions 92

Bibliography **94**

List of Figures

2.1 A chart [17] showing the elementary particles predicted by the Standard Model 5

3.1 The T2K experiment beamline. A beam of ν_μ produced by a proton accelerator at the Japan Proton Accelerator Research Complex (J-PARC) is directed at the Super-K detector 295 kilometres down the beamline. The near detector suite ND280 is located 280 metres away from the neutrino source, providing valuable measurements about the neutrino beam. 10

3.2 An illustration of the T2K neutrino beamline [58] 11

3.3 The T2K neutrino flux predictions at the Super-K detector for the Forward Horn Current (FHC, left) and Reverse Horn Current (RHC, right) modes [60, 61]. 11

3.4 T2K detectors are located 2.5° off-axis, achieving a neutrino spectrum that peaks at 600 MeV, coninciding with an oscillation minimum. [62] 12

3.5 An exploded view of the ND280 detector suite prior to the 2020 Upgrade (left), showing the constituent subdetectors. The ν_μ beam enters from the left of the figure along the z-axis. The detector coordinate system is right-handed, as shown by the origin at the geographical centre, which lies near the downstream end of the first TPC. The P0D was replaced by a group of new detectors (right) as part of the Upgrade [7], and the installation was completed in 2024. 13

3.6 An example event display showing particle tracks in the three TPCs and the two FGDs [70] . 14

3.7 A schematic diagram of a TPC [71]. The detector volume is separated by the central cathode into two mirrored regions. With the two anodes installed at each side of the detector, two mirrored electric fields are generated, pointing from the side anodes at the central cathode. The direction of one electric field is illustrated in the diagram. 14

3.8 The expected selection efficiency for μ_ν charged-current (CC) events originating from different detectors as a function of the angle between the product muon and the beam axis [7]. The ν_μ CC event selection efficiency in SuperFGD is significantly improved, particularly at higher angles. 16

3.9 A schematic diagram of the Super-Kamiokande detector and its location underground in the Kamioka mine (left, [80]). A photo showing the PMTs mounted on the inner wall of the Super-K detector during maintenance (right, [81]). 17

3.10 Super-K utilises a likelihood-based particle identification algorithm to distinguish between a μ-like candidate and a e-like candidate [3]. Visually, a μ-ring is sharper because muons are less prone to scattering in water. 18

4.1 A 3D concept model of a $19 \times 6 \times 13$ cube segment of the SuperFGD [7]. A zoom-in view of a cube, including the WLS fibres, can be seen on the right. 20
4.2 A photo showing a SuperFGD cube and three WLS fibres, one threading through each orthogonal holes. 21
4.3 The left plot shows the normalised absorption and emission spectra of the WLS fibres [85] and the right plot shows the photon detection efficiency, defined as the ratio of the detected photons to the incident photons, of the SuperFGD MPPC (S13360-1325PE, [86]). Note that the POPOP emission peak wavelength at ~ 430 nm roughly coincides with the Y-11 absorption spectrum peak, and the Y-11 emission wavelength is close to the MPPC efficiency peak. . . . 22
4.4 An MPPC-PCB containing an 8×8 array of MPPCs [87]. 22
4.5 Left photo showing the side panel of the SuperFGD detector. The bottom black square shows 64 WLS couplings (three of which are shown in the right photo [88]) pinning a thin black elastic foam to the red detector panel. The foam will ensure good optical contact with the 64 MPPCs mounted on an MPPC-PCB, as shown by the top black square. Note the protruding white fibres are fishing lines, which were used as placeholders that provided structural stability, waiting to be replaced by WLS fibres. 23
4.6 A diagram showing the hierarchical structure of the SuperFGD electronics. A Master Clock Board (MCB) controls 16 Optical Concentrator Boards (OCBs), and each OCB connects to 14 Front-End Boards (FEBs), which contains eight Cherenkov Imaging Telescope Integrated Read-Out Chips (CITIROCs). Two CITIROCs are required to process one MPPC-PCB, each contains 64 MPPC channels. 24
4.7 The three read-out paths of the CITIROC [90]. The fast shaper (FSH) can be configured to either the LG or the HG path. 24
4.8 An illustration of the SuperFGD LED calibration system [91]. Each fibre is paired with a LED diffuser notch that is etched directly onto the LGP. 25
4.9 A comparison showing the effect of the diffuser layer on the LGP light [92]. The diffuser increases the tolerance on the horizontal WLS fibre displacement. 25
4.10 An illustration of a mock finger plot with a gain of $G = 70$ ADC/p.e. The pedestal (zero-p.e. peak) is, in general, not visible in a SuperFGD MPPC finger plot due to the threshold effect. 27
4.11 An example of a fit result using the 'multi-peak' method on a typical LED calibration finger plot. The last three peaks are discarded and not used in the gain fitting, according to an algorithm that takes the fit quality and the spacing between neightbouring peaks into account. 28
4.12 A plot showing a linear fit to the 'peak number-ADC' plot. The slope of the linear function is the gain (ADC/p.e.) of the channel. The errorbars are included but too small to be seen. . 28
4.13 A plot showing a shifted sampler segment. When the peaks align, the correlation between the sampler and the original finger plot is high. Note the first two peaks are affected by the threshold and are therefore discarded. 29

4.14 The autocorrelation of the finger plot in Figure 4.13. Since the shift is of the same scale as the finger plot (HG ADC unit), the spacing between the peaks provides a measure of the gain. Note, the process also enhances the small peaks in the high ADC region. 30
4.15 A demonstration of the pedestal search algorithm. By varying the HG setting (HG43, HG47, etc.), one produces finger plots of different gains, which can be seen by the change of slope over different HG settings. Since the pedestal position is not affected by the gain setting, the point at which all lines converge should correspond to the location of the pedestal. 30
4.16 A flowchart explaining the pedestal search algorithm. The algorithm returns the best possible p.e. number corresponding to the first peak of the target finger plot, where the configuration minimises the spread of the y-intercepts. 31
4.17 The HG and LG ADC readings of each hit on a channel, as well as the linear function that relates the LG and HG values, are plotted. The parameters of the linear function can be used to convert a LG measurment to HG. The non-linear region at the higher HG ADC region is a result of saturation. The data shown here were collected from the SuperFGD prototype beam test at CERN [90]. 32
4.18 The 1% non-linearity points (marked as magenta crosses) of different gain settings, above which the non-linearity of ADC measurements responding to the injected charge is larger than 1% [97]. Each line shows the response of HG or LG measurement to the injected charges provided by an external generator, given a fixed gain setting. The unit of the charge injected was converted to p.e. for the convenience of reading. The bounds of the unsaturated region is defined according to the result. 33
4.19 An example result of a ToT calibration using two separate calibration routes [90] used in the SuperFGD prototype beam test. The method fits each distribution with a polynomial of degree five, and it is less effective at calibrating the high HG and low LG regions. The method also generates a large number of calibration constants, potentially causing a storage problem in the long run. 34
4.20 An example of a ToT vs (HG & LG) plot using the SuperFGD prototype data. The blue region contains hits whose HG and LG are averaged, weighted by the respective resolutions. The green region combines HG and LG readings similar to the blue region, but the weight of HG is continuously reduced to zero as HG increases. The red region contains only the LG readings. Note the noisy events distributed across ToT < 7 is a result of the miss-tagging of timing information, a firmware bug unique to the prototype data which was fixed in the later firmware releases. 35
4.21 The HG gain responds to the change of operating voltage linearly with the typical gain range created by temperature fluctuation. The data points on the left side of the figure show inaccurate results due to the unrealistic V_{op} setting. 36
4.22 A comparison between G_{HG} distributions before and after the HV trimming. The target gain is set to 15 ADC/p.e. in this example. 36

5.1 A CC0π event candidate inside the ND280. It is likely an event where a muon neutrino (track invisible) entering from the left interacts with the SuperFGD (the magenta box on the left) and produces a long muon track and a shorter proton track. 39
5.2 An attention heat map shown in [103]. When generating 'zone économique européenne', the language model has its attention non-monotonically on 'European Economic Area', shown by the non-diagonal appearance of the heat map, and is able to correctly identify the word order and gender. 41
5.3 A possible scenario illustrating the improvement of Adam compared to the classic SGD. The two optimisers initially start at the same point in a 2D parameter space (marked with a black star). Each line segment denotes one algorithm iteration. The momentum feature helps the Adam optimiser converge onto the global minimum (marked with a red star) more efficiently. 43
5.4 The workflow of the vertex activity neural network [107]. The neural network takes VA images as input and predicts the vertex positions and proton kinematic variables iteratively. 44
5.5 Short proton track kinetic energy (left) and directional reconstruction (right) accuracy of the Transformer neural network [107]. The results show that the Transformer network performs well in reconstructing proton tracks that are difficult to do with other conventional methods. 45
5.6 A schematic diagram [113] showing the process chain of the ND280 software suite. Two main purposes of the suite are to process *Data* (starting from the MIDAS data) and to generate *Monte Carlo events* (starting from 'Neutrino Interaction Generators'), the output of which is compared and studied. 46
5.7 2D histograms showing the true vs reconstructed vertex positions (in all three orthogonal directions), produced by the two Transformer models. The mean differences between the true and the reconstructed coordinates are included. The apparent boundaries at ± 5 mm are caused by the physical separations between cubes. 47
5.8 Confusion matrices for reconstructing the number of protons in each event. Configuration (b) has a slightly enhanced ability to determine the number of protons in each event. 48
5.9 The comparison of KE fractional errors, defined as $\frac{\mathrm{KE_{reco}}-\mathrm{KE_{true}}}{\mathrm{KE_{true}}}$, achieved by the two different Transformer models. Only events with truly one proton were included. Configuration (b) produced more accurate results. The error bars represent $\pm 1\sigma$ intervals. 49
5.10 The comparison of KE fractional errors, defined as $\frac{\mathrm{KE_{reco}}-\mathrm{KE_{true}}}{\mathrm{KE_{true}}}$, achieved by the two different Transformer models. All possible numbers of protons per event (1–5) were included. Configuration (b) produced more accurate results. The error bars represent $\pm 1\sigma$ intervals. . . 49
5.11 2D histograms of the true vs reconstructed total proton KE for each event 50
5.12 2D histograms showing true vs reconstructed initial track direction. The mean differences of the angles θ and ϕ are included. 50

6.1 The hierarchical structure of the GAMBIT software package 54
6.2 The NOνA Far Detector (left [139]) and Near Detector (right [140]). The two liquid scintillator detectors are separated by a distance of 810 km. 57

6.3 The NOνA FD neutrino flux predictions for the Forward Horn Current (left) and Reverse Horn Current (right) modes [141]. 58
6.4 The ν_μ selection efficiency at the NOνA FD 61
6.5 Plots comparing the 1σ and 3σ C.L. contours produced by NOνA [114] and GAMBIT, assuming normal mass ordering. 63
6.6 Plots comparing the 1σ and 3σ C.L. contours produced by NOνA [114] and GAMBIT, assuming inverted mass ordering. 64
6.7 The GAMBIT and NOνA predicted FD neutrino energy spectra at their respective best-fit parameters. The peripheral samples are shown as rates and without energy scale. 65
6.8 Images of the far detector (left, [151]) and the near detector (right, [152]) of the MINOS experiment. The magnetised steel-plastic far detector with a length of 30 m and a diameter of 8 m was located 735 km away from the neutrino beam source and 705 m underground inside the Soudan Underground mine. The near detector, using a similar technology, sat a few hundred metres downstream from the neutrino source at Fermilab. 66
6.9 The on-axis setup of the MINOS detectors produced a much broader and higher energy spectrum compared to the NOνA off-axis design [153]. 67
6.10 A two-flavour comparison between the GAMBIT and MINOS [133] 2D contours. For both results, the θ_{13} was a free parameter without an external constraint. Note, the GAMBIT result only includes the $\nu_\mu \to \nu_\mu$ channel. 68
6.11 2D contour comparisons between GAMBIT and MINOS [154] in three-flavour, where the external constraint $\sin^2(\theta_{13}) = 0.0242 \pm 0.0025$ based on a weighted average of the results from the Daya-Bay, RENO, and Double Chooz experiments was applied. Note, the GAMBIT result only includes the $\nu_\mu \to \nu_\mu$ channel. 69
6.12 Comparison of GAMBIT and MINOS [133] spectra at their respective best-fit points 69
6.13 A schematic diagram of the KamLAND detector [24] 70
6.14 The KamLAND selection efficiency function digitised from [128]. The data points close to the energy threshold were added for interpolation. 73
6.15 The IBD total cross-section used in the KamLAND likelihood functions. 74
6.16 The 1σ and 3σ C.L. contours set by GAMBIT and KamLAND [128]. A noticeable shift in the high Δm^2_{21} direction is present, but size is small. 74
6.17 The unoscillated (left) and oscillated (right) prompt energy spectra predicted by GAMBIT and KamLAND, using the respective best-fit parameter values. The GAMBIT predictions are consistent with the KamLAND results and fit well with the KamLAND observation. 75
6.18 Two-dimensional 1σ, 2σ, and 3σ C.L. contours for the neutrino oscillation parameters within GAMBIT, assuming normal mass ordering 77
6.19 Two-dimensional 1σ, 2σ, and 3σ C.L. contours for the neutrino oscillation parameters within GAMBIT, assuming inverted mass ordering 78

6.20 Comparison of the best-fit values and 1σ C.L. for $\sin^2(\theta_{12})$ by GAMBIT (red), the dominant experiments (orange, reference listed in Table 6.2), and global fits (blue, [45, 119, 46, 47]), assuming NO. 80
6.21 Comparison of the best-fit values and 1σ C.L. for $\sin^2(\theta_{13})$ by GAMBIT (red), the dominant experiment (orange, reference listed in Table 6.2), and global fits (blue, [45, 119, 46, 47]), assuming NO. 81
6.22 Comparison of the best-fit values, 1σ (coloured), and 2σ (black) C.L. for $\sin^2(\theta_{23})$ by GAMBIT (red), the dominant experiments (orange, reference listed in Table 6.2 except T2K for which the values are sourced from [166] for the T2K-only values), and global fits (blue, [45, 119, 46, 47]), assuming NO. 82
6.23 Comparison of the best-fit values and 1σ C.L. for Δm^2_{21} by GAMBIT (red), the dominant experiment (orange, reference listed in Table 6.2), and global fits (blue, [45, 119, 46, 47]), assuming NO. 83
6.24 Comparison of the best-fit values and 1σ C.L. for Δm^2_{32} by GAMBIT (red), the dominant experiments (orange, reference listed in Table 6.2 except T2K for which the values are sourced from [166] for the T2K-only values), and global fits (blue, [45, 119, 46, 47]), and global fits (blue, [45, 119, 46, 47]), assuming NO. 84
6.25 Comparison of the best-fit values, 1σ (coloured), and 2σ (black) C.L. for $\delta_{\rm CP}$ by GAMBIT (red), the dominant experiments (orange, reference listed in Table 6.2 except T2K for which the values are sourced from [166] for the T2K-only values), and global fits (blue, [45, 119, 46, 47]), and global fits (blue, [45, 119, 46, 47]), assuming NO. 85

A.1 The $\bar{\nu}_\mu$ selection efficiency at NOνA FD 92
A.2 The ν_e selection efficiency at NOνA FD 93
A.3 The $\bar{\nu}_e$ selection efficiency at NOνA FD 93

List of Tables

4.1 Reduced χ^2 values of various fit functions 35

6.1 A table summarising the current sensitivities of the neutrino oscillation experiments [117]. . . 51
6.2 The neutrino oscillation experiments currently included in `NeutrinoBit` and the associated papers 54
6.3 Comparison of the best-fit neutrino oscillation parameters between GAMBIT and NOνA [114] 64
6.4 GAMBIT and NOνA predicted [114], and NOνA observed numbers of events at the NOνA FD at the respective best-fit points 65
6.5 Comparison of the best-fit neutrino oscillation parameters between GAMBIT and MINOS [154] 69
6.6 Comparison of the best-fit neutrino oscillation parameters between GAMBIT and KamLAND (KamLAND-only, 3-ν, free θ_{13}, [128]) 75
6.7 GAMBIT and KamLAND predicted [128], and KamLAND observed numbers of events at the respective best-fit points. Note, the background counts include the oscillated geo-neutrinos from U and Th decays. 75
6.8 The best-fit parameters of different neutrino oscillation global studies [45, 119, 46, 47], assuming normal mass ordering 79
6.9 The best-fit parameters of different neutrino oscillation global studies [45, 119, 46, 47], assuming inverted mass ordering 79

7.1 A summary table of the preliminary constraints on the neutrino oscillation parameters set by GAMBIT 90

Chapter 1

Introduction

Physics is a subject concerning the motion and interaction of matter. It has always been the most reliable approach to explain and predict the evolution of matter through space and time, from the ancient study of astronomy to the revolutionary Newtonian mechanics and Einstein's theories of relativity. Among these powerful theories, it was quantum mechanics that gave birth to the Standard Model (SM) of particle physics, to date, the most successful theory that describes all known elementary particles and three of the four forces (electromagnetic, weak, and strong forces) that govern the interactions between them. It predicts the existence of W and Z bosons, and explains the origin of the masses of the elementary particles. Until a few decades ago, all particle physics experimental results had agreed with the Standard Model to an incredibly high accuracy. Despite the great predicting power of the Standard Model, there is strong evidence hinting at the existence of Physics Beyond the Standard Model (BSM). For example, the inadequate theory of quantum gravity, the severe parameter fine-tuning caused by the hierarchy problem, and the lack of Dark Matter candidates.

Another mysterious yet fascinating BSM evidence comes from the observation of the phenomena of **neutrino oscillations**. Many experiments have demonstrated that a neutrino of a particular flavour has a probability of changing type after propagating in spacetime, which was previously disallowed by the SM. Moreover, for this to be true, at least two of the three neutrino types must be massive. Neutrino oscillation is thus far the first and only definitive example of BSM physics. The phenomena of neutrino oscillation were first observed with high statistical significance by the Super-Kamiokande (Super-K) experiment in 1998 [1] in the study of cosmic-ray-produced neutrinos ('atmospheric neutrinos'), and the theory was used in explaining the deficit of solar electron neutrinos by the Sudbury Neutrino Observatory (SNO) in 2001 [2]. For their contributions to neutrino physics, the spokespersons of the two experiments, Takaaki Kajita and Arthur B. McDonald, were awarded the 2015 Nobel Prize in Physics. Furthermore, the recent observations which suggest a non-zero CP-violation phase [3] may also explain the observation of matter-antimatter asymmetry in the Universe, which further increases the urgency and importance of neutrino research, making it one of the most actively researched areas in high-energy physics.

Neutrino physics has experienced remarkable progress over the past few decades. Since Bruno Pon-

tecorvo's groundbreaking 1957 proposal [4] to extend the Standard Model to include neutrino oscillation, a multitude of experiments have been designed to investigate this phenomenon, and the six parameters that describe neutrino oscillation have been measured with varying levels of accuracy. Despite over twenty years of experimental effort, some critical questions remain unresolved, such as the precise value of the CP-violating imaginary phase, denoted as δ_{CP}, and the hierarchy of neutrino masses. A brief review of the topics in neutrino physics is found in Chapter 2.

Apart from the new experiments such as Hyper-Kamiokande (Hyper-K) [5] and the Deep Underground Neutrino Experiment (DUNE) [6], which are two large next-generation neutrino experiments currently being built in Japan and the US, upgrades to the existing experiments are also beneficial. In particular, the upgrades to the near detector ND280 of the Tokai-to-kamioka (T2K) experiment [7], a current long-baseline accelerator neutrino oscillation experiment in Japan, is now entering an exciting phase where several subdetectors have been installed and are being validated. Among the new subdetectors is the Super Fine-Grained Detector (SuperFGD), a plastic-scintillator-based novel detector. It is a fully-active target tracker that aims to perform precise particle momentum reconstruction and identification. With the upgraded subdetectors, we expect to significantly reduce the systematic uncertainties and assist in pushing the non-zero δ_{CP} measurement beyond 5σ. In Chapter 3, the design of the T2K experiment and its ND280 upgrade programmme are covered.

Chapter 4 and Chapter 5 are dedicated to topics related to the SuperFGD, including its detector design, the various calibration tasks, and a study on the reduction of charge calibration uncertainties utilising a Tranformer-based machine learning algorithm. A Transformer neural network is a type of machine learning algorithm designed to handle sequential input. It is widely adopted in many modern natural langauge processing tasks, such as translation, text summarisation, and text generation. Its unique feature, 'attention', allows the network to retain long-range awareness and is therefore also suitable for processing particle detector event images.

The full exploitation of the collected data is crucial to the advancement of neutrino study. Among the numerous methods of investigation, global fits can be performed to study the neutrino oscillation experimental results in a unified and coherent approach. Since each neutrino experiment is specifically sensitive to a subset of neutrino oscillation parameters, by combining a wide range of different experimental data, it is possible to set constraints on the neutrino oscillation parameters with an accuracy no one individual experiment has alone. However, as the field grows in scope and complexity, the interpretation of the experimental data and systematic errors become challenging. Furthermore, the limited availability of publicly accessible experiment information also adds to the difficulty.

The success of a global study relies on several factors. The accuracy of the experiment modelling, the efficiency of the parameter space exploration, and the eventual statistical interpretation are some examples of vital importance. To achieve this, we perform a neutrino oscillation global study utilising the 'Global And Modular BSM Inference Tool' (GAMBIT) fitting package [8, 9], of which the methods and

results are shown in Chapter 6. GAMBIT is an open-source global fitting software package for studying generic particle and astronomical physics models. Its modular design allows easy implementation of likelihood functions and models. The built-in scanners also provide concrete and efficient statistical sampling techniques.

Chapter 2

Neutrino Physics

2.1 A Brief History of Neutrino Physics

The postulation of a new, electrically neutral, spin-1/2 particle [a] was proposed by Wolfgang Pauli in 1930 to explain the continuous β-decay spectrum [b]. He called it neutron, a name first coined by Ernest Rutherford in 1920 for his proposed neutral nucleon to explain the discrepancy between the mass numbers of atoms and their atomic numbers. To avoid confusion, later, the name of Pauli's new particle was changed to 'neutrino' [c] by Enrico Fermi after the definitive discovery of Rutherford's neutron by James Chadwick in 1932 [11]. The hypothetical neutrino allowed Fermi to successfully develop a theory of β-decay [12] in 1934.

2.1.1 Discovery of the Three Types of Neutrino

It was not until 1956 that the first direct detection of neutrinos (specifically $\bar{\nu}_e$) was confirmed [d] by F. Reines and C. Cowan. The Reines-Cowan experiment [14] utilised a detector that had multiple alternating water and liquid scintillator layers to detect neutrinos emitted from a nuclear reactor [e] via the inverse beta decay process, $\bar{\nu}_e + p \rightarrow n + e^+$. Not many years later, the muon neutrino was observed by the Lederman–Schwartz–Steinberger experiment in 1962 [15] where a spark chamber was used to detect the muon neutrinos produced from pion decays. However, the wait for direct tau neutrino detection took a little more time. It was announced 38 years later, in 2000, by the DONUT collaboration that a total of four tau neutrino interactions originated from the decays of strange D mesons (D_S) were detected from the proton beam dump at the Fermilab [16]. This completes the discovery of all leptons as we know today, leaving the Higgs boson as the only remaining unobserved Standard Model particle (Figure 2.1) at that time.

[a] Pauli also speculated that the mass of the new particle should be of the same order of magnitude as that of an electron.

[b] It was proposed in an open letter [10] to the attendees of the Tübingen meeting in December 1930. At the end of the letter, Pauli also explained that his absence was due to a ball held in Zürich.

[c] A 'small neutron' in Italian.

[d] A tentative result was published earlier in 1953 [13].

[e] The neutrino source was initially proposed to be an atomic bomb.

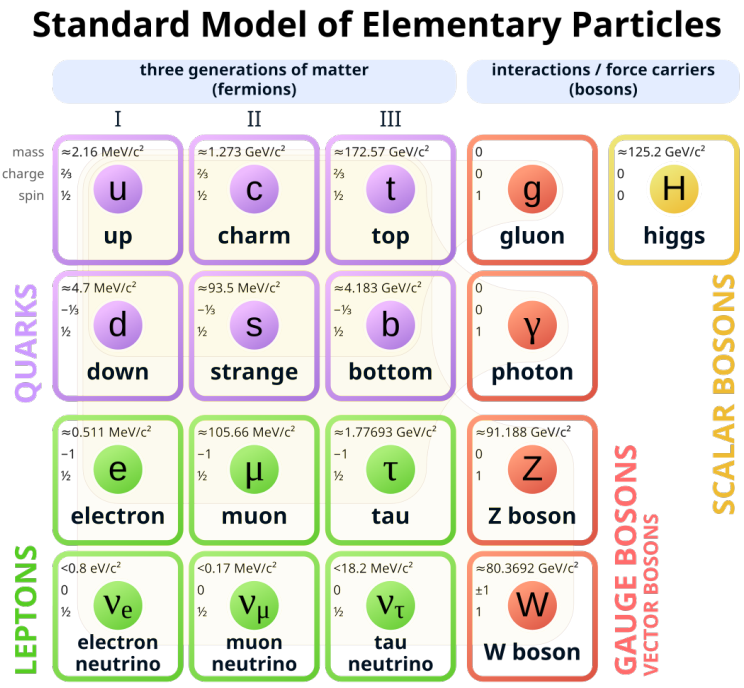


Figure 2.1: A chart [17] showing the elementary particles predicted by the Standard Model

2.1.2 Neutrino Phenomena Outside the Standard Model

Our story starts with the puzzling 'solar neutrino problem'. It refers to the observed deficit of neutrinos produced by the Sun, reported by a series of experiments tracing back to the Homestake experiment by R. Davis [18] in the late 1960s all the way to the 1990s [19, 20, 21]. At the time, it was unclear whether the problem was caused by an incomplete solar model or by some unaccounted-for flavour-converting mechanism in the leptonic sector [f].

The solar neutrino problem was definitively shown by the SNO collaboration [2] to be of a particle physics origin. The experiment result can be precisely explained by the Mikheyev-Smirnov-Wolfenstein (MSW) effect [22, 23]. The interactions with surrounding matter create an effective potential that affects the neutrino's propagation. When neutrinos travel through the Sun, they encounter regions where the matter density changes. At specific points where the density matches the condition for resonance enhancement, the oscillation effect is strengthened. This, in combination with the adiabatical change of matter density, allows the neutrino to smoothly convert from one flavour to another, maximising the effect of the resonance. The $\bar{\nu}_e$ oscillations were also confirmed in the laboratory by the KamLAND experiment in 2002 [24], which in addition also showed that ν_e and $\bar{\nu}_e$ oscillate in a consistent way without the dependency on enhancement through matter.

On the other hand, the atmospheric neutrino experiments [g] [25, 26] also hinted at a discrepancy between the observed and simulated number ratios, $(\mu/e)_{\text{data}}$ and $(\mu/e)_{\text{MC}}$, where μ and e correspond to the number of μ-like and e-like neutrino candidates. In other words, the asymmetry ratio $R \equiv \frac{(\mu/e)_{\text{data}}}{(\mu/e)_{\text{MC}}}$

[f] Note that the SM does not provide explanations for leptonic flavour-changing processes.
[g] Many of these experiments started as proton decay searches.

was reported by some experiments to be less than one. Despite the early tension between the water Cherekov experiments and the calorimetry experiments [27], the anomaly was convincingly shown to exist by the Super-K experiment in 1998 [1] at a significance level of 6.2σ. In the paper, all the different ν_μ samples displayed a strong zenith angle dependency—the deficit only occurred in the upward-travelling angles. This is strong evidence suggesting flavour-changing processes [h], and very excitingly, the result was consistent with the two-flavour $\nu_\mu \to \nu_\tau$ oscillations.

With the ability to explain both the solar neutrino problem and the atmospheric neutrino anomaly, the three-flavour neutrino oscillation framework became a viable and convincing extension to the SM. The remaining oscillation between $e \leftrightarrow \tau$ was hinted to be small but none-zero by early reactor neutrino experiments [28, 29, 30] and also supported by an early global fit study [31] in 2006. In 2011, T2K [32] and MINOS [33] both reported some electron neutrino excess. Further global studies [34, 35] using the results, although inconclusive, found $\theta_{13} > 0$ at 3σ. It was the short-baseline reactor neutrino experiments that were able to precisely measure θ_{13} [36, 37, 38], with the Daya-Bay experiment publishing the first 5σ result in 2012 [37]. By then, all three-flavour mixing processes had been discovered.

2.2 Neutrino Oscillations

In this section, the standard three-flavour neutrino oscillation framework is briefly summarised.

Neutrino oscillation is a quantum-mechanical phenomenon [i] where a neutrino of a given 'flavour' (electron, muon, or tau), after propagation in spacetime, can be measured to be of a different flavour. It is caused by the fact that the neutrino flavour eigenstates $|\nu_\alpha\rangle, \alpha = e, \mu, \tau$ in weak interactions do not correspond to neutrino mass eigenstates $|\nu_i\rangle, i = 1, 2, 3$ exactly one-to-one, but rather are each a superposition of the three.

2.2.1 The PMNS Matrix

The mixing between the flavour and mass eigenstates is a simple change of basis and can be described by a unitary leptonic mixing matrix $U_{\alpha i}$ as

$$|\nu_\alpha\rangle = U_{\alpha i} |\nu_i\rangle . \tag{2.1}$$

A generic 3×3 unitary matrix can be parameterised by nine real parameters (three mixing angles and six phases). However, one can redefine each state by $|\ell_\alpha, x\rangle \to e^{i\phi_\alpha} |\ell_a, x\rangle$ (lepton states) or $|\nu_i, x\rangle \to e^{i\phi_i} |\nu_i, x\rangle$ (neutrino states) without altering the probability $|\langle\nu_\beta|\nu_\alpha, x\rangle|^2$, removing five (not six due to the neutrino mass term) phases assuming Dirac neutrinos [j]. In the case of Majorana neutrinos, one cannot rotate a neutrino state by an arbitrary phase because it will make the mass a complex number. In summary, there are three mixing angles plus a CP-violating phase δ_{CP} assuming Dirac neutrinos, but

[h] This cannot be explained by the absorption of ν_μ in the Earth because the interaction rate is too small

[i] In this chapter, only a simplified derivation of the neutrino oscillation probability is shown. For proper treatments such as the wave-packet formalism, please see [39].

[j] From here on, this assumption holds implicitly throughout the thesis unless otherwise specified.

there are six (three angles plus three phases) assuming Majorana neutrinos [k]. Therefore, the leptonic mixing matrix can be conveniently parameterised as

$$U_{\alpha i} = \begin{bmatrix} 1 & 0 & 0 \\ 0 & c_{23} & s_{23} \\ 0 & -s_{23} & c_{23} \end{bmatrix} \begin{bmatrix} c_{13} & 0 & s_{13}e^{-i\delta_{\rm CP}} \\ 0 & 1 & 0 \\ -s_{13}e^{-i\delta_{\rm CP}} & 0 & c_{13} \end{bmatrix} \begin{bmatrix} c_{12} & s_{12} & 0 \\ -s_{12} & c_{12} & 0 \\ 0 & 0 & 1 \end{bmatrix}, \tag{2.2}$$

where $c_{ij} \equiv \cos\theta_{ij}$ and $s_{ij} \equiv \sin\theta_{ij}$. For Majorana neutrinos, the mixing matrix is formed by multiplying Equation (2.2) by an additional matrix containing the two Majorana phases, $\mathrm{diag}(e^{i\eta_1}, e^{i\eta_2}, 1)$. Without loss of generality, the domains can be defined to be $0 \leq \theta_{ij} \leq \pi/2$ and $0 \leq \delta_{\rm CP} < 2\pi$. This is the Pontecorvo-Maki-Nakagawa-Sakata (PMNS) parameterisation of the leptonic mixing matrix [4, 40]. It is a unitary 3×3 matrix parameterised by three mixing angles θ_{12}, θ_{13}, and θ_{23} and the CP-violating phase $\delta_{\rm CP}$.

2.2.2 Three-Neutrino Oscillations in Vacuum

At $x = 0$, we start with a pure flavour eigenstate $|\nu(x=0)\rangle = |\nu_\alpha\rangle$. It is a superposition of the three mass states,

$$|\nu_\alpha\rangle = \sum_{i=1}^{3} U^*_{\alpha i} |\nu_i\rangle . \tag{2.3}$$

For relativistic neutrinos, after propagating a distance $L \approx t$ (using the conventional $\hbar = c = 1$), the mixture of the three mass states changes as

$$|\nu_\alpha(t)\rangle = \sum_{i=1}^{3} U^*_{\alpha i} |\nu_i(t)\rangle , \tag{2.4}$$

and the probability for observing the state to be $|\nu_\beta\rangle$ is therefore

$$P(\nu_\alpha \to \nu_\beta) = \Big| \langle \nu_\beta | \nu_\alpha(t) \rangle \Big|^2 = \left| \sum_{j=1}^{3} \sum_{i=1}^{3} U_{\beta j} U^*_{\alpha i} \langle \nu_j | \nu_i(t) \rangle \right|^2 . \tag{2.5}$$

Since the mass states are eigenstates of the Hamiltonian in vacuum, they propagate as plane waves, ie

$$|\nu_i(t)\rangle = e^{-iE_i t} |\nu_i\rangle , \tag{2.6}$$

where the energy of the neutrino mass eigenstate $|\nu_i\rangle$ of mass m_i and momentum p_i is $E_i = \sqrt{p_i^2 + m_i^2} \approx p + m_i^2/2E$. In the approximated energy expression, we assumed that all momenta are sufficiently large so that all $p_i \approx p \approx E$ where p is some momentum in the relativistic regime. Therefore, Equation (2.5) becomes

$$P(\nu_\alpha \to \nu_\beta) = \left| \sum_{j=1}^{3} \sum_{i=1}^{3} U_{\beta j} U^*_{\alpha i} e^{-iE_i t} \langle \nu_j | \nu_i \rangle \right|^2 = \left| \sum_{i=1}^{3} U_{\beta i} U^*_{\alpha i} e^{-iE_i t} \right|^2 . \tag{2.7}$$

[k] Note, as we will show later, the measurement of the neutrino oscillation probability is insensitive to the choice of the Majorana phases.

Note that in the last step, we used the identity $\langle \nu_j | \nu_i \rangle = \delta_{ij}$ and summed over the j index. Finally, expanding Equation (2.7) yields the expression

$$\begin{aligned} P\left(\nu_\alpha \to \nu_\beta\right) = \delta_{\alpha\beta} - 4\sum_{i<j}^{3} \mathrm{Re}\big\{U_{\alpha i} U_{\beta i}^* U_{\alpha j}^* U_{\beta j}\big\} \sin^2\left(\Delta m_{ji}^2 \frac{L}{4E}\right) \\ + 2\sum_{i<j}^{3} \mathrm{Im}\big\{U_{\alpha i} U_{\beta i}^* U_{\alpha j}^* U_{\beta j}\big\} \sin\left(\Delta m_{ji}^2 \frac{L}{2E}\right), \end{aligned} \tag{2.8}$$

where $\Delta m_{ji}^2 \equiv m_j^2 - m_i^2$ are the 'mass splittings'. In the case of antineutrino oscillations, transition probability $P(\overline{\nu}_\beta \to \overline{\nu}_\alpha)$ takes a similar form to Equation (2.8), but with the U replaced by U^* and with the sign of the last term inverted. There are a few observations worth noting,

1. A total of six parameters are required to describe the phenomena of neutrino oscillations (three mixing angles, two mass splittings, and one phase).

2. The probability is insensitive to the choice of Dirac or Majorana neutrinos due to the combinations of U elements cancelling out the phases.

3. There must exist at least two massive neutrinos and non-vanishing mixing for the flavour oscillations to happen.

Physically speaking, due to the mass differences between neutrino mass states, they each oscillate at a different phase. This causes the linear combination of mass eigenstates to alter and hence changes the probability of observing a certain neutrino flavour. Macroscopically, this results in changes in the neutrino population of a given species measured at source and at a distance.

2.3 Open Questions

With the advancement of the experimental techniques and theoretical calculations, the field of neutrino physics were able to solve many mysteries, such as the detection of these highly elusive subatomic particles, the successful identification of the root cause of the solar neutrino problem, and the precise measurements of the neutrino oscillation parameters.

However, many fundamental questions about neutrinos remain open despite the relentless efforts from many angles for more than 90 years since the proposal of neutrino [41]. Here, I provide a short discussion on a non-exhaustive list of the current open questions in neutrino physics.

Neutrino absolute mass scale. There are some approaches to gaining insight into the absolute mass scale of neutrinos, but thus far, no conclusive measurements have been made. Neutrino oscillation experiments can set lower bounds on neutrino masses by measuring the mass splittings $|m_i| \geq \sqrt{\Delta m_{ij}^2}$ for $\Delta m_{ij}^2 > 0$, but they give no information about the upper bounds. A direct neutrino mass measurement is to exploit energy-momentum-conservation by observing the electron spectrum in a β-decay process where (anti)neutrino is involved. Since this method is purely concerned with kinematics, it is therefore

model-independent. For example, the KATRIN experiment [42] studied the β-spectrum from tritium decay and obtained

$$m_{\nu_e}^{\text{eff}} < 0.8 \text{ eV}, \tag{2.9}$$

at 90% CL. Another indirect neutrino mass measurement comes from astrophysical measurements, in particular regarding the freeze-out of stable neutrinos [1] in the early Universe, which contribute to the total energy density. This, however, only gives constraints to the sum of neutrino masses $m_{\text{tot}} \equiv \sum_\nu m_\nu$.

Neutrino mass ordering. Although it was experimentally determined that $\Delta m_{21}^2 > 0 \Rightarrow m_1 < m_2$ thanks to the Mikheyev-Smirnov-Wolfenstein (MSW) effect [43, 44], whether the mass ordering is 'normal' ($m_1 < m_2 < m_3$) or 'inverted' ($m_3 < m_1 < m_2$) is still unknown. Current global fit results [45, 46, 47] moderately support the normal ordering, but none exceeds 3σ. A Bayesian study claims decisive evidence for the normal ordering by combining cosmological observations and oscillation experiment results [48], but the result is contested [49]. Future experiments such as JUNO [50] and further combined studies may be able to solve the problem [51].

CP-violation and matter-antimatter asymmetry. CP-symmetry is the symmetry between matter and antimatter. Although a recent study by the T2K collaboration [3] has ruled out $\delta_{\text{CP}} = 0$ at 3σ for both mass orderings, further experiments with higher sensitivities and larger statistics are required to confirm the result at a higher significance. δ_{CP} is the least constrained parameter of all oscillation parameters since the neutrino oscillation probability is a highly degenerate multi-variable function, which means that the determination of the CP-phase requires the remaining parameters to be understood well. On top of it, since the CP-phase is only associated with the imaginary part in Equation (2.8), disappearance measurements, which measure cases where $\alpha = \beta$, will cancel out the imaginary part and hence are insensitive to δ_{CP}. Therefore, the contributions from future generation experiments such as Hyper-Kamiokande [5] and DUNE [6], which will produce much larger statistics for the appearance channels, will be crucial to the precise measurement of the CP-phase.

Since the PMNS matrix is the only remaining possible source of CP-violation in the current SM framework (assuming neutrinos are Dirac), the experimental outcome will be significant and paradigm-defining. If substantial leptonic CP-violation is confirmed experimentally, it could provide strong evidence for leptogenesis as the origin of the matter-antimatter asymmetry. Alternatively, if CP-violation in the lepton sector is determined to be insufficiently small, then it is a strong hint at the existence of some BSM physics that generates the imbalance.

Are neutrinos Majorana? There are many experiments that are searching for the evidence of Majorana neutrinos by looking for the hypothetical process of neutrinoless double β-decay [52, 53, 54]. These experiments can provide stringent constraints on many BSM models that require Majorana neutrinos. Furthermore, a positive result automatically implies the violation of lepton number conservation, which is in and of itself a BSM phenomenon.

[1] Or neutrinos with mean lifetimes comparible to some cosmological timescale.

Chapter 3

The T2K Neutrino Oscillation Experiment

3.1 The T2K Experiment

The Tokai-to-Kamioka (T2K) experiment [55] in Japan is a long-baseline neutrino experiment designed to study the phenomena of neutrino oscillation. It utilises a near-far detector configuration to measure neutrino energy spectra at two different locations (see Figure 3.1). From the discrepancy, one can measure the oscillation behaviour and extract oscillation parameters.

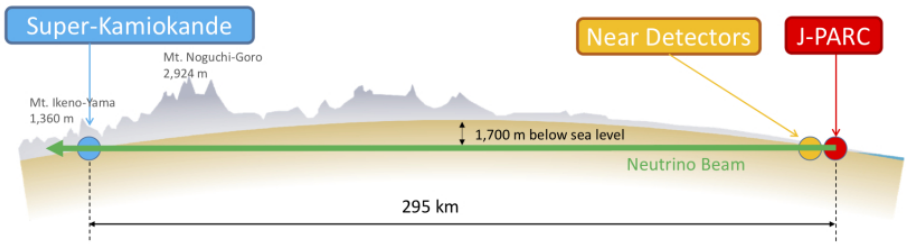


Figure 3.1: The T2K experiment beamline. A beam of ν_μ produced by a proton accelerator at the Japan Proton Accelerator Research Complex (J-PARC) is directed at the Super-K detector 295 kilometres down the beamline. The near detector suite ND280 is located 280 metres away from the neutrino source, providing valuable measurements about the neutrino beam.

The initial physics goals, as listed in the original T2K proposal [55], include the discovery of ν_e appearance in a ν_μ beam [a] and the precision measurements of Δm^2_{32} and θ_{23} by studying ν_μ disappearance. Within around two decades, from the first physics data taken by both the ND280 and the Super-Kamiokande (Super-K) in 2010, both goals have been achieved [56, 57]. Now, the experiment is focusing on the measurement of the CP-violating angle δ_{CP}, which attempts to answer one of the most fundamental questions in physics—is there an asymmetry between neutrino and antineutrino oscillations? And if so, can the CP-violation in the leptonic mixing explain the matter-antimatter imbalance in the Universe? The outcome of this study will be of significant importance regardless of the answer. If the answer is positive, the result will sufficiently explain the mystery [b]. However, if the answer is negative since it was experimentally shown that the CP-violating processes in the quark sector are insufficient to

[a] By confirming the mixing angle $\theta_{13} \neq 0$.
[b] Albeit somewhat boringly fail to defeat the thus far impeccable Standard Model once again.

explain matter-antimatter imbalance, it would require something outside the SM—convincing evidence of BSM physics.

3.2 The T2K Neutrino Beam

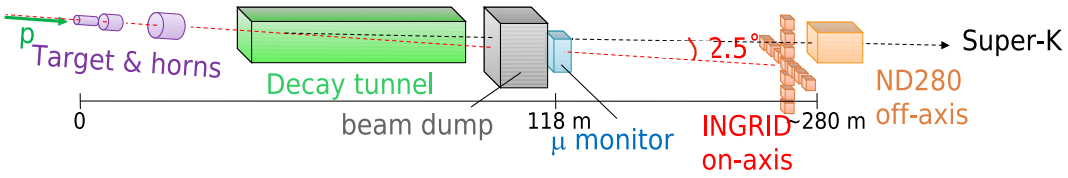


Figure 3.2: An illustration of the T2K neutrino beamline [58]

An illustration of the the T2K neutrino beamline is shown in Figure 3.2. A beam of protons are accelerated to 30 GeV at the Japan Proton Accelerator Research Complex (J-PARC) in Tokai on the east coast of Japan. In the proton beam is a graphite rod with a diameter of 2.6 cm and a length of 91.4 cm, corresponding to about two interaction lengths, serving as the target. The protons collide with the carbon nuclei, producing an abundance of mesons composed primarily of pions and kaons. These mesons are then focused and charge-selected by the three magnetic horns installed in the beamline and subsequently are allowed to decay in a decay tunnel, producing an intense neutrino beam. The produced neutrinos are predominantly μ-flavoured with a purity of 99% thanks to the helicity suppression in meson decays. While the neutrinos continue travelling towards the near and far detectors, the hadronic and charged-leptonic by-products are stopped by the beam dump.

Figure 3.3 shows the latest publicly available nominal unoscillated neutrino flux predictions. The data release [c] corresponds to the T2K 2020 neutrino oscillation physics result [59].

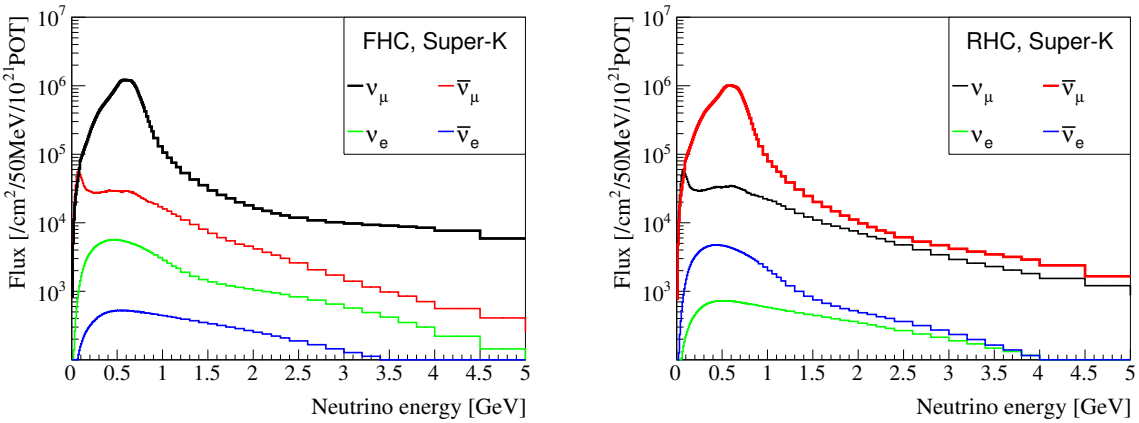


Figure 3.3: The T2K neutrino flux predictions at the Super-K detector for the Forward Horn Current (FHC, left) and Reverse Horn Current (RHC, right) modes [60, 61].

An off-axis beam design is adopted [62]: ND280 and the far detector Super-K are located along an axis that is 2.5° away from the central axis of the neutrino beam. This configuration brings several benefits. As shown in Figure 3.4, the T2K flux maximum is tuned to peak at 600 MeV to achieve an

[c] Data available to download at `https://t2k-experiment.org/result_category/flux/`.

oscillation maximum at Super-K 295 km downstream; the high energy tail of the neutrino spectrum is also suppressed, lowering the occurrence of complicated neutrino-nuclear interactions, hence increasing the reconstruction accuracy.

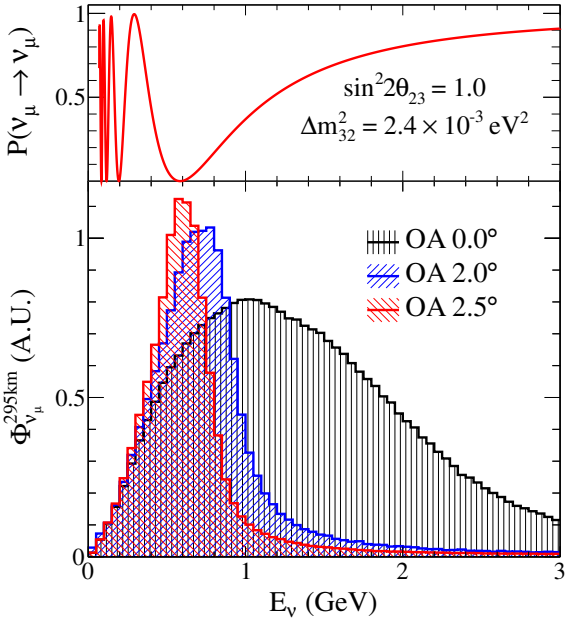


Figure 3.4: T2K detectors are located 2.5° off-axis, achieving a neutrino spectrum that peaks at 600 MeV, coninciding with an oscillation minimum. [62]

3.3 The ND280 Near Detector after the 2020 Upgrade

The near detector ND280 is a hybrid detector composed of several subdetectors of different types. The detector configuration before the Upgrade [7] is shown in Figure 3.5 (left).

ND280 is placed downstream 280 metres from the carbon target, as shown in Figure 3.2. It is used to understand the neutrino fluxes, electron neutrino pollution, and energy spectra of the incoming neutrino beam. Using the data from the near detector, one can estimate the expected interaction rates at the far detector Super-K in the absence of oscillation. In addition to the monitoring duties, ND280 supports various neutrino-nuclear interaction measurements [63, 64, 65] and BSM physics searches [66].

3.3.1 Components of ND280

Several significant modifications have been brought to the ND280 suite since 2020, thanks to the ND280 Upgrade programme [7]. The Upgrade programme replaced the upstream π^0-detector (P0D) [67] with a new detector group consisting of six Time-of-Flight planes and a highly-granular scintillator detector SuperFGD sandwiched by two High-Angle TPCs, as illustrated in Figure 3.5 (right). The Upgrade aims to improve the sensitivity to both new and established neutrino interactions. The ability to measure the properties of incoming neutrinos that are important to the oscillation analysis, such as beam flux, energy spectrum, and electron-neutrino contamination, will also be enhanced. With the Upgrade, ND280

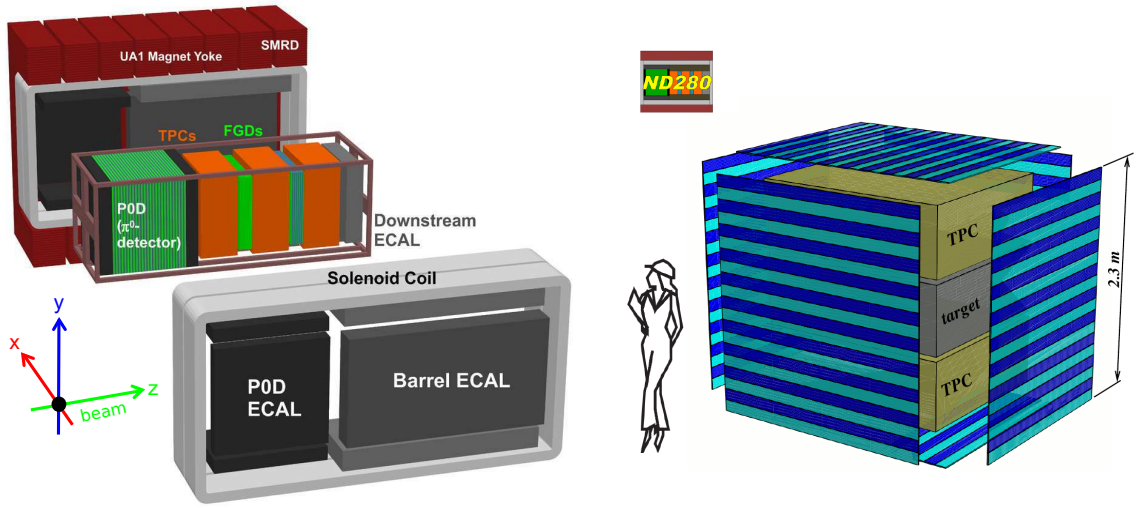


Figure 3.5: An exploded view of the ND280 detector suite prior to the 2020 Upgrade (left), showing the constituent subdetectors. The ν_μ beam enters from the left of the figure along the z-axis. The detector coordinate system is right-handed, as shown by the origin at the geographical centre, which lies near the downstream end of the first TPC. The P0D was replaced by a group of new detectors (right) as part of the Upgrade [7], and the installation was completed in 2024.

will be able to study the neutrino-matter interactions with high accuracy, which will help improve the complicated nuclear interaction models and future efforts for the next-generation neutrino detectors.

Magnet and Side Muon Range Detector

The ND280 detector is surrounded by a 900-tonne magnet repurposed from the CERN UA1 experiment, which provides a 0.2 T magnetic field parallel to the x-axis. The magnet is crucial for identifying particle charges and measuring particle kinematics.

The Side Muon Range Detector (SMRD) [68] consists of plastic scintillators inserted into the gaps in the magnet yoke. It is used to measure the muons that escape the inner detectors. It can also be used as an active veto for events coming into the detector from outside, for example, as a trigger for cosmic rays.

Fine-Grained Detectors

In the downstream part of the ND280 detector, there are two Fine-Grained Detectors (FGDs) [69], which serve as targets for neutrinos to interact with and high-resolution trackers. Both the upstream and downstream FGDs consist of plastic scintillator bars arranged in criss-crossing planes perpendicular to the z-axis. The scintillating light signals produced from neutrino interactions are read out by the Wavelength-Shifting (WLS) fibres to reconstruct particle tracks. Figure 3.6 shows reconstructed particle tracks passing through TPCs and FGDs.

Additionally, the downstream FGD also contains water layers between the scintillator planes for the purpose of understanding neutrino interactions with water.

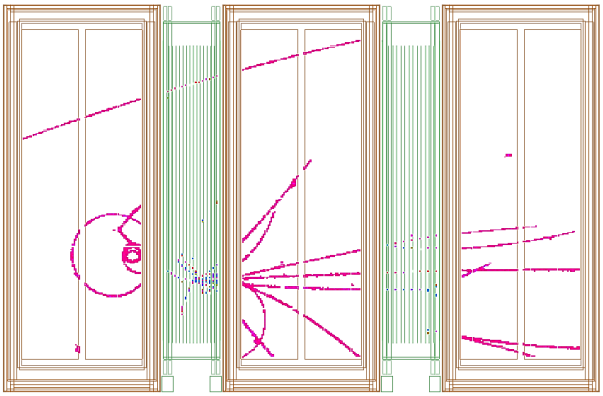


Figure 3.6: An example event display showing particle tracks in the three TPCs and the two FGDs [70]

Time Projection Chambers

Also in the downstream part are the three argon-based gaseous Time Project Chambers [70], which are separated by the two FGDs. A schematic diagram of a TPC can be found in Figure 3.7.

As the charged particles produced from neutrino interactions traverse through the TPCs and ionise the gas molecules, tracks of ionisation electrons are formed. These electrons drift towards the outer sides of the TPCs due to the electric fields produced by a cathode (on the centre y-z plane of TPC) and two fine mesh anodes (one on each side, y-z plane). A stronger field is applied in the region between the anode and the Micro-Mesh Gaseous Structure (MicroMegas, 12 per side) modules. As the electrons cross through the anode mesh, they are accelerated even more and gain the ability to ionise the gas molecules, causing an avalanche effect. The arrival time and position are recorded by the readout planes, which respectively provide the information on the x and y-z positions of the track. Based on the information, the particle tracks and kinematics can be determined. Figure 3.6 shows reconstructed particle tracks passing through TPCs and FGDs.

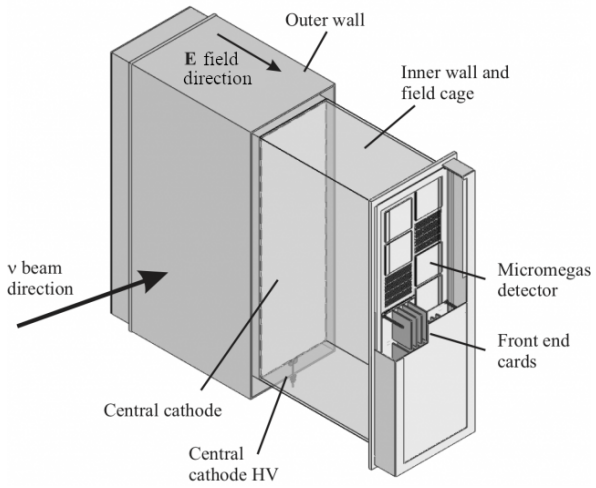


Figure 3.7: A schematic diagram of a TPC [71]. The detector volume is separated by the central cathode into two mirrored regions. With the two anodes installed at each side of the detector, two mirrored electric fields are generated, pointing from the side anodes at the central cathode. The direction of one electric field is illustrated in the diagram.

Electromagnetic Calorimeters

The electromagnetic calorimeters (ECals) [72] are divided into several parts, each surrounding different ND280 subdetectors. The P0D-ECal encloses the original space occupied by the replaced P0D; the Barrel-Ecal forms a tube and surrounds the downstream detectors; and the Downstream-Ecal closes off the downstream end of the ND280 like an end-cap.

The ECals are designed to detect and measure the escaping electromagnetic showers. They are made up of layers of scintillator bars interleaved with lead sheets to increase the probability of electromagnetic showers.

Super Fine-Grained Detector

The Super Fine-Grained Detector (SuperFGD) [7] is a novel, highly-granular plastic scintillator detector designed for the ND280 Upgrade. The detector is made up of approximately two million 1 cm^3 cubes woven together by the WLS fibres. These fibres collect and direct the scintillation signals produced by neutrino interactions in three orthogonal directions, measured by the Multi-Pixel Photon Counters (MPPCs) at the fibre ends.

SuperFGD not only provides an additional 2-tonne active mass, due to the high spatial resolution of the detector design, it also improves the detector acceptance and lowers the detection energy threshold, enabling the reconstruction of short particle tracks that could not be resolved before.

More information on SuperFGD can be found in Chapter 4.

High-Angle Time Projection Chambers

Two High-Angle Time Projection Chambers (HATs) [7] are installed as part of the ND280 Upgrade, stacking on top and below the SuperFGD. Their primary purpose is to precisely track charged particles at high angles relative to the neutrino beam direction. Because of the positioning, the HATs are expected to significantly improve the ND280 acceptance and increase the selection efficiency, especially at higher angles (see Figure 3.8).

The HATs utilise similar technologies to those used on the existing TPCs. However, one design difference lies in the use of Encapsulated Resistive Anode MicroMegas (ERAM) [73]. This new MicroMegas has an additional resistive layer that serves as spark protection and helps distribute the incoming charge across neighbouring channels, improving the spatial resolution.

Time-of-Flight Detectors

There are six Time-of-Flight detector planes (ToFs) [74] surrounding the HATs and SuperFGD, and each ToF plane is composed of 20 scintillating plastic bars. The scintillating light signals emitted are read out by silicon photomultipliers (SiPMs) attached to both ends of each bar.

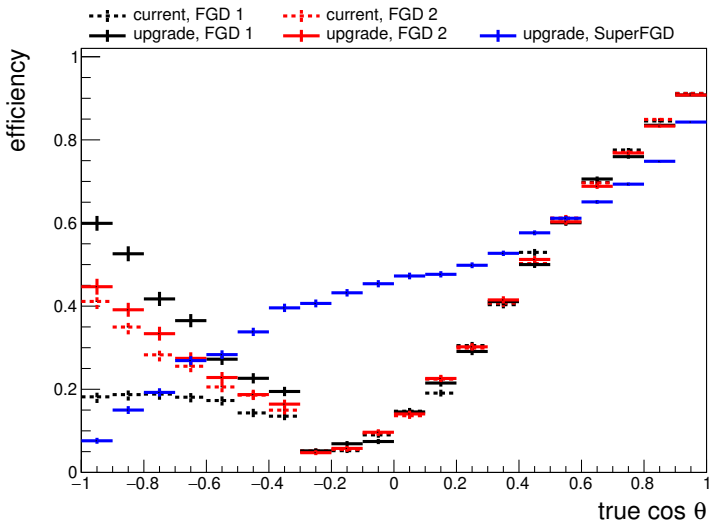


Figure 3.8: The expected selection efficiency for μ_ν charged-current (CC) events originating from different detectors as a function of the angle between the product muon and the beam axis [7]. The ν_μ CC event selection efficiency in SuperFGD is significantly improved, particularly at higher angles.

The excellent timing resolution of 0.14 ns enables the ToF detectors to tag the entering and outgoing charged particles by measuring the time of flight for each particle track [75]. This feature can be utilised to help veto background events originating from outside the detector, such as cosmic rays and sand muons.

3.4 The Super-Kamiokande Detector as the T2K Far Detector

The Super-Kamiokande (Super-K) detector[d] was initially proposed to study the subjects related to proton decay, but the lucky detection of a neutrino burst (a total of 11 neutrinos) from the supernova SN1987A by the Kamioka II detector[e] right after its modification completed near the end of 1986 [77] heavily shifted Super-K's primary focus to neutrino astronomy and solar neutrinos. The construction of the Super-K detector started in 1991 and was completed in 1996.

The Super-K detector is a large water Cherenkov detector built to study neutrinos of various sources, including those produced by the solar nuclear processes, cosmic-ray interactions with the atmosphere, and the hypothetical proton decays. It is also used as the far detector of the T2K experiment to observe neutrinos generated from the particle accelerator at J-PARC.

The Super-K detector is located 295 km away from J-PARC and about 1000 m underground in the old Kamioka mine in Hida City of Gifu, Japan (see Figure 3.9 left). It consists of a 40 m tall and 40 m wide cylindrical tank holding rough 50 kt of water. In 2020, the Super-K water became doped with gadolinium (gadolinium sulfate octahydrate, $Gd_2(SO_4)_3 \cdot H_2O$) at a concentration of 0.03% [f] for

[d] Interestingly, the collaboration was initially proposed under the name 'JACK' (Japan America Collaboration at Kamioka) [76].

[e] The observation was somewhat 'reversed', where the search of the neutrino burst came after the optical sighting of the supernova event on 24 February 1987 [77].

[f] The first and second Gd loadings happened in 2020 and 2022, respectively.

an increased neutron capture efficiency [78, 79]. The tank is divided into an inner detector (ID) and an outer detector (OD). The OD has 1,885 8-inch PMTs to identify incoming cosmic rays, while the ID wall is mounted with 11,146 20-inch photomultiplier tubes (PMTs, see Figure 3.9 right) which are designed to detect the Cherenkov light produced by neutrino interactions with the water.

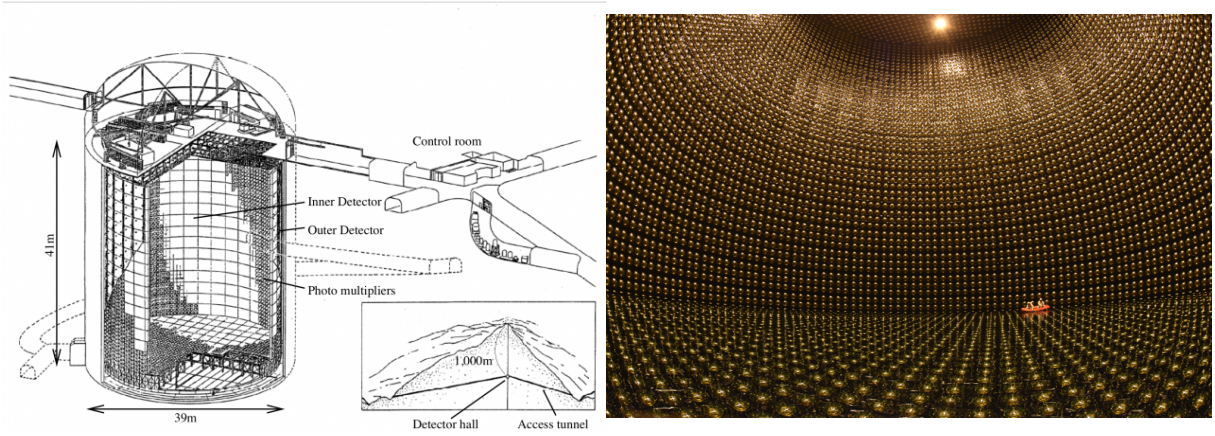


Figure 3.9: A schematic diagram of the Super-Kamiokande detector and its location underground in the Kamioka mine (left, [80]). A photo showing the PMTs mounted on the inner wall of the Super-K detector during maintenance (right, [81]).

The Super-K detector distinguishes the flavour of a neutrino charged-current (CC) interaction by identifying what leptonic particle is produced. If the resulting lepton of the interaction travels at a speed $\beta \equiv v/c > 1/n$ [g], where n is the refractive index of water, a cone of Cherenkov light will be generated and subsequently observed by the PMTs. Due to the lower mass, the electrons are more susceptible to scattering and produce electromagnetic showers, resulting in rings that are 'fuzzier and noisy' visually compared to those emitted by muons. Combining with the charge and timing information, Super-K exploits a likelihood-based particle identification (PID) algorithm [82] to tell apart muons and electrons, as illustrated in Figure 3.10.

The most common neutrino interaction for the T2K experiment is the charged-current quasi-elastic (CCQE), where a neutrino weakly interacts with a bound nucleon and outgoes a lepton and a different nucleon, $\nu_\ell + N \to \ell + N'$. An example of such interactions is $\nu_\mu + n \to \mu^- + p^+$. In this case, T2K reconstruct the neutrino energy solely based on the outgoing lepton kinematics, assuming stationary nuclear target with a known binding energy E_b, using the formula,

$$E_\nu = \frac{m_{N'}^2 - (m_N - E_b)^2 - m_\ell^2 + 2E_\ell(m_N - E_b)}{2\left((m_N - E_b) - E_\ell + p_\ell \cos\theta_\ell\right)}, \tag{3.1}$$

where the m's are the masses, p_ℓ is the charged lepton momentum, θ_ℓ is the angle between the beam axis and $\vec{p_\ell}$. Due to final state interactions (FSIs), re-absorption, and other nuclear effects, the CCQE events cannot be directly selected. Instead, they are selected on the topological level by selecting events with no final state mesons (CC0π). The formula also does not consider the Fermi motion of the nucleon, leading to further deviation.

[g] The kinetic energy thresholds for an electron and a muon are 0.264 MeV and 54.6 MeV, respectively.

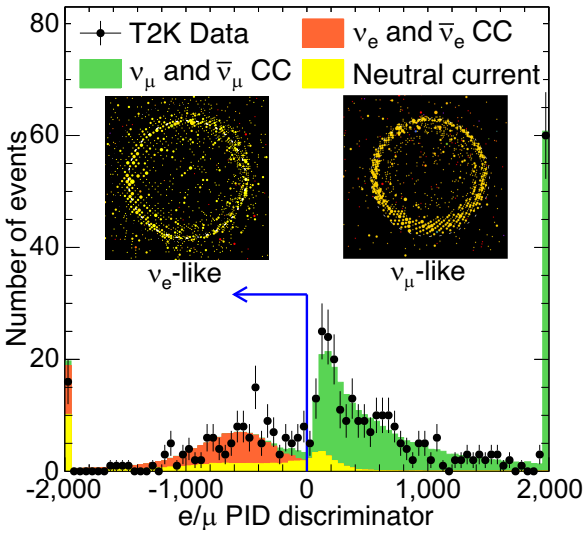


Figure 3.10: Super-K utilises a likelihood-based particle identification algorithm to distinguish between a μ-like candidate and a e-like candidate [3]. Visually, a μ-ring is sharper because muons are less prone to scattering in water.

3.5 T2K Oscillation Ananlysis

For the T2K beam energy and baseline, if the matter effects are ignored, the probability of a muon (anti)neutrino to oscillation to an electron (anti)neutrino is approximately given by

$$P(\nu_\mu \to \nu_e) \approx \sin^2(2\theta_{13})\sin^2(\theta_{23})\sin^2\left(\frac{\Delta m^2_{32}L}{4E}\right) \mp \frac{1.27\Delta m^2_{21}L}{E} 8 J_{\text{CP}} \sin^2\left(\frac{\Delta m^2_{32}L}{4E}\right), \tag{3.2}$$

where the second term is negative for neutrinos and positive for antineutrinos, E is the neutrino energy, $\Delta m^2_{ij} \equiv m^2_i - m^2_j$ are the mass squared differences, L is the baseline, and J_{CP} is the Jarlskog invariant [83] that measures the strength of CP-violation. It is defined as

$$J_{\text{CP}} \equiv \frac{1}{8}\cos(\theta_{13})\sin(2\theta_{12})\sin(2\theta_{23})\sin(2\theta_{13})\sin(\delta_{\text{CP}}). \tag{3.3}$$

On the other hand, an approximation for the muon (anti)neutrino survival probability for the T2K experiment can be written as

$$P(\nu_\mu \to \nu_\mu) \approx 1 - \left[\cos^4(\theta_{13})\sin^2(2\theta_{23}) + \sin^2(2\theta_{13})\sin^2(\theta_{23})\right]\sin^2\left(\frac{\Delta m^2_{32}L}{4E}\right), \tag{3.4}$$

where the symbols have the same meanings as those in Equation (3.2). Note, Equation (3.4) can be rearranged into

$$P(\nu_\mu \to \nu_\mu) \approx 1 - 4\cos^2(\theta_{13})\sin^2(\theta_{23})\left[1 - \cos^2(\theta_{13})\sin^2(\theta_{23})\right]\sin^2\left(\frac{\Delta m^2_{32}L}{4E}\right), \tag{3.5}$$

which is symmetrical under the change of sign $\left(\cos^2(\theta_{13})\sin^2(\theta_{23}) - \frac{1}{2}\right) \to -\left(\cos^2(\theta_{13})\sin^2(\theta_{23}) - \frac{1}{2}\right)$. This means that the constraints on $\sin^2(\theta_{23})$ will be symmetric with respect to the value $\frac{1}{2\cos^2(\theta_{13})} \approx \frac{1}{2}$[h].

[h]This degeneracy also occurs in other neutrino oscillation long-baseline accelerator experiments such as NOνA and MINOS.

If $\theta_{23} > \pi/4$, it is said that the mixing angle is in the 'upper octant' (UO), and if $\theta_{23} < \pi/4$, it is said to be in the 'lower octant' (LO). However, the measurements of the ν_e and $\bar{\nu}_e$ appearance channel can break the degeneracy.

In the oscillation analysis, while marginalising all systematic uncertainty parameters, the oscillation parameters are fitted to data by minimusing the log-likelihood

$$-\ln(\mathcal{L}) = \sum_i \left[N_i^{\text{exp}} - N_i^{\text{obs}} + N_i^{\text{obs}} \ln\left(\frac{N_i^{\text{obs}}}{N_i^{\text{exp}}}\right)\right], \tag{3.6}$$

where the summation runs over each 2D bin of reconstructed neutrino energy and muon scattering angle, N_i^{exp} and N_i^{obs} are the numbers of predicted and observed events in bin i.

Chapter 4

The Super Fine-Grained Detector

The Super Fine-Grained Detector (SuperFGD) is a novel plastic scintillating detector, newly incorporated into the existing ND280 detector suite along with the two High-Angle TPCs (HATs) and the six Time-of-Flight planes (TOFs) as a part of the T2K ND280 Upgrade [7]. The majority of the detector consists of $192 \times 56 \times 184 = 1{,}956{,}864$ plastic scintillator cubes with a size of $1 \times 1 \times 1$ cm^3. A schematic mock-up of some SuperFGD cubes can be found in Figure 4.1.

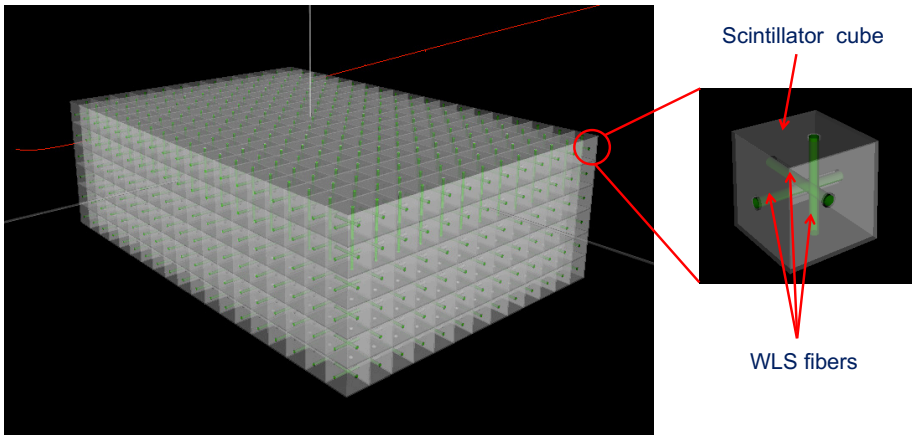


Figure 4.1: A 3D concept model of a $19 \times 6 \times 13$ cube segment of the SuperFGD [7]. A zoom-in view of a cube, including the WLS fibres, can be seen on the right.

The SuperFGD is capable of measuring particle tracks with a spatial resolution of $\sim \mathcal{O}(1$ cm), thanks to its fine granularity. The on-detector LED calibration system also ensures the detector is well-calibrated at all times, preventing the particle energy measurements from time and temperature drifts. Furthermore, the detector also provides an additional two-tonne active target. With the help of the two HATs, the geometrical acceptance and efficiency of the ND280 detector are significantly improved.

In this chapter, the basic SuperFGD design and specifications are presented. In addition, the SuperFGD calibration items are described, and in particular, the charge calibration methods, which include the gain and pedestal algorithms, are described in detail.

4.1 SuperFGD Components

4.1.1 Plastic Scintillator Cubes

The scintillator cubes used in the SuperFGD are manufactured by UNIPLAST Co. in Vladimir, Russia, using injection moulding. The cubes are made of transparent polystyrene doped with 1.5% para-terphenyl (PTP) and 0.01% POPOP [a], and coated with a chemical agent, resulting in a reflective white micropore deposit shell designed to reduce light leakage from one cube to the neighbouring ones. After the processes, the average cube width is measured to be 10.26 mm, with a standard deviation of less than 30 μm [84].

Three orthogonal holes of 1.5 mm diameter are drilled through each cube, and the position precision of the holes is controlled to be less than ~ 40 μm. With the manufacture precision, the holes are able to accept the 1 mm WLS fibres to be threaded through, as shown in Figure 4.2.

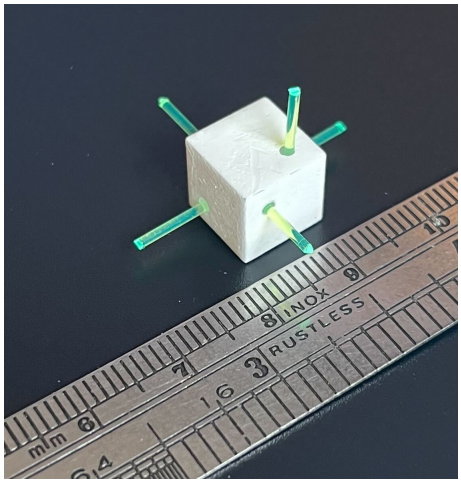


Figure 4.2: A photo showing a SuperFGD cube and three WLS fibres, one threading through each orthogonal holes.

4.1.2 Wavelength-Shifting (WLS) Fibres

The WLS fibres are used to collect and transport the scintillation light emitted by the SuperFGD cubes by absorbing the light and re-emitting it at a longer wavelength (see Figure 4.3 left). The SuperFGD uses the Y-11(200) variant produced by Kuraray Co., Ltd, which is the same as those used by the other ND280 detectors.

The Y-11 WLS fibre has a round cross-section with a diameter of 1 mm. It is also multi-cladded, with each layer having a different refractive index and chemical composition [85].

4.1.3 Multi-Pixel Photon Counters (MPPCs)

The SuperFGD MPPC (S13360-1325PE, [86]) is a type of silicon photomultiplier (SiPM) designed and manufactured by Hamamatsu Photonics. Compared to the MPPCs used by other ND280 subdetectors, the SuperFGD MPPC has a larger sensitive area of 1.3×1.3 mm^2 and contains more pixels (2668). It

[a] POPOP stands for 1,4-bis(5-phenyloxazol-2-yl) benzene.

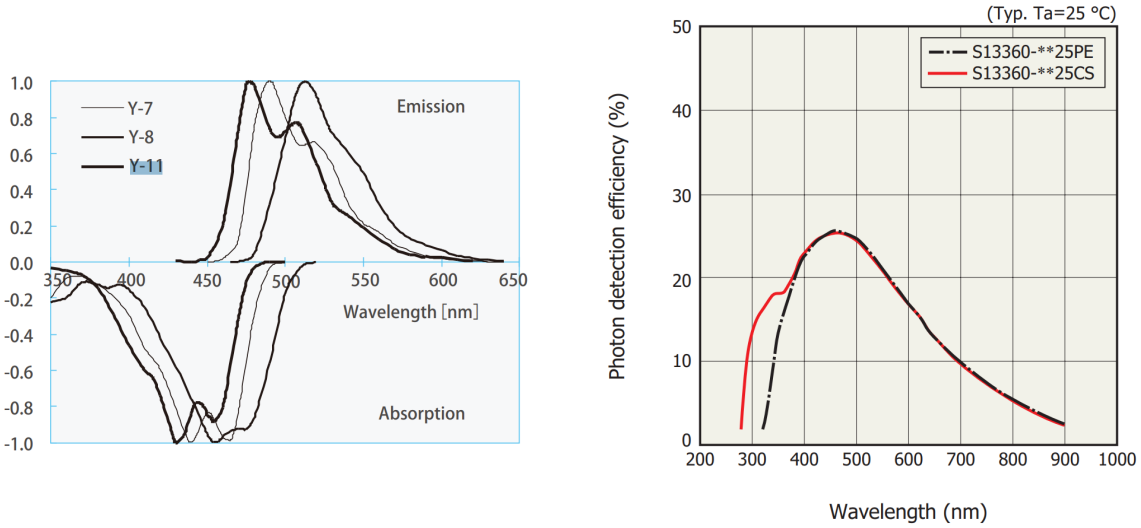


Figure 4.3: The left plot shows the normalised absorption and emission spectra of the WLS fibres [85] and the right plot shows the photon detection efficiency, defined as the ratio of the detected photons to the incident photons, of the SuperFGD MPPC (S13360-1325PE, [86]). Note that the POPOP emission peak wavelength at ~ 430 nm roughly coincides with the Y-11 absorption spectrum peak, and the Y-11 emission wavelength is close to the MPPC efficiency peak.

also has the advantages of possessing a lower dark count rate at 70 KHz and a lower crosstalk probability of 1%. The SuperFGD MPPCs are bundled as an 8×8 array on an MPPC-PCB (Figure 4.4), which, when mounted on the detector, will be in optical contact with 64 fibre connectors, as shown in Figure 4.5.

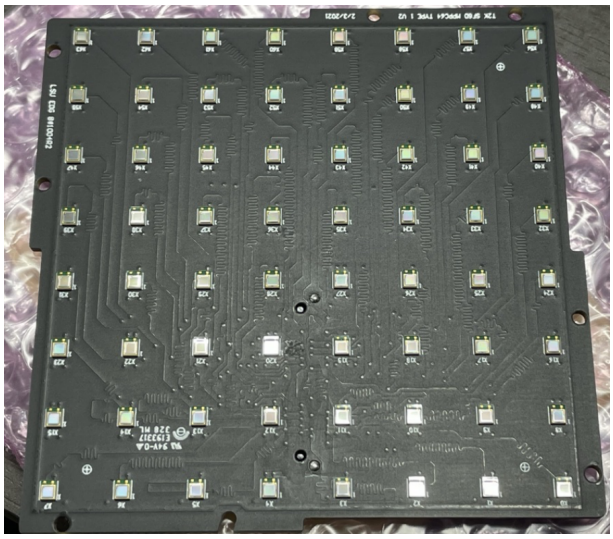


Figure 4.4: An MPPC-PCB containing an 8×8 array of MPPCs [87].

An MPPC is essentially a 2D array of photon-counting 'pixels' each made up of an avalanche photodiode (APD) in Geiger mode and a quenching resistor[b]. Each pixel generates only one pulse whose amplitude is independent of the number of incident photons; it is therefore possible to saturate an MPPC when a large quantity of photons arrive at the same pixel within a very short acquisition time window, causing the measured pulse charge to respond non-linearly to the number of incident photons.

[b] A quenching resistor is a resistor in series to an APD, preventing the continuous Geiger discharge that would otherwise occur upon detecting an incident photon.

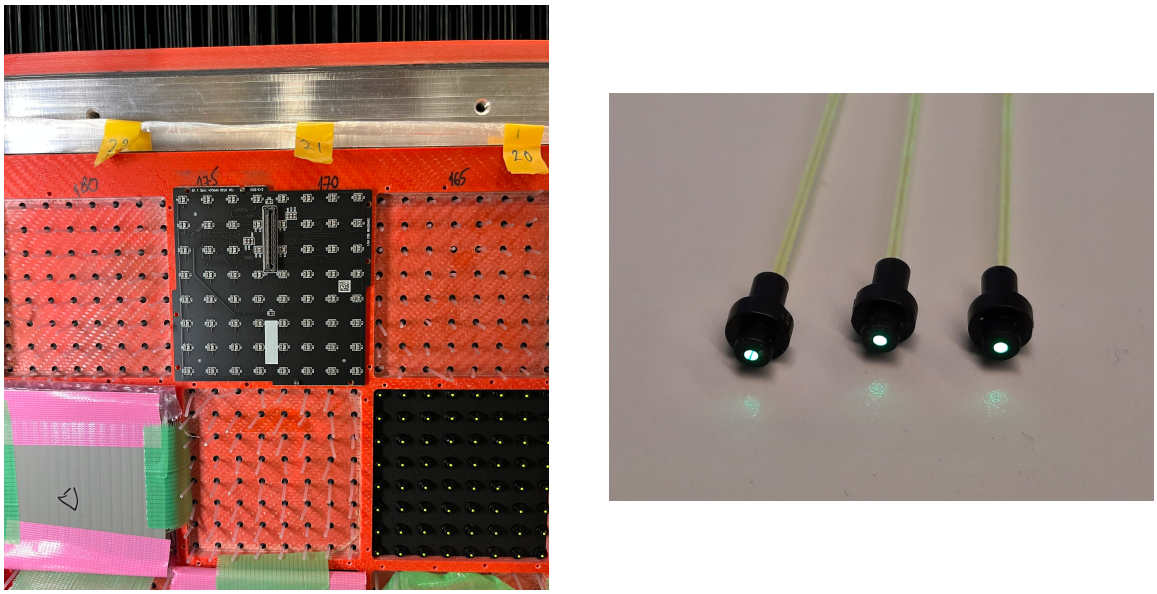


Figure 4.5: Left photo showing the side panel of the SuperFGD detector. The bottom black square shows 64 WLS couplings (three of which are shown in the right photo [88]) pinning a thin black elastic foam to the red detector panel. The foam will ensure good optical contact with the 64 MPPCs mounted on an MPPC-PCB, as shown by the top black square. Note the protruding white fibres are fishing lines, which were used as placeholders that provided structural stability, waiting to be replaced by WLS fibres.

The MPPC charge gain M is defined as the number of charge carriers in a pulse when a photon is detected,

$$M \equiv \frac{Q}{Q_e}, \tag{4.1}$$

where Q is the charge in one pulse, and Q_e is the electric charge of an electron [89].

4.1.4 SuperFGD Read-Out Electronics

At the level of information processing, the most fundamental unit is the 'Front-End Board' (FEB). Each FEB houses and processes the data transmitted from eight Cherenkov Imaging Telescope Integrated Read-Out Chips (CITIROCs), and two CITIROCs are connected to one MPPC-PCB (64 MPPC channels). Up the information processing chain is the Optical Concentrator Board (OCB), which connects 14 FEBs forming a 'crate'. In total, there are 16 OCBs on the SuperFGD, and all of them are connected to the data-acquisition computers (DAQ PCs). The 16 OCBs are also connected to a Master Clock Board (MCB) responsible for triggering, timing, and synchronisation, as shown in Figure 4.6. The maximum channel capacity is therefore $16 \times 14 \times 4 \times 64 = 57{,}344$ channels, and the total number of fibres is $192 \times 184 + 184 \times 56 + 56 \times 192 = 56{,}384$.

In a CITIROC, each MPPC signal is split into two paths defined by their starting adjustable pre-amplifier: the High Gain (HG) path and the Low Gain (LG) path. The amplification of each pre-amplifier is controlled by a digital-to-analogue converter (DAC) parameter between 0 and 63 (inclusive), and it is denoted as $HG40$ when the HG amplification is set to 40, and similar for the LG path, for instance.

Both the HG and the LG paths are equipped with a slow shaper (SSH) which is responsible for

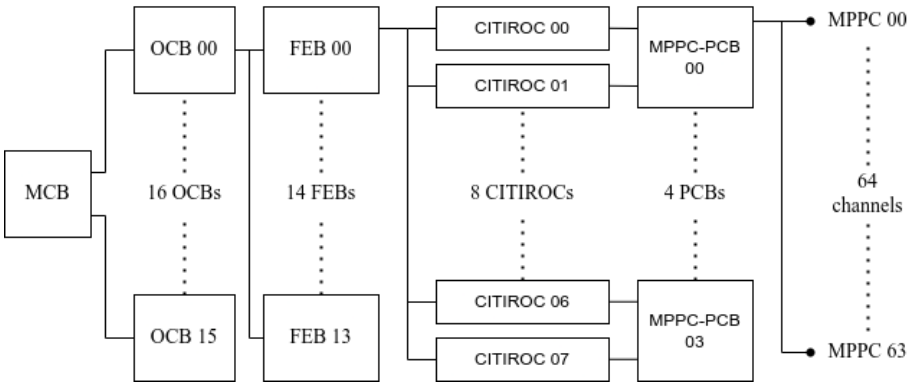


Figure 4.6: A diagram showing the hierarchical structure of the SuperFGD electronics. A Master Clock Board (MCB) controls 16 Optical Concentrator Boards (OCBs), and each OCB connects to 14 Front-End Boards (FEBs), which contains eight Cherenkov Imaging Telescope Integrated Read-Out Chips (CITIROCs). Two CITIROCs are required to process one MPPC-PCB, each contains 64 MPPC channels.

transforming the incoming pulse into a suitable waveform. After the shapers, the analogue signals are sampled and digitised by the 12-bit analogue-to-digital converter (ADC) on the FEB, and finally sent off to the FEB Field Programmable Gate Array (FPGA).

The timing information of a signal is managed by the Time-over-Threshold (ToT) data path in a CITIROC, which takes in either the HG or LG pre-amplified information and passes it through a fast shaper (FSH), followed by a threshold-adjustable discriminator. The FEB FPGA directly samples the signal at a frequency of 800 MHz by recording the times when the signal rises above and falls below the discriminator threshold. Additionally, the difference between the rising and falling timestamps provides a third charge amplitude measurement. All three read-out paths are illustrated in Figure 4.7.

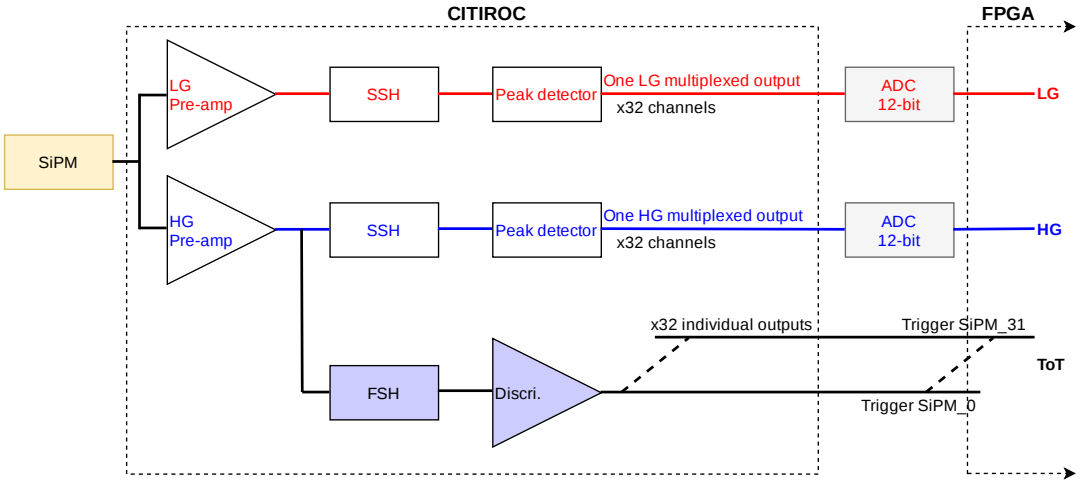


Figure 4.7: The three read-out paths of the CITIROC [90]. The fast shaper (FSH) can be configured to either the LG or the HG path.

4.1.5 LED Calibration System

A dedicated LED calibration system is installed on the opposite walls to those where the MPPC-PCBs are. It provides a controlled light source for the calibration of HG and pedestal[c].

[c]The calibration methods will be described in detail in Section 4.2.

The LED calibration system comprises a set of light guide plates (LGPs) and LED driver boards, which control the LED pulse shape. Each driver board is connected to the DAQ system via an ethernet board. The LGPs are made of acrylic plates laser-etched with arrays of notches at which the LED light is scattered. The notches are distributed correspondingly to every WLS fibre, as illustrated in Figure 4.8.

The calibration light is produced by a strip of blue LED bulbs spaced at 1 cm intervals at the end of the LGPs. The LED light passes through a collimator, scatters off the notches, and passes through a diffuser layer made of a translucent white acrylic plate before entering the fibres. The diffuser sacrifices the peak LED intensity but ensures that the off-centred fibres can receive sufficient calibration light. On average, the LGP modules provide $\sim$ 2.5 photoelectrons (p.e.) A visual comparison between the LGP modules with and without a diffuser can be found in Figure 4.9.

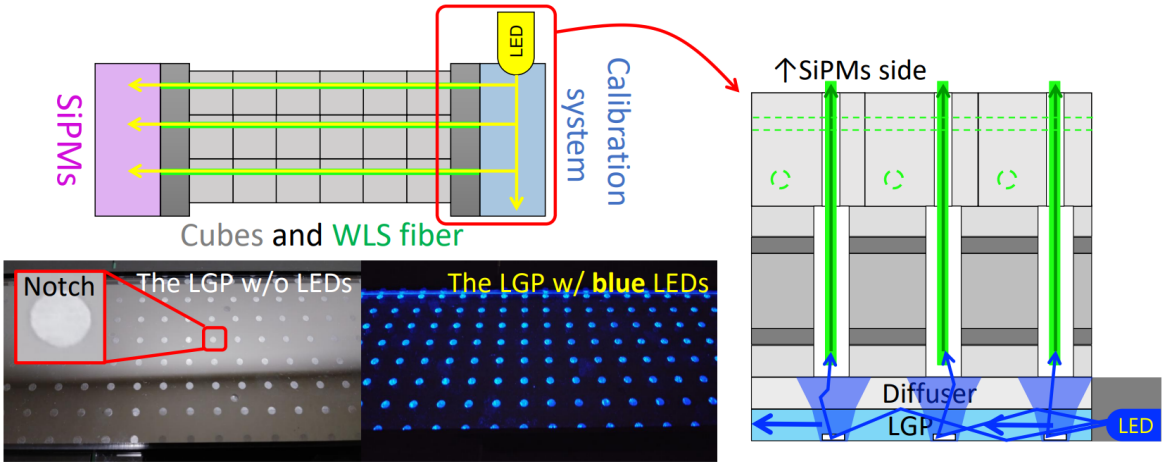


Figure 4.8: An illustration of the SuperFGD LED calibration system [91]. Each fibre is paired with a LED diffuser notch that is etched directly onto the LGP.

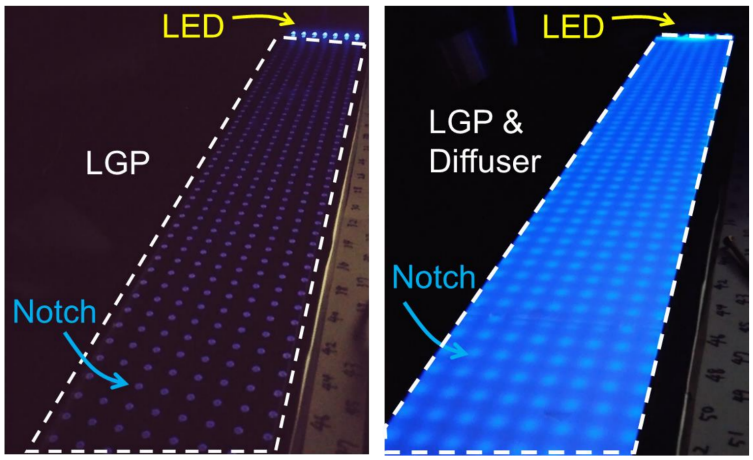


Figure 4.9: A comparison showing the effect of the diffuser layer on the LGP light [92]. The diffuser increases the tolerance on the horizontal WLS fibre displacement.

4.2 SuperFGD Charge Calibration

This section includes both original calibration methods and those improved from the prototype study [90]. Unless otherwise specified, the results presented here are produced by the software package developed by me, but the ND280 software framework which the package belongs to is the work of many ND280 group members.

The scintillation light received by an MPPC is transmitted as an electric pulse to a CITIROC, where the signal is processed through three paths: the HG path, the LG path, and the ToT path. The HG path has the finest resolution but saturates[d] quickly; the LG path has a wider dynamic range but loses the fine resolution. The signals are amplified respectively before being digitised by the ADC. These processes introduce a digitisation dead-time of 9.7 μm following each acquisition window whose duration is of comparable length (~ 40 μm). And since each acquisition window can only record one HG and one LG value, the ToT path, which utilises only the timing information, can be exploited to overcome the blackout.

'Calibration constants' need to be extracted for each of the three read-out paths and for each MPPC individually to 'translate' the ADC values into the more physically meaningful unit of photoelectrons (p.e.). The formula to convert an HG ADC reading to the corresponding p.e. is

$$N_{\text{p.e.}} = \frac{ADC - P}{G_{\text{HG}}}, \tag{4.2}$$

where $N_{\text{p.e.}}$ is the number of p.e., P is the pedestal[e], and G_{HG} is the 'circuit gain' (or simply 'the gain'), distinct from the MPPC gain. Note that all quantities on the right are in the scale of HG ADC.

With the three read-out channels, we can potentially produce three different $N_{\text{p.e.}}$ measurements of a hit by following the calibration routes below:

- HG: HG $\rightarrow N_{\text{p.e.}}$ (the HG calibration),
- LG: LG $\rightarrow$ HG $\rightarrow N_{\text{p.e.}}$ (the LG calibration),
- ToT: ToT $\rightarrow$ HG $\rightarrow N_{\text{p.e.}}$ (the ToT calibration).

The processes of converting the read-out values to the measurements of $N_{\text{p.e.}}$, along with the pedestal calibration, which will also be described, are collectively referred to as the SuperFGD charge calibration. In the following subsections, the fitting methods for obtaining the calibration constants of the above calibration routes are described.

[d] Note, this saturation is not caused by multiple incident photons hitting the same MPPC pixel, but rather, by the finite current supplied by the capacitors on the CITIROC.

[e] A pedestal is formed by events with 0 p.e. signals, which are data read out when no charge is deposited.

4.2.1 Extracting HG Calibration Constants

To measure the charge deposition using the HG ADC path with Equation (4.2), one needs to find the HG gain G_{HG} and the pedestal P. G_{HG} can be extracted from the HG ADC distribution, which shows the charge deposition (measured in HG ADC) of the LED light hits generated by the calibration system. An example distribution can be seen in Figure 4.10.

The number of LED photons detected follows a Poisson distribution, and each Poisson bin is also smeared roughly following a Gaussian distribution. Therefore, multiple evenly-spaced peaks can be seen in an ADC distribution. Such a plot is colloquially called a 'finger plot'. G_{HG} is obtained by measuring the spacing between two consecutive p.e. peaks, denoted as G in Figure 4.10.

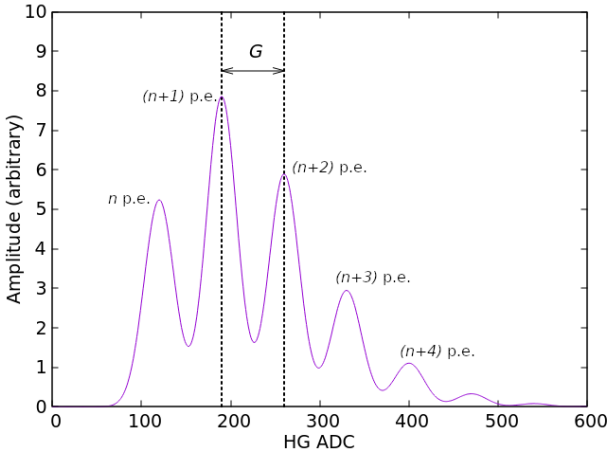


Figure 4.10: An illustration of a mock finger plot with a gain of $G = 70$ ADC/p.e. The pedestal (zero-p.e. peak) is, in general, not visible in a SuperFGD MPPC finger plot due to the threshold effect.

The 'Multi-Peak' Method

The current algorithm in use is the 'multi-peak' method, which looks for all suitable peaks and fits each with a Gaussian function to find the peak centres. These peak centres, when plotted against the peak numbers, can be described by a linear function whose slope gives the gain.

Several factors are considered when selecting suitable peaks to include in the fit. The first step of the selection process is to pick out the peak candidates using a 1D high-resolution peak search tool provided by the `ROOT` library [93, 94, 95]. The algorithm is based on smoothed second derivatives[f] and the ratios to their standard deviations. The search algorithm can optionally replace the source spectrum with a new spectrum obtained from a method [96] that is based on discrete Markov chains inspired by the quantum-tunnelling effect where two points on each side of a peak are compared, achieving a smoothing and enhancing effect of the peaks. Next, the peak candidates are subsequently subjected to various examinations to weed out potential misidentified noise and real peaks with poor quality. The

[f]Specifically, it is based on the second 'differences' where the quantities $dd_i \equiv n_{i+1} - 2n_i + n_{i-1}$ (n_i being the number of events in bin i) are considered.

peak features, such as the amplitude, width, distances between neighbours, and neighbours' amplitudes, are considered in the selection process. An example of a typical fit result can be found in Figure 4.11.

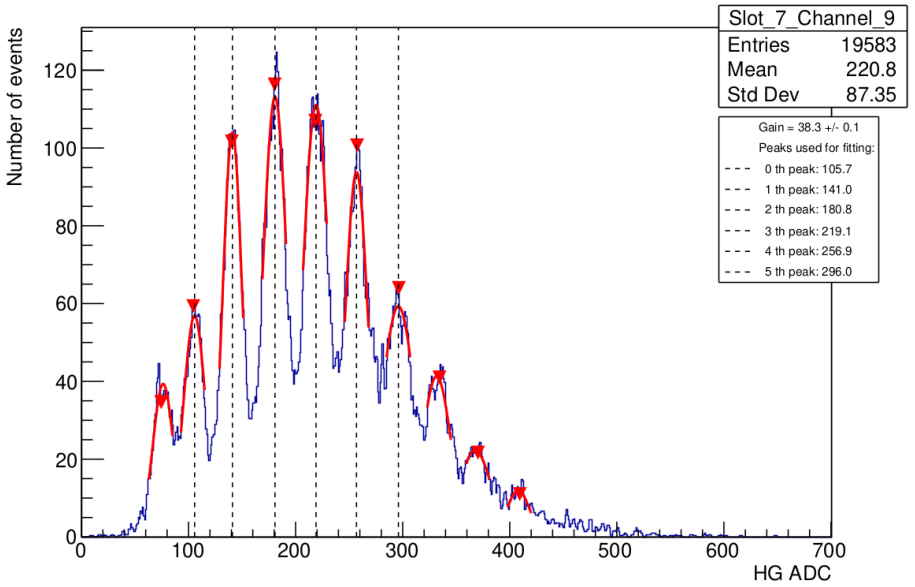


Figure 4.11: An example of a fit result using the 'multi-peak' method on a typical LED calibration finger plot. The last three peaks are discarded and not used in the gain fitting, according to an algorithm that takes the fit quality and the spacing between neightbouring peaks into account.

With the identified peak position in the ADC unit, we can relate them with the peak number and fit a linear function through the points. The slope gives an estimation of the gain G, as shown in Figure 4.12.

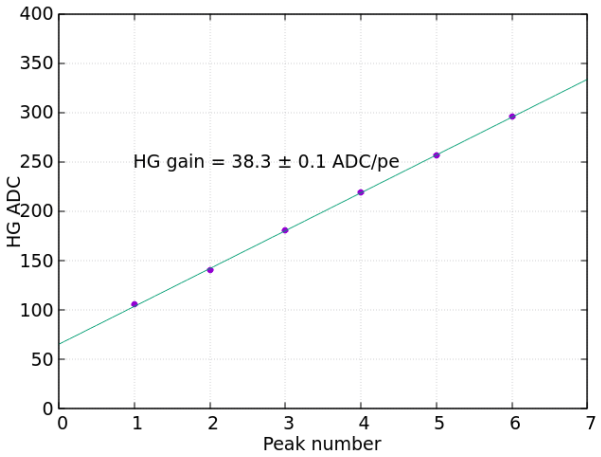


Figure 4.12: A plot showing a linear fit to the 'peak number-ADC' plot. The slope of the linear function is the gain (ADC/p.e.) of the channel. The errorbars are included but too small to be seen.

The 'Autocorrelation' Method

In addition to the aforementioned 'multi-peak' method, an autocorrelation-based fitting algorithm was developed as an alternative backup. This autocorrelation algorithm is described here.

The autocorrelation algorithm first starts by selecting a subsegment from a finger plot called the 'sampler'. The sampler at minimum includes two fingers within its range and it is typically selected from the low ADC region where the fingers are more distinct, as shown in Figure 4.13. Starting from the low

ADC end of a finger plot, the selected sampler is shifted towards the high ADC direction one bin at a time. After shifting i bins, the correlation ρ_i between the sampler, denoted as X, and the finger plot segment covered by the sampler, denoted as Y, is computed using the formula

$$\rho_i = \frac{\mathrm{Cov}(X,Y)}{\sigma_X \sigma_Y}, \tag{4.3}$$

where $\mathrm{Cov}(X,Y)$ is the covariance, and σ's are the standard deviations. In terms of expected values $\mathbb{E}$, Equation (4.3) can be rewritten as

$$\rho_i = \frac{\mathbb{E}(XY) - \mathbb{E}(X)\mathbb{E}(Y)}{\sqrt{\mathbb{E}(X^2) - \mathbb{E}(X)^2}\sqrt{\mathbb{E}(Y^2) - \mathbb{E}(Y)^2}}. \tag{4.4}$$

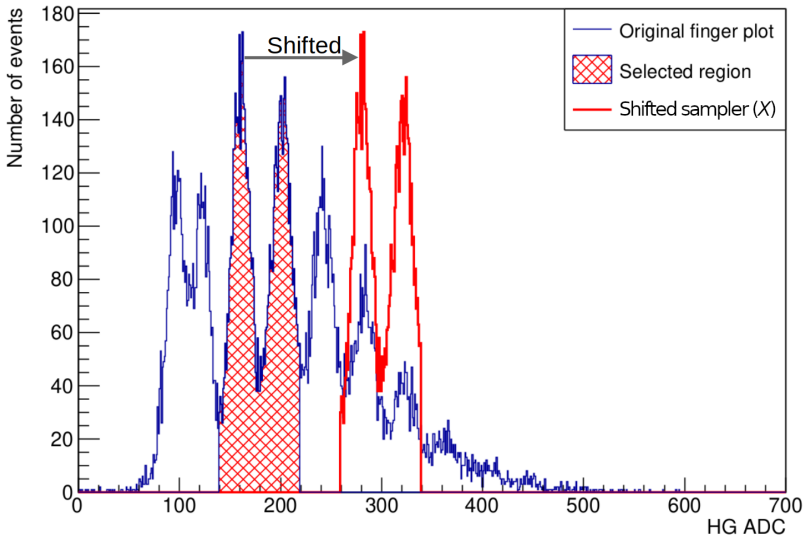


Figure 4.13: A plot showing a shifted sampler segment. When the peaks align, the correlation between the sampler and the original finger plot is high. Note the first two peaks are affected by the threshold and are therefore discarded.

When the peaks in the sampler segment match those in the original finger plots, the correlation score will be large, and when the peaks in the sampler coincide with the troughs, the correlation score is small. Plotting the correlation score $\frac{1}{2}(\rho_i + 1)$ as a function of the shift i produces a correlation finger plot where the smaller peaks are enhanced, as shown in Figure 4.14. The period of the fluctuation is an estimate of the gain, but this plot can also be fed back to the multi-peak method to estimate the gain.

4.2.2 Extracting Pedestal Calibration Constant

The pedestal of a channel is the HG ADC of the zeroth p.e. peak. Due to the ADC threshold of the SuperFGD, the zeroth peak cannot be directly observed in a finger plot. Instead, to locate the pedestal, multiple finger plots collected with different HG settings (either gain or voltage) are needed in the analysis. Since the change of HG settings should not affect where the pedestal is, by extrapolating the peak positions linearly and shifting the apparent 'peak number'-'p.e. number' [g] correspondence, one can locate the pedestal by extrapolating the peak numbers back to the y-axis, as demonstrated in Figure Figure 4.15.

[g] The 'peak number' refers to the numberings of the identified peaks in a finger plot, while the 'p.e. number' refers to the actual numbers of photoelectrons corresponding to the peaks.

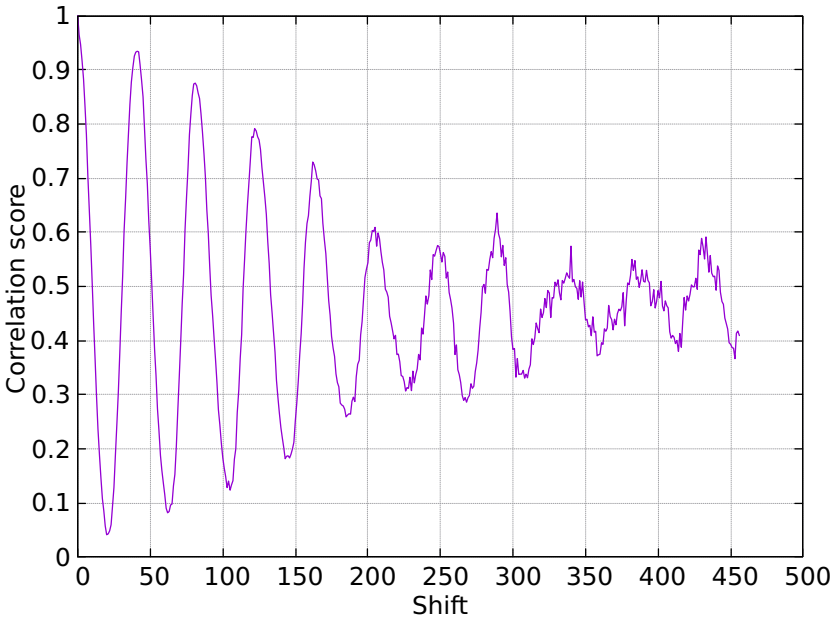


Figure 4.14: The autocorrelation of the finger plot in Figure 4.13. Since the shift is of the same scale as the finger plot (HG ADC unit), the spacing between the peaks provides a measure of the gain. Note, the process also enhances the small peaks in the high ADC region.

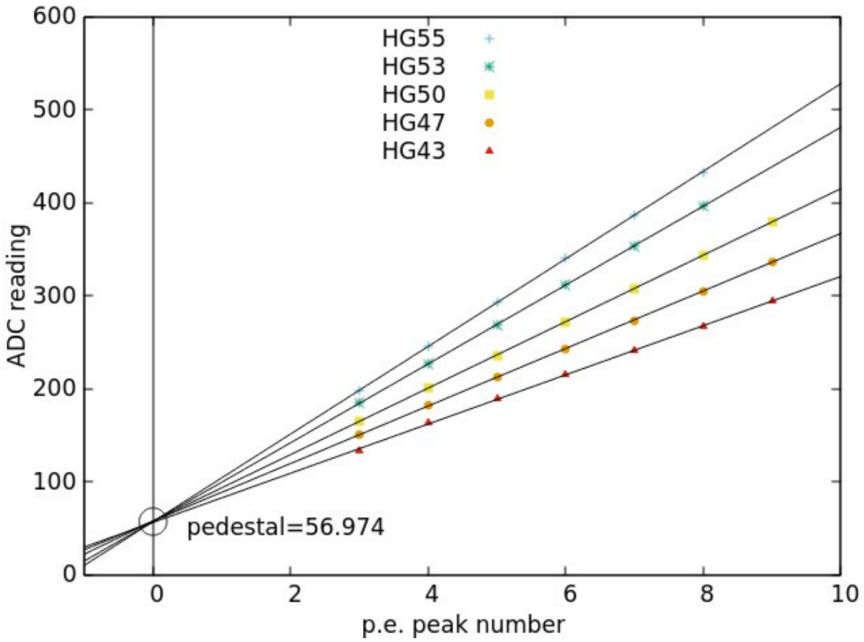


Figure 4.15: A demonstration of the pedestal search algorithm. By varying the HG setting (HG43, HG47, etc.), one produces finger plots of different gains, which can be seen by the change of slope over different HG settings. Since the pedestal position is not affected by the gain setting, the point at which all lines converge should correspond to the location of the pedestal.

The pedestal algorithm conducts the search for the pedestal ADC by minimising the spread of y-intercepts made by finger plot lines and the y-axis. It works by first assuming a 'peak number'-'p.e. number' correspondence and shifting the lines of extrapolation horizontally to minimise the spread of the intercepts with the y-axis. The average of those y-intercepts with the configuration that minimises the spread is taken to be the pedestal.

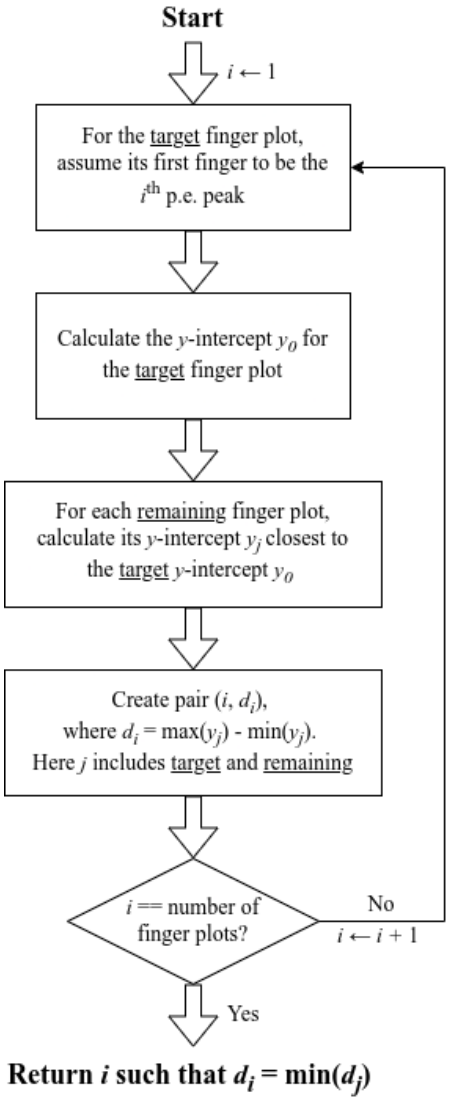


Figure 4.16: A flowchart explaining the pedestal search algorithm. The algorithm returns the best possible p.e. number corresponding to the first peak of the target finger plot, where the configuration minimises the spread of the y-intercepts.

Figure 4.16 shows a flowchart of the algorithm steps. The algorithm first selects the first finger plot as the 'target' and calculates its y-intercept (y_0) under the assumption that it is the i^{th} p.e. peak. For the remaining plots, it calculates the closest possible y-intercepts and the shifts required. Since the peak numbers are strictly integers, the best shift s for each finger plot can be calculated analytically using the formula,

$$s = \text{round}\left(\frac{y' - y_0}{G}\right), \tag{4.5}$$

where round() rounds a value to the nearest integer and y' is any reference y-intercept (e.g. obtained by assuming the first finger is the first p.e. peak) to which the shift is relative. Hence, the closest y-intercept of this particular peak is

$$y = y' - sG. \tag{4.6}$$

For each configuration i, there is a y-intercept spread defined by the difference between the maximum and minimum y-intercepts. The y-intercepts of the configuration that yields the least spread are averaged

and taken as the pedestal.

In some cases, the actual points of intercepts do not sit on the y-axis; hence, there exists a discrepancy between the average y-intercept and the actual intercept. To account for this, a second value, calculated by averaging the points of intercepts produced by all pairs of finger plots, is also provided in the pedestal map.

4.2.3 Extracting LG Calibration Constants

The LG calibration constants are the coefficients of the function that relates the LG ADC value to the HG ADC value of a given hit. Before saturation, the HG and LG ADC measurements are linearly correlated, ie,

$$A_{\mathrm{LG}} = c_1 A_{\mathrm{HG}} + c_0, \tag{4.7}$$

where A_{LG} and A_{HG} are the LG and HG ADC values respectively, and the c coefficients are the desired LG calibration constants. Therefore, to extract the LG calibration constants, a linear function is fitted to the unsaturated region of a 'HG vs LG plot', as shown in Figure 4.17. This extraction process is conducted for each channel individually, and the obtained calibration constants are applied to convert a LG ADC measurement to HG following the equation:

$$A_{\mathrm{LG}\to\mathrm{HG}} = \frac{A_{\mathrm{LG}} - c_0}{c_1}. \tag{4.8}$$

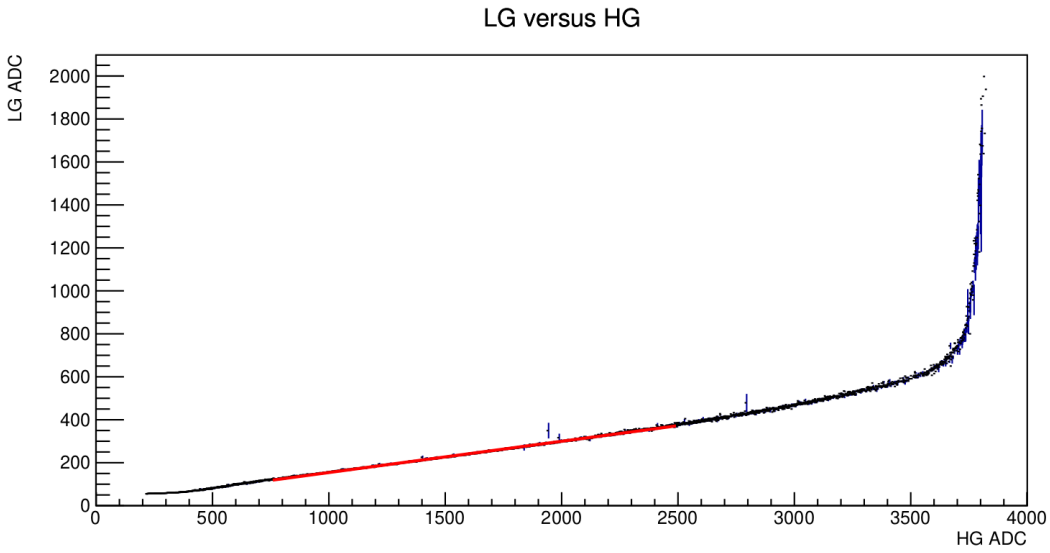


Figure 4.17: The HG and LG ADC readings of each hit on a channel, as well as the linear function that relates the LG and HG values, are plotted. The parameters of the linear function can be used to convert a LG measurment to HG. The non-linear region at the higher HG ADC region is a result of saturation. The data shown here were collected from the SuperFGD prototype beam test at CERN [90].

To define the range of the unsaturated region, the result from a previous study [97] examining the non-linearity response of HG and LG to the input amplitude was used. In this previous study, a pulse generator is used to directly inject different amounts of charges into the FEB. The non-linearity of the

response to the injected charges is quantified by ϵ_r, which is defined as

$$\epsilon_r = \frac{\Delta(\text{ADC})}{\text{Included ADC range}}, \tag{4.9}$$

where the denominator is the ADC range included in a linear fit and Δ(ADC) is the deviation from that linear function. For each data point, the non-linearity is computed. The result is summarised in Figure 4.18. In the LG calibration, the HG non-linearity cutoff is set to 1%, which corresponds to ~ 2500 HG ADC.

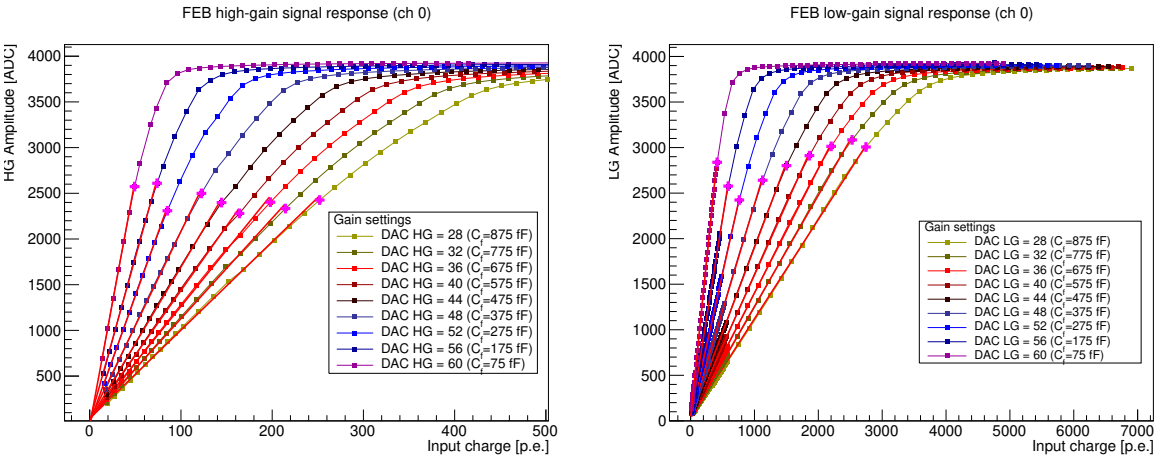


Figure 4.18: The 1% non-linearity points (marked as magenta crosses) of different gain settings, above which the non-linearity of ADC measurements responding to the injected charge is larger than 1% [97]. Each line shows the response of HG or LG measurement to the injected charges provided by an external generator, given a fixed gain setting. The unit of the charge injected was converted to p.e. for the convenience of reading. The bounds of the unsaturated region is defined according to the result.

The extraction of the LG calibration constants does not rely on the LED calibration light source. Different from the HG calibration, the LG calibration cannot utilise on the light provided by the LED calibration system, whose energy range is insufficient to cover the LG dynamic range[h]. The LG finger plot is also not useful for calibration since the fingers are not resolved. Instead, LG calibration relies on self-calibration, where the collected data are used to calibrate itself during each given time period. The data source can be from the beam or from cosmic or sand muons.

4.2.4 Extracting ToT Calibration Constants

Similar to the LG calibration, ToT calibration constants needed to convert ToT values into measurements of $N_{\text{p.e}}$ are extracted from detector data.

In general, each MPPC hit consists of three read-out values, the HG, LG, and ToT. Hence, in terms of converting ToT values into $N_{\text{p.e}}$, it may seem natural to consider each calibration route (ToT $\rightarrow$ HG and ToT $\rightarrow$ LG) separately. However, the approach comes with several drawbacks. For example, in both conversion routes due to the saturation effects, ToT responds highly non-linearly to the change of ADC value towards the end of the distribution, as shown in Figure 4.19, which makes the fits for the regions

[h]The current LG setting measures up to ~ 600 p.e.

complicated and perform poorly at high HG and low LG ADC regions. It also requires a larger storage space since the approach produces many time-dependent calibration constants.

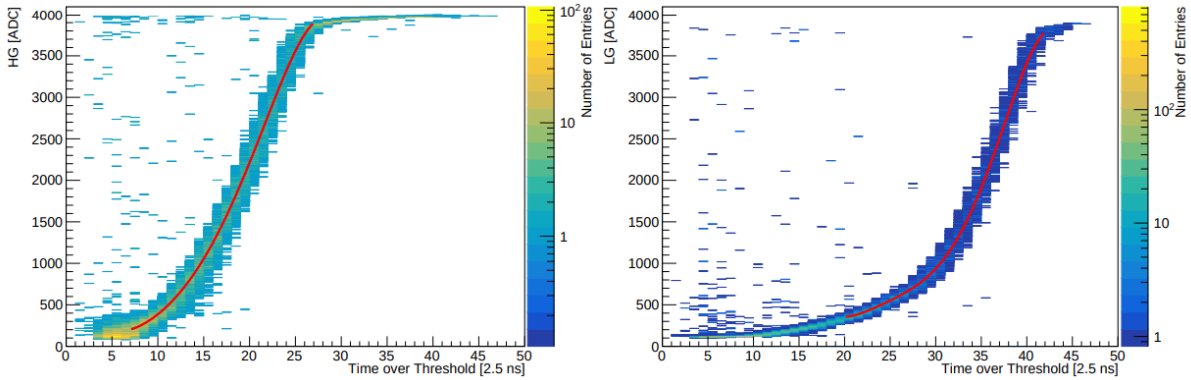


Figure 4.19: An example result of a ToT calibration using two separate calibration routes [90] used in the SuperFGD prototype beam test. The method fits each distribution with a polynomial of degree five, and it is less effective at calibrating the high HG and low LG regions. The method also generates a large number of calibration constants, potentially causing a storage problem in the long run.

To improve the fit quality in the transition between HG and LG, and to smoothly map the whole ToT range to some ADC values, the ToT calibration constants can be extracted using a combined ToT $\rightarrow$ (HG & LG) method as an alternative. In the ToT $\rightarrow$ (HG & LG) method, the LG values of MPPC hits are first calibrated following LG $\rightarrow$ HG as described in Section 4.2.3, so they are on the same scale as the HG values. The calibrated LG values are then combined with the HG values to produce the combined measurements. In this study, a weighted average based on the resolution is proposed. For each MPPC hit, if

- HG $<$ 2500 (blue points in Figure 4.20), HG and LG are weight-averaged by the relative resolution. $W_{\mathrm{HG}} = 1, W_{\mathrm{LG}} = \frac{1}{m^2}$, where W's are the weights, and m is the relative resolution. The relative resolution can be determined from the slope of the linear function used for the LG $\rightarrow$ HG calibration.
- 2500 $\leq$ HG $<$ 3000 (green points in Figure 4.20), similar to the above procedure, but W_{HG} drops quadratically from 1 to 0 as HG goes from 2500 to 3000.
- HG $\geq$ 3000 (red points in Figure 4.20), only the scaled LG is selected.

An example result using the combined method is shown in Figure 4.20. The combined (HG & LG) method produces a smoothly growing response curve with ToT. The transition from heavily weighting on the HG side in the low ADC region to gradually decreasing the importance and eventually discarding the saturated HG completely helps reduce the calibration difficulty at the transitional region. Several fit functions are tested, and for a smooth response curve, it is determined that a fourth-order polynomial is sufficient, as shown in Table 4.1.

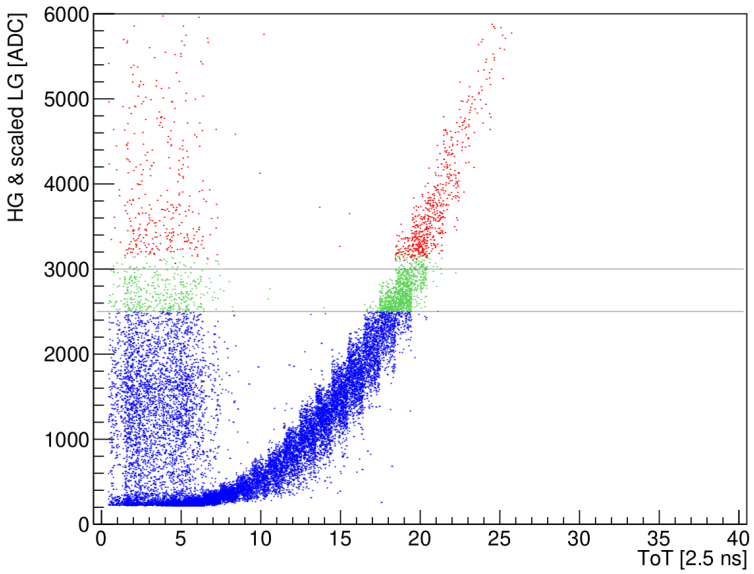


Figure 4.20: An example of a ToT vs (HG & LG) plot using the SuperFGD prototype data. The blue region contains hits whose HG and LG are averaged, weighted by the respective resolutions. The green region combines HG and LG readings similar to the blue region, but the weight of HG is continuously reduced to zero as HG increases. The red region contains only the LG readings. Note the noisy events distributed across ToT < 7 is a result of the miss-tagging of timing information, a firmware bug unique to the prototype data which was fixed in the later firmware releases.

Table 4.1: Reduced χ^2 values of various fit functions

Fit function	χ^2/N.D.F.
Polynomial (5^{th} degree)	4.34
Polynomial (4^{th} degree)	4.58
Polynomial (3^{rd} degree)	8.36
Polynomial (2^{nd} degree)	10.56
Exponential ($Ae^{B+Cx} + D$)	14.16

4.3 Other SuperFGD Calibration Tasks

Apart from the MPPC and CITIROC charge calibration described in Section 4.2, various other SuperFGD properties need to be measured to ensure the correct operation of the detector.

4.3.1 High-Voltage Trimming

The HG gain is sensitive to the ambient temperature, with a rate of change of approximately -0.1 ADC/p.e. per 1°C increase. As the temperature increases, the vibrations of the MPPC crystal lattice become stronger, which increases the difficulty of a charge carrier accelerating and triggering the avalanche effect. Consequently, the MPPC gain is reduced. Therefore, during the detector's operation, the HG gain needs to be tuned to maintain a suitable value that balances the dynamic range and the sensitivity. This is achieved by performing a 'high-voltage (HV) trim', where the MPPC operating voltage, V_{op}, is adjusted. This operation will be described in this section.

For a channel that is initially tuned to 22 ADC/p.e., over time the gain will typically drift within a ±2 ADC/p.e. window due to the fluctuation of temperature. Within this typical drift window, $G_{\mathrm{HG}} \propto V_{\mathrm{op}}$, as shown in Figure 4.21. It is therefore straightforward to determine the correct V_{op} at a given temperature by performing a 'HV scan' where the V_{op} is sampled about a typical value and interpolating the measurement. The desired V_{op} value can subsequently be configured during detecter maintenance[i]. A comparison before and after performing a HV trimming can be seen in Figure 4.22.

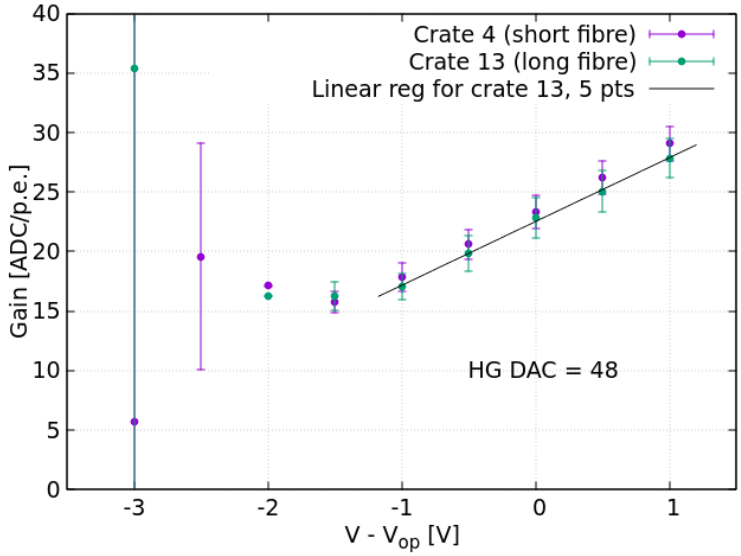


Figure 4.21: The HG gain responds to the change of operating voltage linearly with the typical gain range created by temperature fluctuation. The data points on the left side of the figure show inaccurate results due to the unrealistic V_{op} setting.

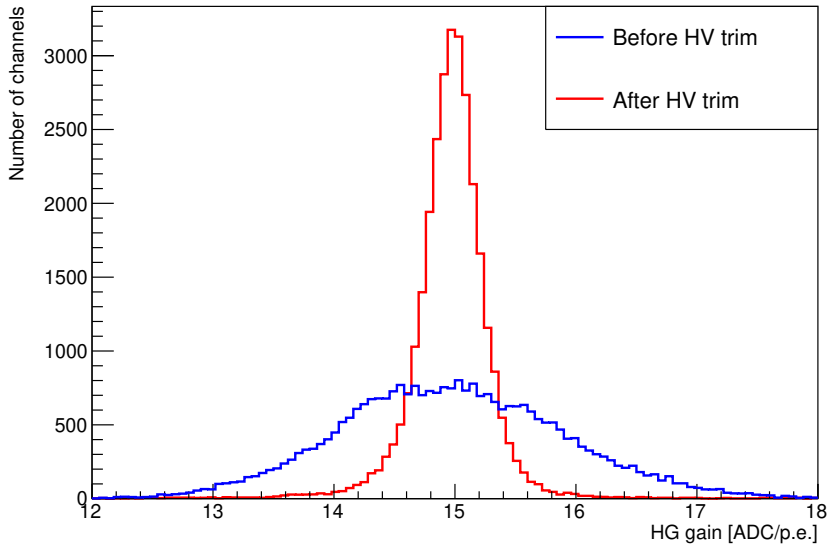


Figure 4.22: A comparison between G_{HG} distributions before and after the HV trimming. The target gain is set to 15 ADC/p.e. in this example.

[i]More specifically, all 32 MPPCs belonging to a CITIROC share a common V_{base}, but they can be additionally configured with a channel-specific ±2.5 V voltage shift ΔV to achieve the desired V_{op}, which equals the sum $V_{\mathrm{base}} + \Delta V$.

4.3.2 Cube-Related Calibration

How a scintillator cube responds to the energy deposition is one of the most fundamental properties that directly impact the performance of the detector hence the correct calibration of the scintillation efficiency, S,[j] is vital. The scintillation efficiency is the proportionality constant that links the light yield L to the energy deposited. It is usually measured by selecting cosmic muon tracks of different orientations, which are used to obtain an intermediate quantity of p.e. per minimum ionising particle (MIP). This can then be converted to the desired quantity of p.e./MeV.

The measured light yield is affected by the scintillator quenching effect. The quenching effect is a detector-specific property due to its intrinsic light production saturation, where the light yield $\frac{\mathrm{d}L}{\mathrm{d}x}$ is no longer proportional to the energy deposition per path length $\frac{\mathrm{d}E}{\mathrm{d}x}$. The effect is especially prominent in high-energy loss cases, where the light production efficiency is decreased due to the high ionisation density leading to saturation. Empirically, the quenching effect can be described by the Birks' law [98],

$$\frac{\mathrm{d}L}{\mathrm{d}x} = S\frac{\frac{\mathrm{d}E}{\mathrm{d}x}}{1 + k\frac{\mathrm{d}E}{\mathrm{d}x}}, \tag{4.10}$$

where S is a linear constant that characterises the relationship in the low energy regime, and k is the Birks' constant specific to the scintillator material. For the SuperFGD simulation software, $k = 0.0208$ cm/MeV.

The optical crosstalk, which refers to the light leakage from one cube to its neighbours, is also a factor that needs to be considered. Despite the white coating applied to the SuperFGD cube surfaces, preliminary measurements showed that the effect is at the level of $\sim 3.5\%$ and, therefore, is not negligible.

4.3.3 Fibre-Related Calibration

There are two main WLS fibre factors that affect the performance of SuperFGD: attenuation along the fibres and reflection at the fibre ends.

The light attenuation as photons travel along the WLS fibres is characterised by a long- and a short-distance decay with an attenuation length of D_L and D_S, respectively. The attenuation affects both the direct and the reflected light signals. Specifically, the light yield $L(d)$ (measured in number of p.e.) at a distance d away from the hit cube, where a signal of light yield L_0 is emitted, is given by the equation

$$L(d) = L_0\left\{\underbrace{\left(\alpha e^{-\frac{d}{D_L}} + (1-\alpha)e^{-\frac{d}{D_S}}\right)}_{\text{direct light}} + R\underbrace{\left(\alpha e^{-\frac{2D-d}{D_L}} + (1-\alpha)e^{-\frac{2D-d}{D_S}}\right)}_{\text{reflected light}}\right\}, \tag{4.11}$$

where the coefficient $0 \leq \alpha \leq 1$ is introduced to weight the contribution, the R is the fraction of light reflected, and D is the fibre length.

These parameters are determined from fits and will be applied to correct for the fibre effects on the charge measurements.

[j] This is occasionally called the 'light yield'. The term 'light yield' can refer to a multitude of different but similar properties. It could sometimes refer to the 'simple' light yield L which refers to the amount of light generated (often measured in $N_{\text{p.e.}}$), the light produced per particle track length $\frac{\mathrm{d}L}{\mathrm{d}x}$, or the light produced per energy deposition $\frac{\mathrm{d}L}{\mathrm{d}E}$. Instances where potential confusion can occur, the mathematical symbol will follow the mention of 'light yield' for clarity.

4.3.4 Timing Calibration

The two dominant timing-related effects are the time offset and the time-walk effect. The time offset is concerned with the synchronisation difference between the channels. This discrepancy between the time origin can originate from different sources, such as the varying cable lengths and the variation in wavelength-shifting processes. Single muon track data are typically used to measure the offset. The time offset between channels can be observed after removing the muon travel time and the photon propagation time.

The time-walk is mainly caused by the applied electronics threshold, without correcting this effect, the hit time will show a dependency on the hit amplitude, where the large signals being registered earlier than those with smaller amplitudes due to their steeply rising waveform.

4.3.5 Detector Geometry Calibration

The inter-detector and inter-cube alignment are important, so the measurements and corrections on the relative positions and orientations of the detectors with respect to SuperFGD and the cube sag are required. The calibration procedures for these geometric effects are currently under study.

Chapter 5

Particle Activity at the Neutrino Interaction Vertex in the SuperFGD

Presented in this chapter is a private feasibility study, the content of which is not reviewed by the T2K collaboration, hence may not reflect or represent the views or findings of the T2K collaboration and should not be considered as an official T2K result.

At the T2K beam energy, the most common way for neutrinos to interact with the detector is via the charged-current (CC) interaction without outgoing pions (CC0π events). The interaction topology of a ν_μ CC0π event can be written as

$$\nu_\mu + N \rightarrow \mu^- + X, \tag{5.1}$$

where N is the target nucleon, and X is the outgoing hadronic system. In the SuperFGD, such an event can be identified by a long curved track (μ) and a relatively short track (p) originating from the same vertex. An example of a CC0π event candidate is shown in Figure 5.1.

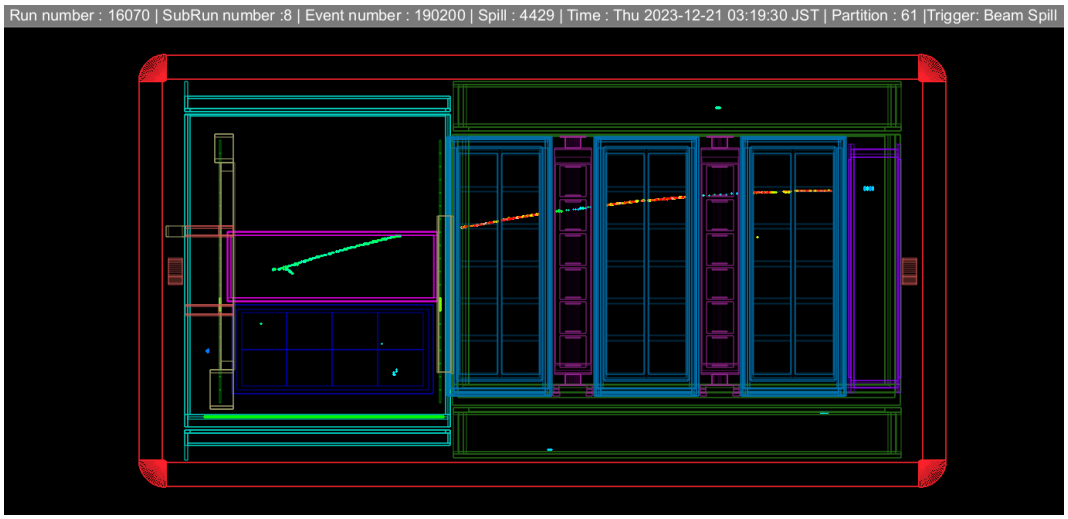


Figure 5.1: A CC0π event candidate inside the ND280. It is likely an event where a muon neutrino (track invisible) entering from the left interacts with the SuperFGD (the magenta box on the left) and produces a long muon track and a shorter proton track.

Apart from the primary products, a neutrino-nucleus interaction can also produce multiple short tracks near the interaction vertex. The energy deposition from such short tracks in proximity to the interaction point is called the vertex activity (VA). A poor understanding of the vertex activity can lead to inaccurate event reconstruction or even misidentification.

Despite the fine granularity of the SuperFGD, the reconstruction of the vertex activity remains inherently challenging. As the short tracks overlap, the number of particles involved cannot be determined with confidence, and due to the short track lengths, traditional track fitting algorithms often perform poorly. Combined with the uncertainties in charge calibration, it is well-motivated to explore modern machine learning (ML) algorithms, such as a Transformer.

5.1 Transformer Neural Network

A deep learning neural network (NN) is a type of computation algorithm that was inspired by the structure and function of the human nervous system. It consists of multiple layers of interconnected 'neurons', which are the fundamental units that store and process data in a hierarchical manner. Each layer applies specific weights and biases to the input data and passes it to the next layer. The backpropagation feature allows the network to learn and identify how the weights and biases need to be modified after each step. A review of the topics related to deep learning can be found in reference [99].

A Transformer NN is an ML algorithm that utilises a neural network architecture designed to handle sequential data that possess complex short- and long-range dependencies. The architecture was first proposed by Google in 2017 [100] and has been widely adopted in various fields of computer vision and natural language processing. Examples such as machine translation and large language models, to name a few, ChatGPT [101] and BERT [102], are some of the most well-known applications of the algorithm.

A Transformer network consists of an encoder and a decoder, and each contains multiple identical layers. The encoder is responsible for transforming an input sequence of 'tokens'[a], $(x_1, x_2, \cdots, x_n)$, into an intermediate differentiable sequence $\mathbf{z} = (z_1, z_2, \cdots, z_n)$ called an 'encoding'[b]. On the other hand, the decoder takes the encoding sequence $\mathbf{z}$ as an input and iteratively generates an output sequence of tokens $(y_1, y_2, \cdots, y_m)$, with each iteration taking the previously generated tokens as additional inputs[c].

Several features of the Transformer NN contribute to its effectiveness:

- token embedding: each token is converted into an embedding, which is a vector that captures the meaning of a token such that the embeddings of the tokens that share similar meanings are close in a vector space. For example, in language processing, the 'husky' vector would be closer to the 'beagle' vector than the 'bagle' vector.

[a] A sequence of tokens can be, for example, a sentence of words, a time sequence of signals, or a sequence of pixels flattened from an image.
[b] An encoding is sometimes called a 'representation'.
[c] The generation process which takes the previous results as additional inputs is said to be 'auto-regressive'.

- positional encoding: the order of the tokens in a sequence is also encoded because the tokens ordered differently may have a different meaning.
- attention: this helps the NN understand which input tokens are significant when generating an output token. A translation task in the paper by Bahdanau et al. [103] highlights the significance of the attention mechanism, where the translation model was able to correctly translate 'European Economic Area' into French 'zone économique européenne' by focusing on the important input words (see Figure 5.2).
- self-attention: contrary to the attention mechanism, the self-attention is the output-to-output and input-to-input attention where the model can learn the dependencies of a token on the surrounding neighbours. In the natural language translation example, the self-attention features help the model understand the context of a word[d].

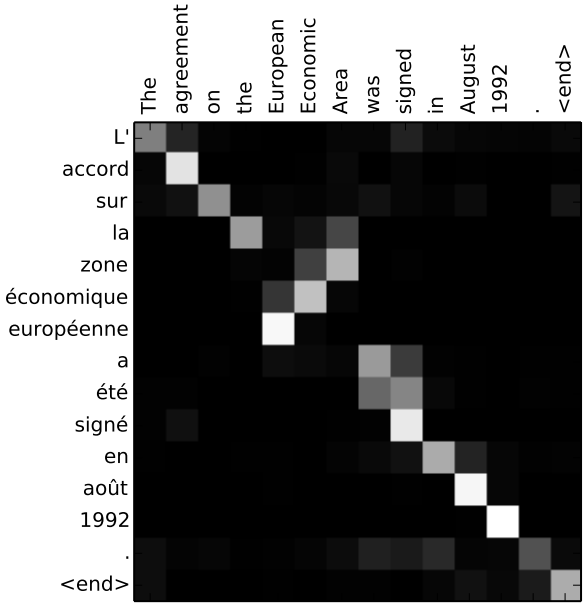


Figure 5.2: An attention heat map shown in [103]. When generating 'zone économique européenne', the language model has its attention non-monotonically on 'European Economic Area', shown by the non-diagonal appearance of the heat map, and is able to correctly identify the word order and gender.

The Transformer architecture holds many advantages over conventional network designs [104, 105, 106], such as Convolutional Neural Networks (CNNs), which are widely used in image analysis tasks, and Recurrent Neural Networks (RNNs) for language processing. Transformers excel at identifying long-range token dependencies, while CNNs struggle to understand correlations outside of the kernels and RNNs also face challenges in keeping distant dependencies due to vanishing gradient issues during training. Transformers are much more context-aware thanks to the attention features. Additionally, CNNs are limited by kernel size, and the sequential processing of RNNs restricts the possibility of a non-monotonic understanding of the input tokens. Moreover, Transformers are able to process the tokens in parallel, which makes them much more efficient and easy to train. CNNs and RNNs, in contrast, are slow to train due to their sequential nature and recurrent design.

[d]For example, a bat can refer to sports equipment or an animal in a different context.

The Transformer is particularly suitable for tackling the VA fitting problem. The possibility for accepting variable-length inputs enables the compression of sparse event images, while the attention features help provide contextual interpretation of the hits. Moreover, the ability to effectively retain long-distance memories is necessary for understanding the 3D-geometrical relationships between hits from the flattened images.

5.2 Vertex Activity Fitting Utilising Transformer Network

The first Transformer NN utilised in VA fitting in a general voxelised 3D detector demonstrated the feasibility of the method [107]. The NN was shown to be effective at reconstructing short proton tracks produced in CC0π events. In this section, we will start by summarising the design of the NN used in the paper, and end by presenting an alternative training process the NN trained with which demonstrated good robustness against calibration inaccuracies.

5.2.1 The Transformer Neural Network Design

In the original paper [107], the Transformer NN consists of 10 encoder and 10 decoder layers, and each layer has a total number of 192 neurons. A total of 16 attention heads are employed. All these sum up to a total of 10,393,165 trainable model parameters. At the training stage, the accumulation strategy is used, where the gradients of 4 batches of 512 samples are processed and accumulated, optimising memory usage and parallelism. The optimisation algorithm used is LAMB [108], which combines large batch optimisation, layerwise adaptive (learning) rate scaling ('LARS', [109]), and Adam [110], a well-known stochastic gradient descent (SGD) method.

A classic SGD updates the weights at the t^{th} iteration, w_t, as

$$w_t = w_{t-1} - \alpha g_t, \tag{5.2}$$

where α is a (constant) learning rate and $g_t = \nabla_w \ell_t(w_{t-1})$ is the gradient of the loss function ℓ, which is a metric measuring the performance of the network. In the original study [107], the mean squared error was used, i.e. $\ell_i \sim (x_i - y_i)^2$ for some prediction x_i and label y_i. Adam improves from the classic SGD by introducing the concept of 'momentum'. It works by computing the first and the second moments,

$$m_t = \beta_1 \cdot m_{t-1} + (1 - \beta_1) \cdot g_t \text{ (first moment, the 'mean')}, \tag{5.3}$$

and

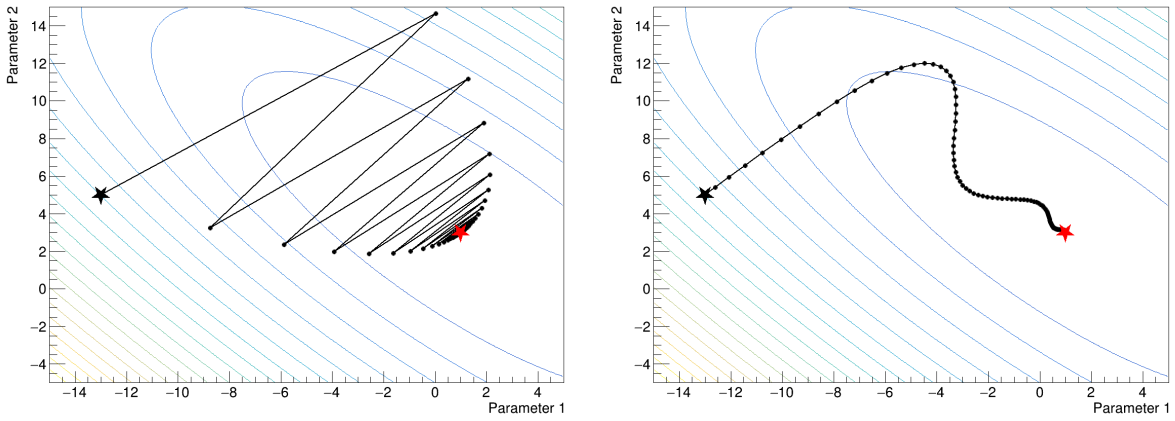
$$v_t = \beta_2 \cdot v_{t-1} + (1 - \beta_2) \cdot g_t^2 \text{ (second moment, the 'momentum')}, \tag{5.4}$$

where two hyperparameters, β_1, β_2 are added, and $g_t^2 \equiv g_t \cdot g_t$. The weights are updated using the formula,

$$w_t = w_{t-1} - \alpha \frac{\hat{m}_t}{\sqrt{\hat{v}_t} + \epsilon}, \tag{5.5}$$

where the mean and the momentum are bias-corrected via $\hat{m}_t = m_t/(1 - \beta_1)$ and $\hat{v}_t = v_t/(1 - \beta_2)$, and a small number ϵ is added to avoid numerical singularity. Qualitatively, the momentum captures the

overall trend of the gradients, which increases the rate of convergence in many situations. A comparison illustrating the effect of Adam can be found in Figure 5.3. In the study, the default values $\beta_1 = 0.9$ and $\beta_2 = 0.999$ were used.



(a) Classic SGD (b) Adam

Figure 5.3: A possible scenario illustrating the improvement of Adam compared to the classic SGD. The two optimisers initially start at the same point in a 2D parameter space (marked with a black star). Each line segment denotes one algorithm iteration. The momentum feature helps the Adam optimiser converge onto the global minimum (marked with a red star) more efficiently.

Motivated by the observation that the ratio of $L2$-norms, $||w_t||_2/||g_t||_2$, can change significantly from one layer to another, the LAMB optimiser scales the learning rate by a factor ϕ that depends on the ratio for each layer. Empirically, this treatment improves many challenging training tasks, as shown in the LAMB paper.

The NN workflow is illustrated in Figure 5.4. It is able to decompose $7 \times 7 \times 7$ VA images, each including a vertex from which one muon track and one to five protons originate. Due to the sparseness, the images are pre-processed into lists of non-empty pixels containing the hit coordinates and the energy deposition ($N_{\text{p.e.}}$). It is assumed that the muon track is reconstructed from some other means, for example, methods based on track length and track curvature, so the reconstructed kinematic parameters for the muon track are also included as input. The encoder transforms the input into embeddings and passes the embeddings to the decoder, which is designed to decompose the embeddings iteratively in descending order according to the reconstructed kinetic energies (KEs) of the short proton tracks. By doing so, it is more transparent for a human to interpret the fitting mechanism. Starting from the proton track with the highest kinetic energy, the decoder outputs the kinetic energy, track direction, as well as a boolean value indicating whether the decoder thinks there are more proton tracks. The decoder also predicts the vertex position in the process.

A Generative Adversarial Network (GAN) [111] is incorporated into the training workflow. This generative model utilises the reconstructed kinematic variables from the decoder to generate particle tracks, which are then combined to form a replica of the original input VA image. By comparing this replica to the original, the decomposition result can be evaluated. Furthermore, based on the evaluation,

the algorithm performs an additional optimisation on the kinematic parameters by minimising the loss function.

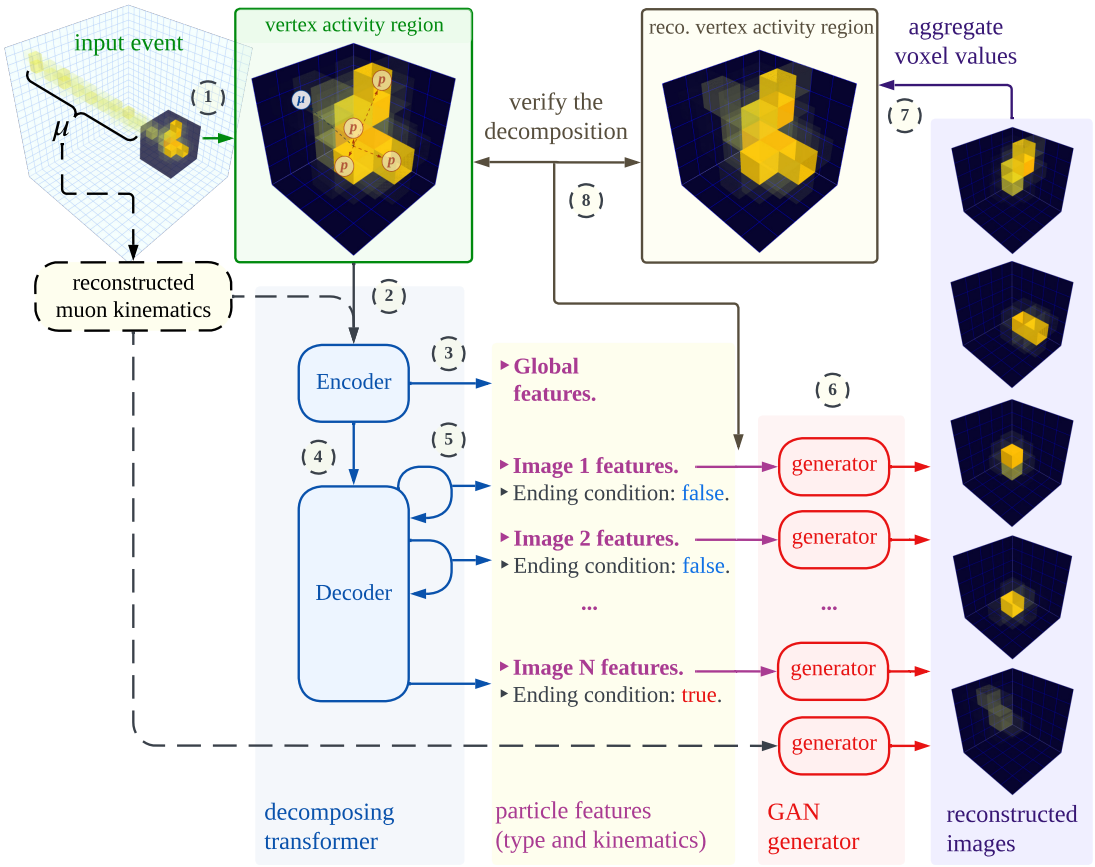


Figure 5.4: The workflow of the vertex activity neural network [107]. The neural network takes VA images as input and predicts the vertex positions and proton kinematic variables iteratively.

The original result shows that the Transformer network is able to identify the number of proton tracks correctly at an accuracy of $\sim 70\%$, and is able to reconstruct proton tracks with kinetic energies under 60 MeV, which were previously not reconstructed by the SuperFGD using traditional fitting methods (see Figure 5.5). The direction and position reconstruction accuracy is also impressive, achieving a sub-centimetre level.

5.2.2 A New Training Process

The work presented in this chapter is built on top of the original study described above. Compared to the original study, two new features are added. The dataset preparation method was inherited from the original paper [107], but the proton track simulation used for training was done in the ND280 software suite. Also, two random scaling effects were added to decrease calibration dependency and overfitting.

A CC0π VA event is contained within a $7 \times 7 \times 7$ SuperFGD cube region, where the centre has the coordinate $(0, 0, 0)$. At run-time, each event is generated by randomly assembling one muon track and one to five proton tracks that originate from the same 'sub-voxel', where a sub-voxel is a $0.2 \times 0.2 \times 0.2$ mm^3

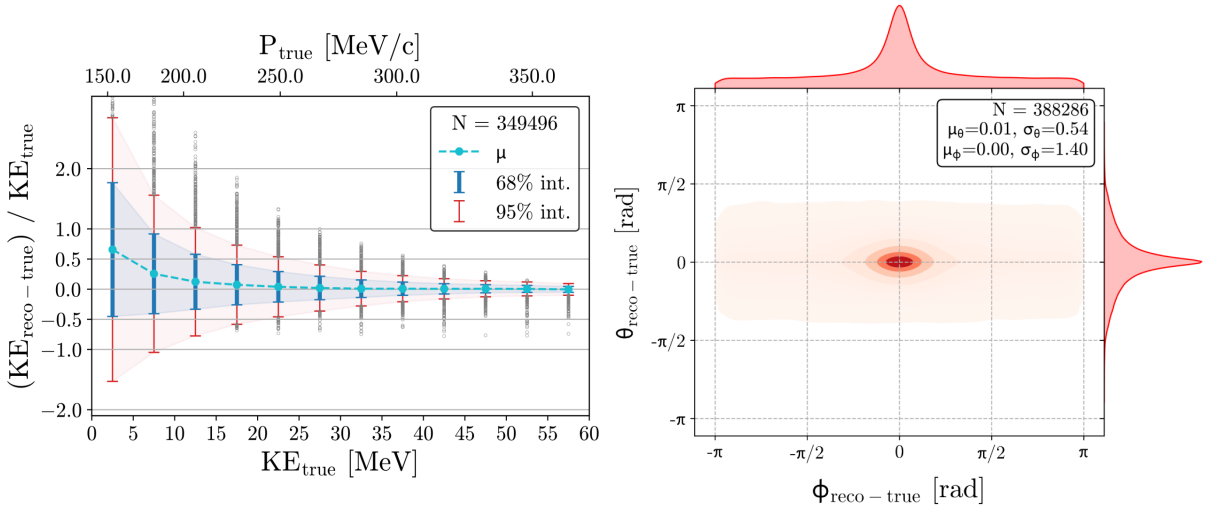


Figure 5.5: Short proton track kinetic energy (left) and directional reconstruction (right) accuracy of the Transformer neural network [107]. The results show that the Transformer network performs well in reconstructing proton tracks that are difficult to do with other conventional methods.

volume formed via equally subdividing a cube into $50 \times 50 \times 50$ sub-cubes. In each training run, five million proton tracks and five million muon tracks were generated, so on average, each sub-voxel contains 40 proton tracks and 40 muon tracks that can be selected from, dramatically increasing the variety of events in the dataset. Subsequently, after the assembly, this event has a chance to be shifted randomly by ± 1 cube length in each direction, so the final event vertex can reside anywhere within the central $3 \times 3 \times 3$ cube region. This is to account for realistic reconstruction errors. Finally, the image is processed into a list of non-empty pixels storing the hit coordinates and numbers of photoelectrons.

The proton tracks were generated using the Monte Carlo (MC) simulation tools within the ND280 software suite (version 14.21), but the muon dataset was taken from the original study. The simulated protons had kinetic energies distributed uniformly from 5 MeV to 60 MeV, while the muons had kinetic energies ranging from 300 to 1000 MeV. The vertices of the tracks were evenly spread across the central cube volume, with initial momentum vectors pointing in all directions. The proton simulation followed the steps:

Step 1: ND280 GEANT4 simulation: simulates the proton interactions within the SuperFGD volume using a GEANT4-based [112] package

Step 2: Detector response simulation: simulates the detector electronics response to the proton hits

Step 3: Calibration: corrects and converts the electronic signals into $N_{\text{p.e.}}$

Two modes of running are included in the ND280 software suite, as shown in Figure 5.6, where either the 'real data' (MIDAS[e] files) or the 'MC simulation' of neutrino interactions is processed into files suitable for purposes such as neutrino oscillation analysis. In the current SuperFGD MC simulation, the

[e]MIDAS is an abbreviation of 'Maximum Integrated Data Acquisition System', a common data acquisition package used in experimental particle physics.

number of photons produced per energy deposited tuned to 320 p.e./MeV, and after all corrections, the energy deposition per track length is set to 20.7 p.e./mm for a minimum ionising particle (MIP). The Birks' quenching factor is 0.0208 cm/MeV.

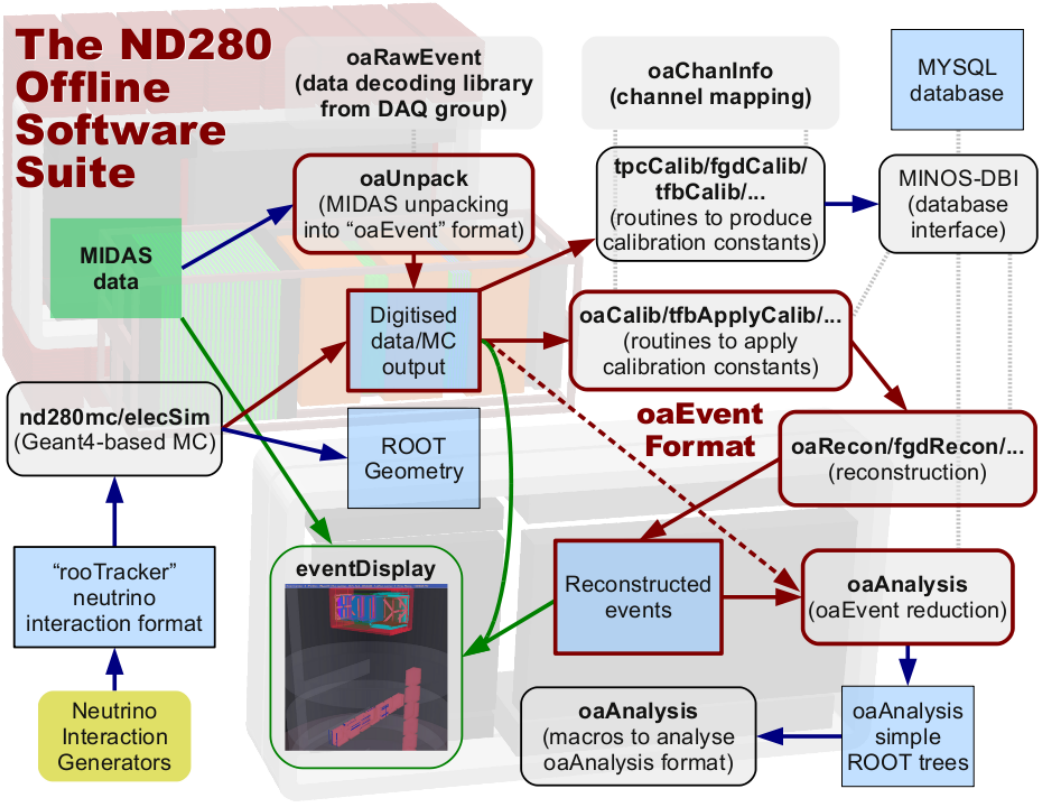


Figure 5.6: A schematic diagram [113] showing the process chain of the ND280 software suite. Two main purposes of the suite are to process *Data* (starting from the MIDAS data) and to generate *Monte Carlo events* (starting from 'Neutrino Interaction Generators'), the output of which is compared and studied.

In total, two datasets, each containing five million proton tracks, were created. One of the two datasets was introduced additional noises, in order to emulate calibration defects. A similar treatment to the dataset was employed by NOνA during the training of a CNN [114, 115].

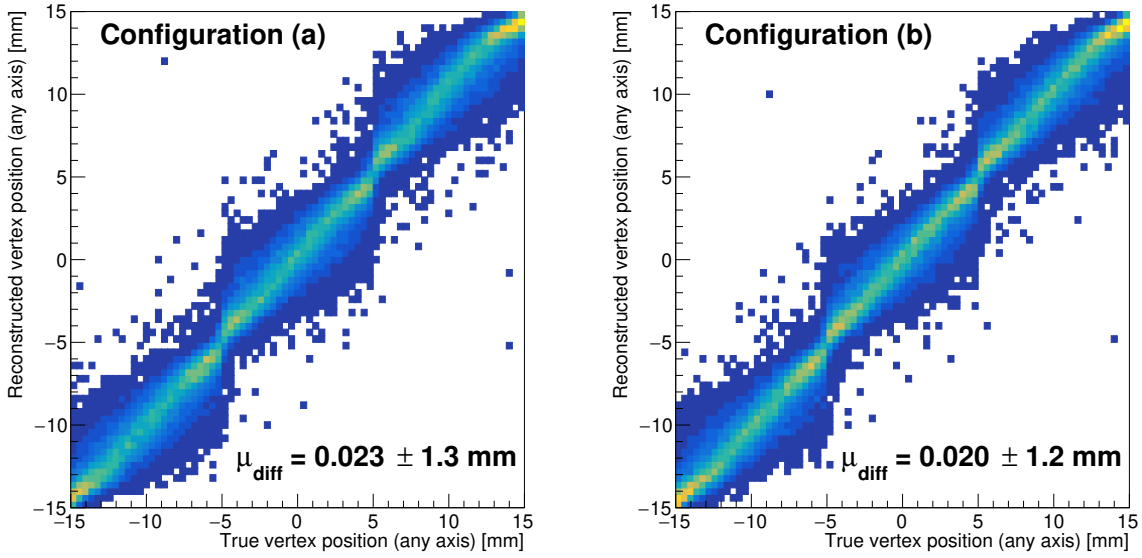
The calibration noise was introduced to the dataset according to the following procesure. Each hit (energy deposition) i of a proton track was multiplied by a random scaling factor $(1 + \epsilon_{\text{abs}})$, where the absolute energy scale ϵ_{abs} is a random varible that is shared by all hits of the same event. ϵ_{abs} follows a normal distribution with a mean of 0 and a variance of 0.05, which we denote as $\epsilon_{\text{abs}} \sim \mathcal{N}(0, 0.05)$. Then, each hit of the same event was multiplied by a second scaling factor $(1 + \epsilon_i)$, where the relative energy scale ϵ_i is also a normally distributed random varible, $\epsilon_i \sim \mathcal{N}(0, 0.05)$. The magnitude of the relative energy scaling is applied on a per-hit basis, hence the value may differ from hit to hit. The absolute scaling aimed to capture the effects contributing to the SuperFGD channel-to-channel variation, while the relative scaling represented the measurement resolution of number of photoeletrons per hit, $N_{p.e.}$.

5.3 Results

In this section, the results of the two Transformer models that were trained on different datasets are compared:

- **configuration (a)**: trained on SuperFGD simulation dataset;
- **configuration (b)**: trained on SuperFGD simulation dataset with the additional noise described in Section 5.2.2.

Both models predicted vertex position accurately, as shown in Figure 5.7. All three orthogonal axes, x, y, z, were accumulated in the histograms. The absolute difference, $x_{\text{reco}} - x_{\text{true}}$, where x can be any of the three axes, was calculated, and the statistics, including the mean, μ_{diff}, and the standard deviation, σ_{diff}, are shown. A slight improvement can be seen between the two, but the difference is small. The plots also demonstrated the ML algorithm can achieve sub-centimetre resolution when it comes to vertex reconstruction, a scale that is smaller than the physical detector pixel.

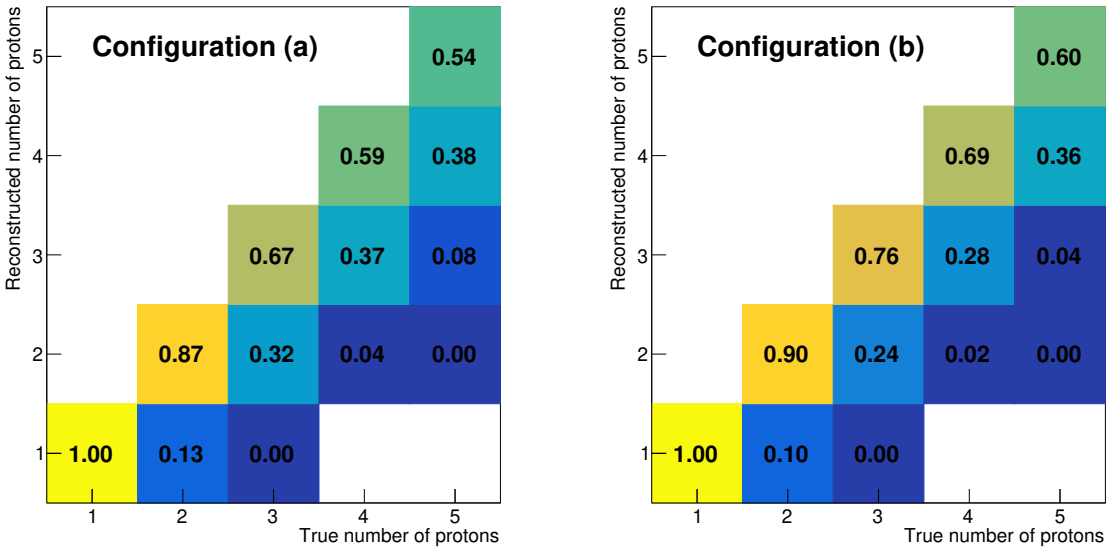


(a) Configuration (a)

(b) Configuration (b)

Figure 5.7: 2D histograms showing the true vs reconstructed vertex positions (in all three orthogonal directions), produced by the two Transformer models. The mean differences between the true and the reconstructed coordinates are included. The apparent boundaries at ±5 mm are caused by the physical separations between cubes.

Figure 5.8 shows the confusion matrices for the number of protons in each event, as predicted by both model configurations. The bins were normalised in each column, where given a true number of protons, the reconstructed numbers summed up to one. Configuration (b) displayed a higher ability to correctly identify the number of protons in each event.



(a) Configuration (a)

(b) Configuration (b)

Figure 5.8: Confusion matrices for reconstructing the number of protons in each event. Configuration (b) has a slightly enhanced ability to determine the number of protons in each event.

Figure 5.9 and Figure 5.10 compare the proton kinetic energy resolutions for single-proton events and those with any number of protons respectively. The upper panel in each plot shows the fractional error, defined as,

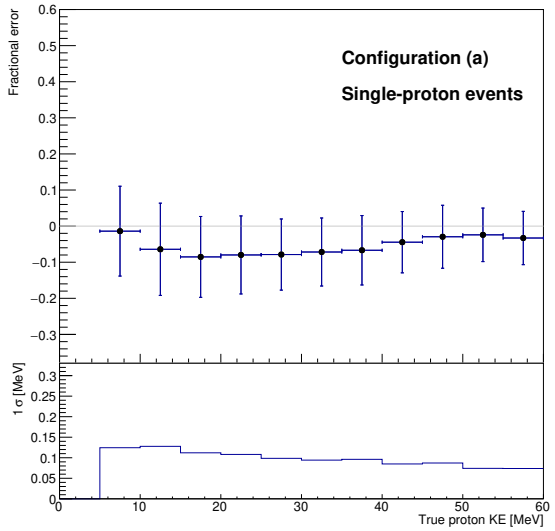
$$\frac{\mathrm{KE}_{\mathrm{reco}} - \mathrm{KE}_{\mathrm{true}}}{\mathrm{KE}_{\mathrm{true}}},$$

as a function of true proton KE, and the error bars are the $\pm 1\sigma$ intervals, which are separately shown in the lower panel. The difference between the two figures, especially in the low energy regions, showed that the reconstruction of short proton tracks in multi-proton events remained difficult, while within each figure, the use of the noisy dataset in training improved the accuracy of the Transformer model. The reconstruction resolution, however, did not see significant improvement. As a reference, a proton with kinetic energy of 30/50/60 keV roughly creates a track of 1/2/3 cube-length(s) inside the SuperFGD [116].

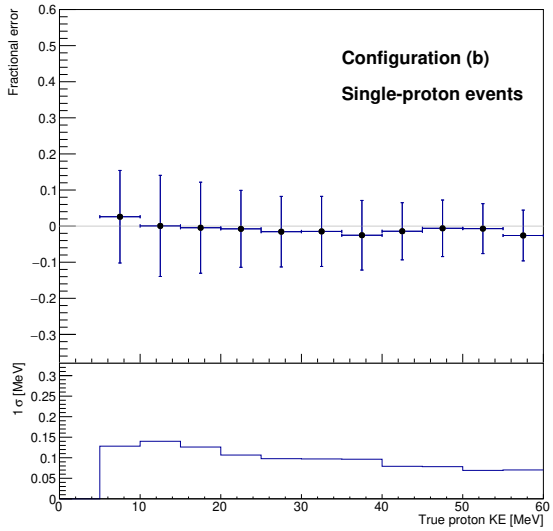
The total proton KE of the events was also studied, the results of which are summarised in the truth vs reconstruction 2D histograms in Figure 5.11. Configuration (b) model had the better accuracy, but the resolution is similar.

Finally, the direction reconstruction performance of the two models can be found in Figure 5.12, where the initial track direction, parameterised by the polar angle θ and the azimuthal angle ϕ, was measured. The means, μ, and the standard deviations, σ, of the absolute angle differences $\phi_{\mathrm{reco}} - \phi_{\mathrm{true}}$ and $\theta_{\mathrm{reco}} - \theta_{\mathrm{true}}$, were also included. Both angles were measured more accurately using configuration (b) model.

In summary, the configuration (b) model, which was trained using the dataset simulated by the

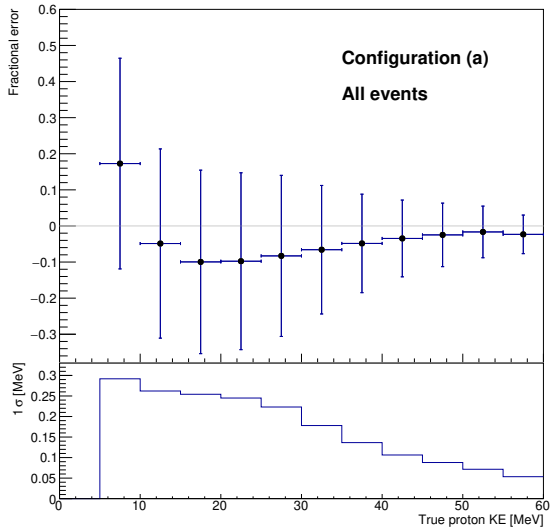


(a) Configuration (a)

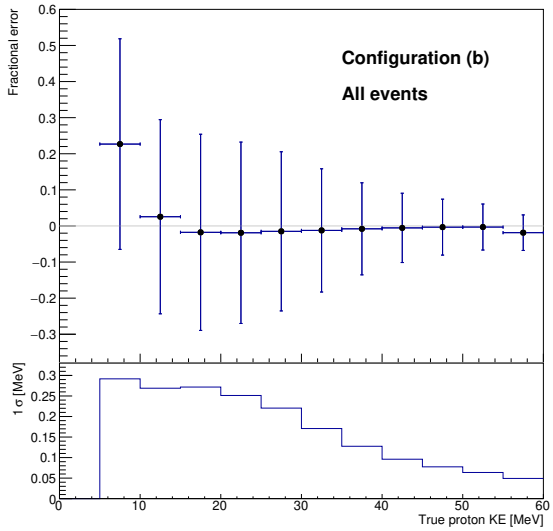


(b) Configuration (b)

Figure 5.9: The comparison of KE fractional errors, defined as $\frac{\mathrm{KE_{reco}}-\mathrm{KE_{true}}}{\mathrm{KE_{true}}}$, achieved by the two different Transformer models. Only events with truly one proton were included. Configuration (b) produced more accurate results. The error bars represent $\pm 1\sigma$ intervals.



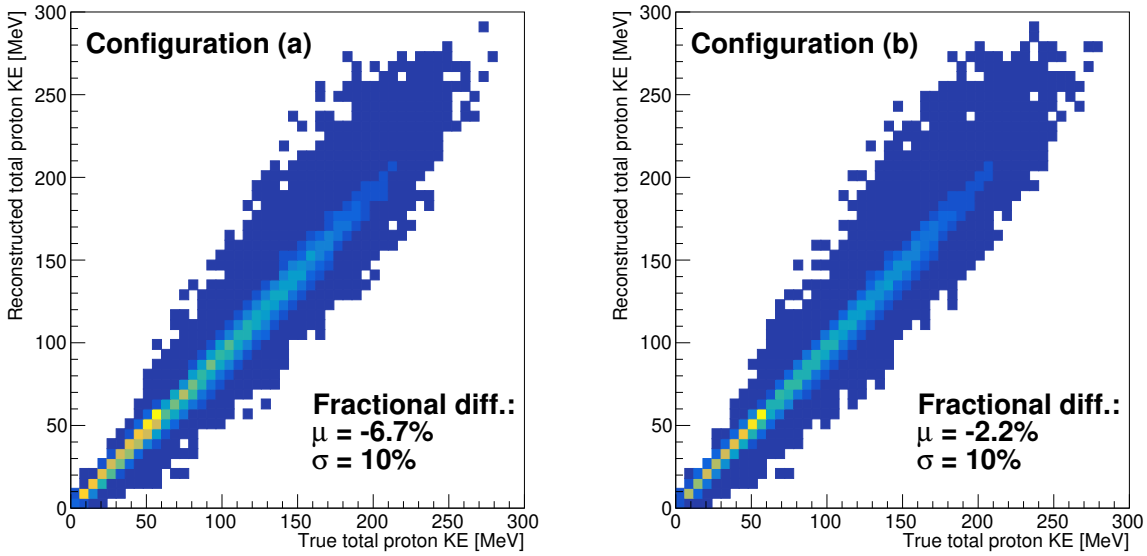
(a) Configuration (a)



(b) Configuration (b)

Figure 5.10: The comparison of KE fractional errors, defined as $\frac{\mathrm{KE_{reco}}-\mathrm{KE_{true}}}{\mathrm{KE_{true}}}$, achieved by the two different Transformer models. All possible numbers of protons per event (1–5) were included. Configuration (b) produced more accurate results. The error bars represent $\pm 1\sigma$ intervals.

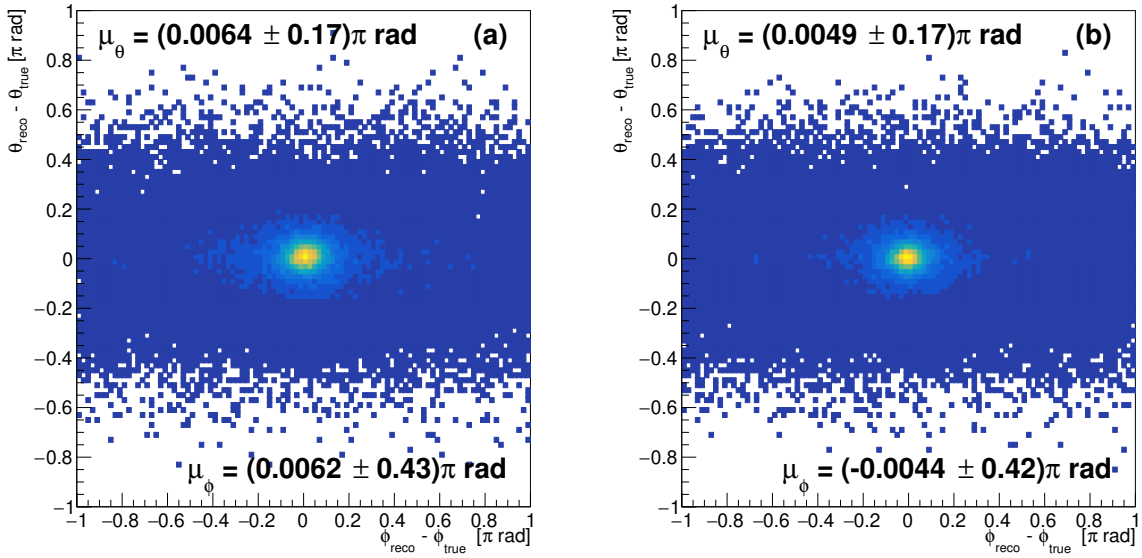
ND280 software suite with additional calibration defects, performed noticeably better in the testing. It consistently produced results that were more accurate compared to the configuration (a) model. However, the models were not tested with real data collected by the SuperFGD; therefore, the results should be interpreted with caution. Nonetheless, this feasibility study has demonstrated promising performance that a deep learning neural network can achieve, and future work is encouraged to fully explore the potential of such a reconstruction method.



(a) Configuration (a)

(b) Configuration (b)

Figure 5.11: 2D histograms of the true vs reconstructed total proton KE for each event



(a) Configuration (a)

(b) Configuration (b)

Figure 5.12: 2D histograms showing true vs reconstructed initial track direction. The mean differences of the angles θ and ϕ are included.

Chapter 6

Neutrino Oscillation Global Study within GAMBIT

Since the theoretical prediction of neutrino oscillation was proposed by Bruno Pontecorvo in 1957, various experiments have been conducted to study the phenomena. Due to the variations in design, including the detection techniques, the neutrino sources and energies, and the baseline, each experiment can be particularly sensitive to a subset of neutrino oscillation parameters. Table 6.1 contains the current dominant and important experiment contributions to the different neutrino oscillation parameters as reported by the Particle Data Group (PDG) [117].

Table 6.1: A table summarising the current sensitivities of the neutrino oscillation experiments [117].

Experiment	Dominant	Important
Solar Experiments	θ_{12}	$\Delta m^2_{21}, \theta_{13}$
Reactor Long-Baseline (KamLAND)	Δm^2_{21}	θ_{12}, θ_{13}
Reactor Medium-Baseline (Daya-Bay, RENO, Double Chooz)	$\theta_{13}, \lvert\Delta m^2_{31,32}\rvert$	–
Atmospheric Experiments (Super-K, IceCube)	–	$\theta_{23}, \lvert\Delta m^2_{31,32}\rvert, \theta_{13}, \delta_{\rm CP}$
Accelerator Long-Baseline ν_μ, $\bar{\nu}_\mu$ Disappearance (K2K, MINOS, T2K, NOνA)	$\lvert\Delta m^2_{31,32}\rvert, \theta_{23}$	–
Accelerator Long-Baseline ν_e, $\bar{\nu}_e$ Appearance (MINOS, T2K, NOνA)	$\delta_{\rm CP}$	θ_{13}, θ_{23}

Given the clear strengths and weaknesses of each neutrino experiment, it is natural to wonder what insights a combined study can reveal. Global fitting is an effective tool for studying neutrino oscillation experimental results in a unified and coherent approach. By combining the results from different experiments which are sensitive to different parts of the neutrino oscillation parameter space, stricter constraints that cannot be achieved by the experiments separately can be set.

For the success of a global fit study, the accuracy of the experiment modelling, the efficiency of the parameter space exploration, and the eventual statistical interpretation are of vital importance.

However, as the field grows in scope and complexity, performing such a combined study presents some difficult and complicated challenges. First, the experiment simulations are highly tailored and specific to the experiment; therefore, it is often the case that the error modellings for these simulations need to be simplified. Alongside the modelling errors, each experiment also introduces several parameters related to the detectors, neutrino sources, and reconstruction methods, increasing the computation cost rapidly. Furthermore, the limited availability of publicly accessible experiment information and data also adds to the difficulty.

In this chapter, we will start with a short summary of the current progress of the Standard Model three-flavour neutrino oscillation global fit studies. This will be followed by an introduction to the Global and Modular Beyond-the-Standard Model Inference Tool (GAMBIT) [8, 9] and the functions and tools it provides that are useful in our study. Furthermore, the progress of the Standard Model three-flavour neutrino oscillation study within GAMBIT, namely the development of the NOνA, MINOS, KamLAND likelihood functions, their validation results, and preliminary global fits, will be described and shown. Finally, we will end the chapter by discussing the importance and benefits of data openness, proposing a list of data essential to global studies and challenges related to data sharing.

6.1 A Brief Review of the Current Neutrino Oscillation Global Fit Studies

For the reasons mentioned above, it is not surprising that there exist several neutrino oscillation global fit studies. In fact, the earliest global study within the hierarchical three-flavour neutrino framework dates back to the 90s by the 'Bari group' [118], tackling the tricky 'solar neutrino problem' and the 'atmospheric neutrino anomaly'. The paper also produced bounds on neutrino masses (reduced form, assuming $m_1^2 = 0$ and $\delta_{\mathrm{CP}} = 0$) and mixing angles within the three-flavour scheme.

The Bari group remains active in the field of neutrino global fit. In the latest paper from the group [47], apart from δ_{CP}, all oscillation parameters are determined with an accuracy of or smaller than 6%. The paper supports the lower octant (LO) solution $\theta_{23} < \pi/4$ at 90% confidence level (C.L.) and NO at the level of 2.5σ.

The 'València group'[a] also publishes global studies on neutrino mass and neutrino oscillations. In their latest update [46], which employed both Bayesian and frequentist approaches, the group found a mild preference for the NO at the level of 2.5σ in agreement with the Bari result. However, the upper octant (UO) ($\theta_{23} > \pi/4$) solution is favoured at $\sim 2.4\sigma$, in contrast to the LO that the Bari result supports.

Another neutrino oscillation result comes from the NuFIT group[b]. Their 2020 paper [45] weakly supports NO at the 1.6σ level or at the 2.7σ level if taking the Super-K atmospheric neutrino data analysis χ^2 map into account. Interestingly, the solution of θ_{23} changes from the UO supported by the 2020 paper to the lower in their latest version 5.3 release in March 2024 [119], where IO is increasingly

[a]The València group website can be found at `https://globalfit.astroparticles.es/`.
[b]The NuFIT group website can be found at `https://www.nu-fit.org/`.

disfavoured at the level of 3.0σ ($\Delta\chi^2_{\mathrm{IO-NO}} = 9.1$).

The latest results of the mentioned three neutrino global fit groups can be found in Tables 6.8 and 6.9. Also in the tables are preliminary global fit results within GAMBIT, and the methods from which the results are produced will be described in depth in the following sections.

6.2 The GAMBIT Package and the `NeutrinoBit` Module

The GAMBIT software was published in 2017 by the GAMBIT collaboration [8]. It is an open-source global fitting software package for studying generic particle and astronomical physics models, designed with an emphasis on modularity and flexibility. The package also comes with a built-in module which provides a number of robust and efficient statistical sampling methods. With all these features, the GAMBIT package allows users to easily implement new BSM models and new experimental datasets. New analyses can also be incorporated thanks to the extensibility and the framework's ability to interface with external software packages, making GAMBIT a valuable resource for conducting global analyses.

Apart from the BSM collider and dark matter studies [120, 121, 122], which were their initial focus, the GAMBIT collaboration also published papers on neutrino physics. The results include the determination of an absolute mass upper bound for the lightest neutrino using robust cosmological and terrestrial data [123], and a global study of the three right-handed neutrinos extension of the Standard Model [124]. Recent GAMBIT development on neutrino physics also includes a Standard Model three-flavour neutrino global fit, which has been in development for a few years. A record of the early progress, including the development of the T2K likelihood functions, can be found in the thesis by W. Shorrock [125]. By the time of writing, several potential BSM neutrino studies have also been suggested, including a non-unitarity fit.

Inside GAMBIT, calculations of theory predictions and experimental likelihoods are performed by a series of 'module functions', which are grouped into 'physics modules' according to relevance, as illustrated in Figure 6.1. Each module function is tagged with its 'capability', the quantity it is able to calculate, and 'dependencies', the required inputs. To implement a new physics model, one needs to define the model parameters and the necessary functions to calculate the physics quantities and implement a set of likelihood functions for the comparisons to experimental data. The functions can depend on other parent models, which may also have their own parameters. The hierarchical structure of the framework simplifies the implementation of new modules, which enables an efficient way to subject a new physics model to the constraints of many experimental results.

The `NeutrinoBit` module is responsible for the neutrino oscillation calculations. Currently, a total of eight neutrino oscillation experiments are included in the `NeutrinoBit` module. The eight experiments and the corresponding reference papers that are included in this project can be found in Table 6.2. Out of the eight, the NOνA, MINOS, and KamLAND likelihood functions will be described in detail in the later sections.

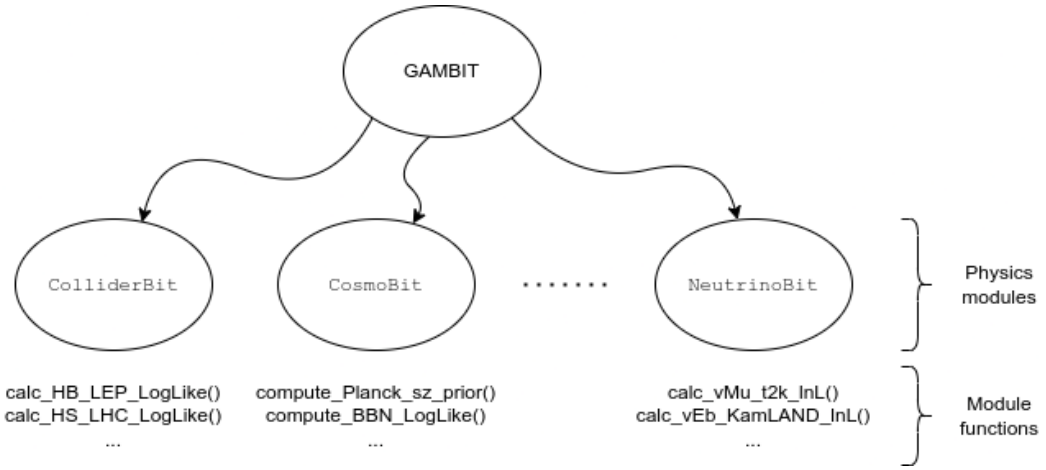


Figure 6.1: The hierarchical structure of the GAMBIT software package

Table 6.2: The neutrino oscillation experiments currently included in `NeutrinoBit` and the associated papers

Type	Experiments
Solar	SNO [126]
Reactor (SBL, LBL)	Daya-Bay [127], KamLAND [128, 129]
Atmospheric	Super-K [130], IceCube [131]
Long-Baseline Accelerator	T2K [61], NOνA [114, 132], MINOS [133]

To run a likelihood scan of a set of parameters, one needs to specify all the necessary parameters, either as fixed values or their respective ranges for GAMBIT to scan over, and the module functions required to carry out the calculation. A wide range of sampling methods and statistical options are also included in the GAMBIT software. These scan specifications are stored as a text file, and because of this, it is simple to switch in and out the modules to produce the desired scan configurations.

6.3 Methodology

Here, we describe how the neutrino oscillation parameter optimisation is performed within GAMBIT.

6.3.1 General Procedure

In a nutshell, to locate the best-fit parameters in a parameter space constrained by a set of experiment observations, the following steps are roughly followed:

Step 1: For each experiment observation, and given a set of parameters, predict the GAMBIT counterpart. In this project, an observation is a neutrino energy spectrum.

Step 2: Compare the GAMBIT prediction to the experimental observation and calculate the likelihood

Step 3: Update the parameter hypothesis according to a sampling algorithm

Step 4: Repeat starting from Step 1 until the convergence condition is met

The exact calculation for each experiment varies and will be described in the following sections separately.

Note that, as important to the values of the best-fit parameters, the region of the parameter space close to the best-fit point should also be sufficiently explored in order to produce accurate constraints.

6.3.2 Likelihood Method

Suppose there is an observed spectrum $\{O_i\}$ and a theoretical spectrum $\{N_i\}$, where O_i and N_i denote the number of events in bin i and $i = 1, \cdots, n$. Given that each observed bin is independent and follows a Poisson distribution whose expected value is predicted by the respective bin in the theoretical spectrum, the likelihood $\mathcal{L}$ associated to this sample is

$$\mathcal{L} = \prod_{i=1}^{n} \frac{N_i^{O_i} e^{-N_i}}{O_i!}, \tag{6.1}$$

and the log-likelihood is

$$\ln(\mathcal{L}) = \sum_{i=1}^{n} O_i \ln(N_i) - N_i - \ln(O_i!). \tag{6.2}$$

The likelihood is maximised if the theoretical prediction matches the observation exactly, ie when $N_i = O_i$ for all possible i. Therefore, the maximal likelihood is given by

$$\mathcal{L}_{\max} = \prod_{i=1}^{n} \frac{O_i^{O_i} e^{-O_i}}{O_i!}. \tag{6.3}$$

The maximum log-likelihood ratio ℓ is calculated following the formula,

$$\ell \equiv \ln(\mathcal{L}/\mathcal{L}_{\max}) = \sum_{i=1}^{n} O_i - N_i - O_i \ln\left(\frac{O_i}{N_i}\right). \tag{6.4}$$

This quantity is chosen over the simple log-likelihood, $\ln(\mathcal{L})$, because it avoids computing log-factorials, and the quantity is easier to interpret, since $\ell = 0$ corresponds to a perfect fit to the observed spectrum. The quantity can also be related to a χ^2 distribution following Wilks' theorem, providing an approximate statistical test.

6.3.3 Scanner

The GAMBIT module `ScannerBit` [134] provides the necessary statistical sampling and scanning algorithms to search for the point of the highest likelihood in the parameter space of a physics model. In this project, unless otherwise mentioned, the `Diver` [134] sampler is used. In this section, we will only briefly describe the algorithm, and for a detailed explanation, refer to the original `ScannerBit` reference.

`Diver` is a sampler performing a self-adaptive λjDE optimisation, a variant of the differential evolution (DE) algorithm [135, 136]. The class of algorithms are known for their robustness in operating in high-dimensional spaces, and because of this, they are well-suited for exploring the vast and complex parameter space of many physics models.

The three main steps common to all DE algorithms are mutation, crossover, and selection. Here, we describe the original DE proposed by Storn and Price in 1995 [135]. The algorithm is controlled by three hyperparameters: the parent population size NP, the learning rate β, and the crossover rate CR. The choice of the hyperparameters is essential to the effectiveness of a scan. Too small of a learning rate or crossover rate, although providing a finer search, leads to a slow convergence speed.

The optimisation starts with an initial population of NP parents $\{\mathbf{x}_1, \mathbf{x}_2, \cdots, \mathbf{x}_{NP}\}$, where each $\mathbf{x}_i$ is a vector of parameters relevant to the concerned physics model that are randomly selected from the allowed parameter space. NP should be large enough so that the whole parameter space is sufficiently covered.

Mutation In the mutation step, a *donor vector* $\mathbf{u}_i$ is generated for each parent $\mathbf{x}_i$ where $i = 1, 2, \cdots, NP$. For each parent $\mathbf{x}_i$, three other members of the parent set, $\mathbf{x}_{i1}, \mathbf{x}_{i2}, \mathbf{x}_{i3}$, are uniformly and randomly selected (the *target vectors*), and the donor vector $\mathbf{u}_i$ is then computed using the equation,

$$\mathbf{u}_i = \mathbf{x}_{i1} + \beta(\mathbf{x}_{i2} - \mathbf{x}_{i3}), \tag{6.5}$$

where β is the learning rate between 0 and 1. In the equation, $\mathbf{x}_{i1}$ undergoes mutation by adding to it a scaled difference vector. It is, therefore, evident that the value of NP is crucial to the algorithm since it directly impacts the density of parents and, consequently, the distance between the target vectors. A large NP will sample the parameter space finely but, as a result, decrease the exploration speed.

Crossover Based on the crossover rate CR ($0 < CR < 1$), which dictates the degree of influence of the donor vectors, the crossover step produces a set of *offspring vectors* $\{\mathbf{x}'_1, \mathbf{x}'_2, \cdots, \mathbf{x}'_{NP}\}$. This crossover is performed element-wise, per parent, according to the formula

$$x'_{ij} = \begin{cases} u_{ij} & \text{if } r \leq CR \\ x_{ij} & \text{if } r > CR \end{cases}, \tag{6.6}$$

where the subscript j denotes the j^{th} element of a vector and r is a random number between 0 and 1. With a high CR, an offspring vector will inherit more mutated elements from the donor and vice versa. A high CR also implies that the algorithm will have a wide exploration of the parameter space.

Selection In the selection step, each parent $\mathbf{x}_i$ and the offspring $\mathbf{x}'_i$ will compete to survive and become a member of the next generation based on some predefined criteria. In our case, the point with the higher likelihood is chosen.

A complete cycle of the three steps produces a new generation of parents, and the process is repeated until some convergence conditions are met. In this study, the j^{th} generation reaches convergence when the 'smoothed fractional improvement' in the population over successive n generations (including the j^{th}) [134],

$$\delta_{\text{smooth}} \equiv \frac{1}{n} \sum_{i=j-n+1}^{j} \left[1 - \frac{\sum_{\text{population}} \ln(\mathcal{L}_{i-1})}{\sum_{\text{population}} \ln(\mathcal{L}_i)} \right], \tag{6.7}$$

drops below a threshold of 10^{-12}. $n = 10$ was set in the study.

The aforementioned DE algorithm is denoted 'DE/rand/1/bin', where

- the first parameter specifies the algorithm type,
- the second specifies how the mutated vector $\mathbf{x}_{i1}$ in Equation (6.5) is chosen,
- the third specifies the number of difference vectors that are included in the mutation,
- and the fourth specifies how the crossover is decided ('bin' for binary).

`Diver` utilises a variant of the original DE algorithm called a self-adaptive λjDE algorithm 'DE/rand-to-best/1/bin', which evolves the algorithm parameters at run time, aiming to optimise the exploration and convergence time. Compared to the original DE (Equation (6.5)), the `Diver` algorithm takes the current best-fit vector into account when computing the donor using the equation,

$$\mathbf{u}_i = \lambda \mathbf{x}_{\text{best}} + (1 - \lambda)\mathbf{x}_{i1} + \beta(\mathbf{x}_{i2} - \mathbf{x}_{i3}), \tag{6.8}$$

where λ controls how influential the current best-fit point $\mathbf{x}_{\text{best}}$ is.

6.4 The NOνA Likelihood Functions in GAMBIT

Similar to the T2K experiment, the US-based 'NuMI[c] Off-axis ν_e Appearance (NOνA) experiment' is also a long-baseline accelerator neutrino oscillation experiment that utilises a near-far detector setup [137, 138]. The two NOνA detectors, the Far Detector (FD) and the Near Detector (ND), are functionally identical, but they are distinct in their sizes. Images of the FD and the ND can be found in Figure 6.2. The FD has a weight of 14 kt, which is approximately 47 times heavier than the ND, which weighs in at 300 t. Both detectors are made up of criss-crossing planes of long rectangular PVC cells containing the liquid scintillator (LS), perpendicular to the incoming beam. The scintillator lights are read out by the wavelength-shifting fibres, the measurements from which can be used to reconstruct particle tracks.

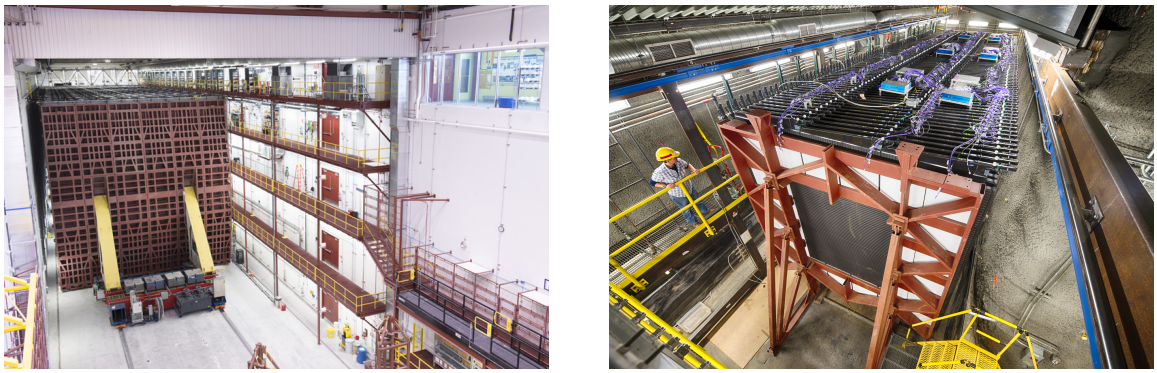


Figure 6.2: The NOνA Far Detector (left [139]) and Near Detector (right [140]). The two liquid scintillator detectors are separated by a distance of 810 km.

[c]NuMI stands for the 'Neutrinos at the Main Injector', which is a neutrino beam at Fermilab.

The NOνA detectors are separated by a distance of 810 km and are located at 14 mrad off-axis away from the NuMI beamline, with the ND located at Fermilab $\sim$ 1 km away from the neutrino source and the FD in Ash River, Minnesota. Consequently, this setup produces a narrow neutrino energy spectrum that reaches its maximum flux at $E_\nu = 2$ GeV, as shown in Figure 6.3, roughly coinciding with the maximal neutrino disappearance.

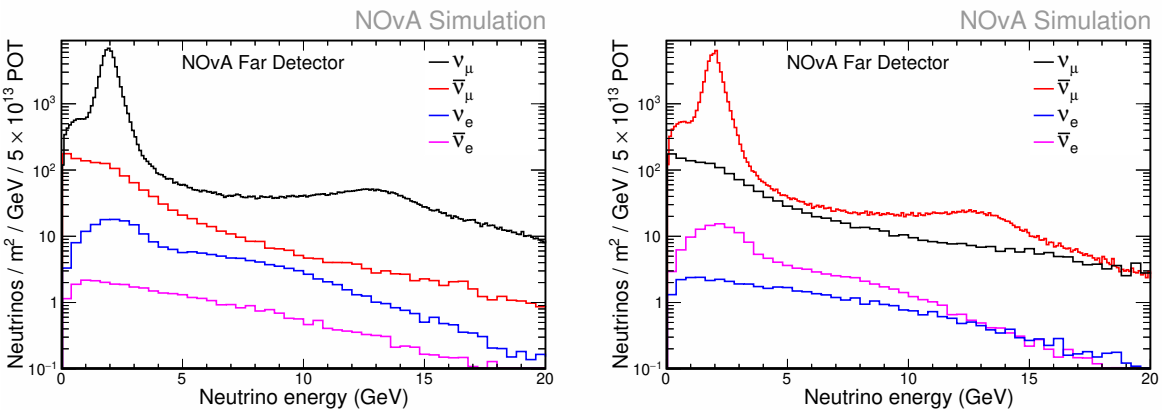


Figure 6.3: The NOνA FD neutrino flux predictions for the Forward Horn Current (left) and Reverse Horn Current (right) modes [141].

For the NOνA beam energy and baseline, the neutrino oscillation probabilities can be approximated using the same equations for T2K (Equations (3.2) and (3.4)). Note that when calculating the oscillation probability in GAMBIT, the full oscillation probability formalism was used, instead of the approximated expressions.

The NOνA experiment measures the neutrino oscillation parameters by comparing the neutrino energy spectrum predictions to the observations at the FD. To generate an FD energy spectrum prediction for a specific sample, NOνA transforms the ND data using a Near-to-Far extrapolation method constrained by external data such as the detector model, neutrino flux, and neutrino interaction model. The neutrino oscillation parameters can then be inferred from fitting the extrapolated FD spectrum to the experimental data.

As opposed to the T2K experiment [142], NOνA does not simultaneously fit the ND and the FD data, and hence, the oscillation fit is not directly constrained by the high-statistics ND data. However, since both the ND and the FD are functionally of the same type, NOνA's oscillation fitting method significantly reduces the uncertainties on neutrino flux and neutrino cross-sections.

The publicly accessible NOνA data is limited. Ingredients such as Near-to-Far ratios are unavailable, making the ND-to-FD propagation in GAMBIT an impossibility. As a consequence, the FD neutrino energy spectra are predicted directly from the truth energy spectra (without oscillation) produced by NOνA (Figure 6.3) scaled by POT. In (anti)neutrino mode, the beam flux consists of 93% (92%) ν_μ ($\bar{\nu}_\mu$) between 1 and 5 GeV.

In GAMBIT, there are four NOνA likelihood functions [d]; each respectively corresponds to one of the $\nu_\mu(\bar{\nu}_\mu) \to \nu_\mu(\bar{\nu}_\mu)$ 'disappearance channels' or the $\nu_\mu(\bar{\nu}_\mu) \to \nu_e(\bar{\nu}_e)$ 'appearance channels'. There is an additional function for constraining the nuisance parameters [e]. The current NOνA likelihood functions utilise the NOνA '2020' results [114] that include the data of 13.6×10^{20} protons-on-target (POT) in neutrino mode and 12.5×10^{20} POT in antineutrino mode. All channels, including the peripheral samples, are considered.

In the likelihood functions, the energy spectra are predicted using Equation (6.9), a method modified from that proposed in [143]. For an oscillation channel $\nu_\beta \to \nu_\alpha$, and for a specific neutrino-nuclear interaction channel ch, the expected number of ν_α events in bin i of the energy spectrum is given by

$$N_i^{ch,\beta,\alpha} = \int_{E_i}^{E_{i+1}} \mathrm{d}E_{\mathrm{rec}} \int_0^\infty R_{ch,\alpha}\left(E_{\mathrm{rec}}|E_\nu\right) \frac{\mathrm{d}\Phi_\beta}{\mathrm{d}E_\nu} \sigma_{ch,\alpha}\left(E_\nu\right) \epsilon_{ch,\alpha}\left(E_\nu\right) P_{\nu_\beta \to \nu_\alpha}\left(E_\nu\right) \mathrm{d}E_\nu, \tag{6.9}$$

where E_i and E_{i+1} are the left and right bin limits, E_{rec} and E_ν are the reconstructed and true energies of neutrino ν_α, $R_{ch,\alpha}$ is the reconstruction function for interaction channel ch and neutrino ν_α, Φ_β is the flux of ν_β at the FD without oscillation, $\sigma_{ch,\alpha}$ is the cross-section for interaction channel ch of neutrino ν_α, $\epsilon_{ch,\alpha}$ is the selection efficiency, and $P_{\nu_\beta \to \nu_\alpha}$ is the oscillation probability. So, the total predicted number of events in bin i is

$$N_i^\alpha = N_i^{\mathrm{bkg}} + \sum_{ch,\beta} N_i^{ch,\beta,\alpha}, \tag{6.10}$$

where N_i^{bkg} is the number of expected background events in bin i, and the sum runs over all interaction channels ch and source neutrino types β. The background spectra are difficult to predict with our GAMBIT calculation since they are strongly influenced by the experiment designs and background modelling. Therefore, the likelihood calculation uses the values estimated by the NOνA experiment directly.

The NOνA experiment uses different methods depending on the neutrino flavour to reconstruct neutrino energy, E_ν. For ν_μ charged-current (CC) candidates, the reconstructed neutrino energy, given by Equation (6.11), is the sum of the muon energy E_μ (measured based on the track length) and the total energy of the hadronic products E_{had},

$$E_{\nu_\mu} = E_\mu + E_{\mathrm{had}}. \tag{6.11}$$

As for the ν_e CC candidates, on top of the electromagnetic (EM) shower energy E_{EM} and the hadronic energy E_{had}, a second-order term is introduced for each component, as shown in Equation (6.12),

$$E_{\nu_e} = c_{\mathrm{EM},1} E_{\mathrm{EM}} + c_{\mathrm{had},1} E_{\mathrm{had}} + c_{\mathrm{EM},2} E_{\mathrm{EM}}^2 + c_{\mathrm{had},2} E_{\mathrm{had}}^2, \tag{6.12}$$

where the c coefficients are determined from simulation.

The GAMBIT representations cannot reconstruct neutrino energies following the above methods. This is caused by the limited information about the hadronic and the extensive use of large-scale machine

[d] In GAMBIT, a likelihood function is responsible for predicting an experiment outcome for a given set of parameters and calculating the likelihood by comparing the GAMBIT prediction to the experimental observation.

[e] A nuisance parameter is a parameter that has an impact on the final neutrino spectrum prediction but is not one of the six oscillation parameters. An example could be the neutrino flux normalisation.

learning techniques such as boosted decision trees (BDT) and convolutional neural networks (CNN). Instead, GAMBIT works with binned data, and the predictions are generated directly starting from the neutrino fluxes.

6.4.1 Reconstruction Functions

A reconstruction function represents the reconstruction effects, for instance, of those originating from the finite detector hardware energy resolution. In some experiments, migration matrices are usually generated from simulation to quantify the energy smearing. Each element e_{ij} of the migration matrix indicates what fraction of events in true energy bin i end up in reconstructed energy bin j, and if there is no smearing, the migration matrix will be equivalent to an identity matrix $\mathrm{diag}(1, \cdots, 1)$, assuming the true and reconstructed bin numbers are equal.

There is no release of migration matrices for the NOνA experiment, so a smearing function is assigned to each interaction channel. The smearing functions are chosen to be Gaussian [f] (area-normalised to 1) characterised by two parameters, a reconstruction width σ_{rec} (shared between each neutrino type) and an energy offset from the true energy Δ_{rec} (per interaction channel), collectively called the 'reconstruction parameters' (see Equation (6.13)).

$$R_{ch,\alpha}(E_{\mathrm{rec}}|E_\nu) \equiv \frac{1}{\sigma_{\mathrm{rec},\alpha}\sqrt{2\pi}} \exp\left\{-\frac{1}{2}\left(\frac{E_{\mathrm{rec}} - (E_\nu + \Delta_{\mathrm{rec},ch,\alpha})}{\sigma_{\mathrm{rec},\alpha}}\right)^2\right\} \tag{6.13}$$

Apart from the σ_{rec}, which are related to the constant NOνA nominal resolution values [g] as $\sigma_{\mathrm{rec}} = \sigma_{\mathrm{nominal}} E_\nu$, the central values of the reconstruction parameters are obtained from χ^2 fits to the respective predicted energy spectra by NOνA while fixing the oscillation parameters to the NOνA best-fit values.

6.4.2 Efficiency Functions

The efficiency functions for different neutrino species at the FD were sourced directly from the NOνA collaboration. Each bin represents the fraction of events of a given neutrino type that are selected, defined by

$$\epsilon_i = \frac{(\text{Selected true } \nu_\mu \text{ or } \nu_e \text{ CC events})_i}{(\text{All true } \nu_\mu \text{ or } \nu_e \text{ CC events})_i}, \tag{6.14}$$

where the value is for the entire 14 kt FD, meaning that the denominator does not account for the true fiducial volume.

The selection efficiency plots for the remaining samples can be found in Appendix A.1.

[f] Other functions, such as a log-normal distribution, were tested but were found to have little difference from a Gaussian distribution.

[g] These can be found in the NOνA main reference. Note that the combined resolutions are used for all neutrino samples.

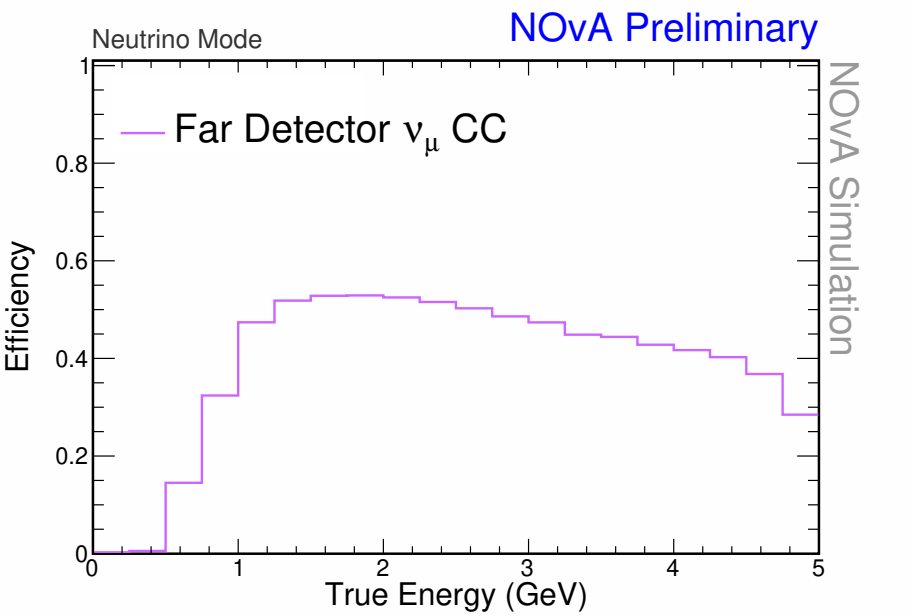


Figure 6.4: The ν_μ selection efficiency at the NOνA FD

6.4.3 Neutrino Interaction and Cross-sections

The NOνA experiment simulates neutrino interactions using a custom configuration of GENIE version 3.0.6 [144, 145]. The modification [h] includes different choices of interaction models for the charged-current quasi-elastic (CCQE), CC two-nucleon two-hole (2p2h [i]), baryon resonance (RES), and deep inelastic scattering (DIS) interactions. The default neutrino coherent scattering (COH) [j] is kept unchanged.

The NOνA MEC model is a variation based on the Empirical MEC model in GENIE. The NOνA modification tunes the original model in a 2D space of $(q_0, |\mathbf{q}|)$, the energy and momentum magnitude transferred from the neutrino to the target [k], to account for the difference between simulation and the ND data after all adjustments to the other interaction channels are made.

Final state interactions (FSI) are also simulated in NOνA. Similar to the 2p2h, NOνA's FSI model is adjusted in a data-driven approach to fit the NOνA interaction models. The detailed treatment is described in the main NOνA paper and the paper [146] dedicated to the tuning of NOνA neutrino interaction models.

In GAMBIT, the NOνA likelihood functions consider five interaction channels, CCQE, RES, MEC, DIS, and COH, which sum up to the total neutrino energy spectrum for a given species. For all apart from the MEC channels, the NOνA cross-section splines are directly used. FSI are not considered.

[h] NOνA use the N18_10j_02_11a tune in the study. The cross-section spline files are published at `https://scisoft.fnal.gov/scisoft/packages/genie_xsec/v3_00_06/`.

[i] Sometimes called the 'meson exchange current, MEC', an interaction between a neutrino and a short-range correlated nucleon pair. They are used interchangeably in this work.

[j] COH is a rare process where a neutrino scatters off from the whole nucleus.

[k] q_0 experimentally is measured as E_{had} while $|\mathbf{q}|$ is reconstructed from the quantity $\sqrt{Q^2 + E_{\text{had}}^2}$ where $Q^2 = 2E_\nu(E_\mu - p_\mu \cos\theta_\mu)) - m_\mu^2$ is the four-momentum transfer.

Unlike the NOνA method, the MEC reweight in GAMBIT is only one-dimensional since it is difficult to decouple the hadronic and leptonic components in Equations (6.11) and (6.12) without the necessary information. Within GAMBIT, the reweight process introduces a scaling factor to each MEC energy bin. These weights are per-bin and are obtained from fits to NOνA best-fit MEC spectra. In addition, we require that the weights must be greater than one to reproduce the enhancement effect.

6.4.4 Neutrino Oscillation Probability Calculations

Neutrino oscillation probabilities are calculated using the Prob3++ package [147]. The open-source software uses the methods based on [148], which calculates the probabilities analytically and includes matter effects[1] during neutrino propagation through the Earth. Unless it is specifically mentioned, this package is used in other likelihood functions for the neutrino oscillation probability calculations.

6.4.5 ν_μ and ν_e samples

Several modern machine learning algorithms are used throughout the NOνA reconstruction chain to achieve high sensitivity. After a data quality cut and a containment check, all event candidates are separated into ν_μ CC, ν_e CC, neutral current (NC), or cosmogenic background using a CNN labelled 'CNN_{evt}'. An additional CNN, in parallel to BDTs also for cosmic background recognition, are used to further reject the FD cosmogenic background events, reducing the contamination to less than 5%. The results of these algorithms are combined to select ν_μ CC and ν_e CC samples of high purity.

For the ν_e samples, further treatments are applied to enhance the sensitivity of the oscillation fit. These fully contained events, named the 'core' events, are further divided into two purity sub-samples based on the CNN_{evt} score. On top of this, some events are selected from those that fail the cosmic rejection or containment check but score highly at the CNN_{evt} and BDT stage to form the 'peripheral' sample. This helps increase the FD selection efficiency.

There is no precise treatment to emulate the NOνA peripheral sample within GAMBIT. Instead, an energy-independent fraction, r_{peri}, of events from each bin is migrated to the pretended peripheral bin. The fraction is calculated from the NOνA best-fit simulation using the formula,

$$r_{\text{peri}} = \frac{N_{\text{peri}}}{N_{\text{core}} + N_{\text{peri}}}, \tag{6.15}$$

where N_{peri} is the total number of peripheral events, and N_{core} is the total number of core events.

For the ν_μ candidates, the sample is further divided into four equal subsets based on the hadronic energy fraction, $E_{\text{frac}} = E_{\text{had}}/E_\nu$. Based on the subsets, binning E_ν in different bin sizes can further increase the sensitivity to the oscillation parameters since the hadronic energy fraction is correlated to the energy resolution and the fraction of background contamination.

[1]The Earth density for NOνA is 2.84 g/cm^3 and is approximately constant during neutrinos' traverse through the Earth.

Attempts were made to model the sample-dependent energy resolution for the ν_μ samples within GAMBIT, but the effects were found to be marginal and, in some configurations, could even cause over-fitting. It is therefore decided to leave out the procedure in the production runs.

After obtaining the energy spectrum, the NOνA likelihood is calculated by summing the likelihood ratio (Equation (6.4)) for each neutrino samples.

6.4.6 Validation of NOνA Likelihood Functions

In the validation runs, both the neutrino oscillation parameters and the reconstruction widths are varied. The reconstruction widths are additionally constrained by Gaussian penalty terms. The remaining nuisance parameters are held at their respective central values[m].

Following the NOνA experiment, the following solar and reactor neutrino oscillation parameter values and constraints obtained by the PDG [149] are used,

$$\Delta m^2_{21} = 7.53 \times 10^{-5}\ \text{eV}^2 \text{ (fixed)},$$
$$\sin^2\theta_{12} = 0.307 \text{ (fixed)},$$
$$\sin^2\theta_{13} = 0.0210 \pm 0.0011 \text{ (varied but constrained)},$$

while the remaining oscillation parameters are freely varied. Some nuisance parameters are held at the central values since they are found to have only a small impact on the parameter constraints. The 2D 1σ and 3σ constraints on the relevant neutrino oscillation parameters produced by GAMBIT and NOνA are shown in Figures 6.5 and 6.6.

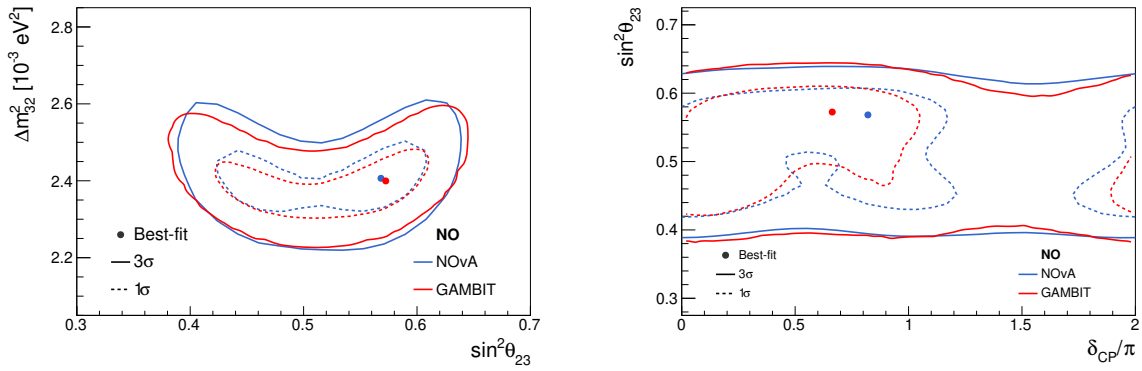


Figure 6.5: Plots comparing the 1σ and 3σ C.L. contours produced by NOνA [114] and GAMBIT, assuming normal mass ordering.

[m]It was found that the fixed parameters only marginally affect the final results. They are, therefore, kept constant to reduce the number of nuisance parameters.

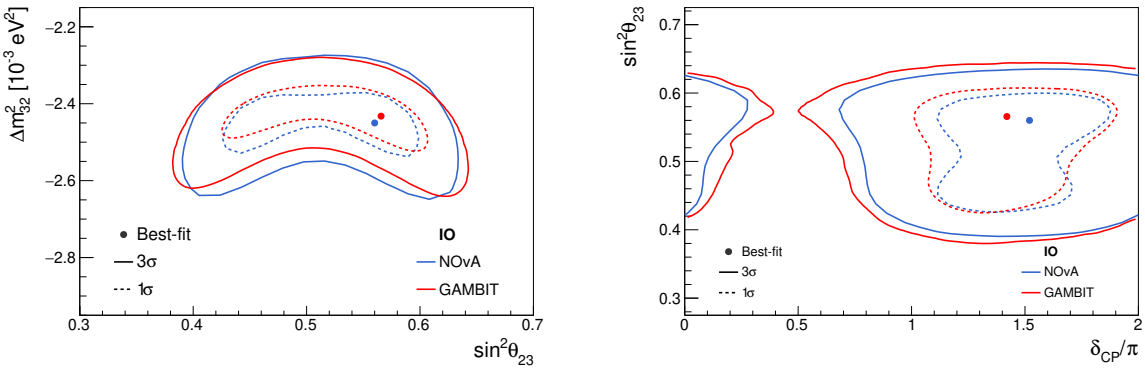


Figure 6.6: Plots comparing the 1σ and 3σ C.L. contours produced by NOνA [114] and GAMBIT, assuming inverted mass ordering.

Table 6.3 summarises the best-fit points obtained by NOνA and GAMBIT. The results generally are consistent. The largest deviation between the two is the asymmetrical error bars of the mixing angles in both NO and IO, which extend into the LO. This is likely caused by the suboptimal modelling of the appearance channels in GAMBIT, which suffer from the low signal-to-background ratios and the inability to incorporate the peripheral samples accurately.

Table 6.3: Comparison of the best-fit neutrino oscillation parameters between GAMBIT and NOνA [114]

Parameters	Normal ordering		Inverted ordering	
	GAMBIT	NOνA	GAMBIT	NOνA
$\sin^2(\theta_{23})$	$0.57^{+0.03}_{-0.13}$	$0.57^{+0.03}_{-0.04}$	$0.57^{+0.03}_{-0.12}$	0.56
Δm^2_{32} [10^{-3}eV^2]	$2.40^{+0.05}_{-0.07}$	2.41 ± 0.07	2.43 ± 0.06	2.45
$\delta_{\rm CP}$ [π]	$0.66^{+0.28}_{-0.65}$	$0.82^{+0.27}_{-0.87}$	$1.42^{+0.38}_{-0.30}$	1.52
$\Delta\chi^2_{\rm IO-NO}$ (σ)			0.38 (0.61σ)	0.9σ

Figure 6.7 shows the energy spectra of the $\nu_\mu \to \nu_\mu$, $\nu_\mu \to \nu_e$, $\bar{\nu}_\mu \to \bar{\nu}_\mu$, and $\bar{\nu}_\mu \to \bar{\nu}_e$ channels predicted by GAMBIT and NOνA, with all parameters held at the respective best-fit values. The predicted spectra are also compared to the observed spectra at the NOνA FD. The peripheral samples are shown without an energy scale since they are only used as a rate constraint. For each sample, Table 6.4 includes the predicted total numbers of events by GAMBIT and NOνA, the expected background events by NOνA, and the observed numbers of events at the NOνA FD.

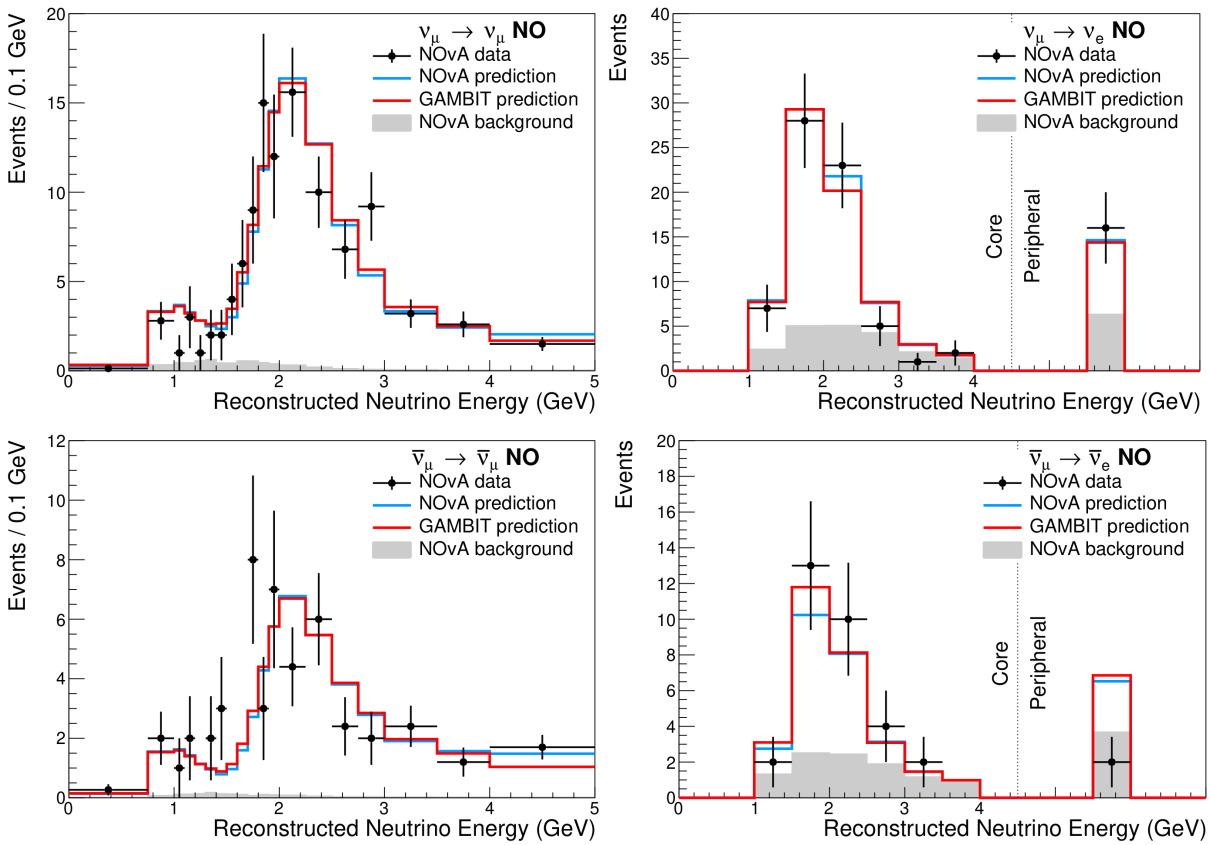


Figure 6.7: The GAMBIT and NOνA predicted FD neutrino energy spectra at their respective best-fit parameters. The peripheral samples are shown as rates and without energy scale.

Table 6.4: GAMBIT and NOνA predicted [114], and NOνA observed numbers of events at the NOνA FD at the respective best-fit points

	ν-mode		$\bar{\nu}$-mode	
	ν_μ CC	ν_e CC	$\bar{\nu}_\mu$ CC	$\bar{\nu}_e$ CC
GAMBIT predicted	223.1	83.9	101.9	35.4
NOνA predicted	222.3	85.8	105.4	33.2
NOνA background	$8.2^{+1.9}_{-1.7}$	$26.8^{+1.6}_{-1.7}$	$2.1^{+0.7}_{-0.7}$	$14.0^{+0.9}_{-0.7}$
NOνA observed	221	82	105	33

In summary, the validation of the NOνA likelihood functions within GAMBIT demonstrates good agreement with the NOνA counterparts, but minor discrepancies are still present. Both the GAMBIT and the NOνA results show a preference for the UO θ_{23} solution and NO, although the GAMBIT result does not rule out the LO solution at 1σ.

6.5 The MINOS Likelihood Functions in GAMBIT

The Main Injector Neutrino Oscillation Search (MINOS) experiment [150] was another long-baseline neutrino oscillation experiment in the US. The experiment started data collection in 2005 and was decommissioned in 2012.

Similar to the NOνA experiment, a near-far detector setup was adopted to observe the neutrinos from the NuMI beam produced at Fermilab. The 980 t near detector (Figure 6.8 right) was situated at Fermilab, a few hundred metres away from the neutrino source, while the MINOS 5.4 kt far detector (Figure 6.8 left) was located 735 km away under the Soudan Underground Laboratory in Minnesota. Both detectors were made up of alternating octagonal layers of steel calorimeter and plastic scintillator. Additionally, both detectors were magnetised, allowing the experiment to reconstruct event energy and topology with high accuracy. Different from NOνA and T2K was that the MINOS detectors laid on-axis to the neutrino beam. As a result, MINOS received a higher flux of neutrinos, which produced a broader and higher energy spectrum, as shown in Figure 6.9.



Figure 6.8: Images of the far detector (left, [151]) and the near detector (right, [152]) of the MINOS experiment. The magnetised steel-plastic far detector with a length of 30 m and a diameter of 8 m was located 735 km away from the neutrino beam source and 705 m underground inside the Soudan Underground mine. The near detector, using a similar technology, sat a few hundred metres downstream from the neutrino source at Fermilab.

Neutrino events detected by the MINOS far detector were classified into three samples: $\nu_\mu(\bar{\nu}_\mu)$ CC, $\nu_e(\bar{\nu}_e)$ CC, and NC. For the $\nu_\mu(\bar{\nu}_\mu)$ CC candidates, the neutrino energy was reconstructed as the sum

$$E_{\nu_\mu} = E_\mu + E_{\text{shower}}, \tag{6.16}$$

where E_μ is the muon energy, and E_{shower} is the hadronic shower energy. E_μ was determined from the track length if the muon track is contained or from its curvature if it is not. The hadronic shower was measured using a k-nearest-neighbour library-matching algorithm that took a few shower characteristics into account. For $\nu_e(\bar{\nu}_e)$ CC and NC candidates, the neutrino energy was measured through calorimetry.

For the MINOS baseline and beam energy, in the two-flavour formalism, the ν_μ survival oscillation

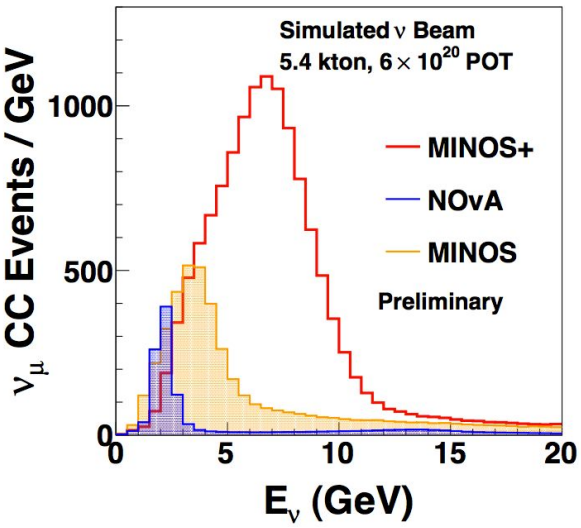


Figure 6.9: The on-axis setup of the MINOS detectors produced a much broader and higher energy spectrum compared to the NOνA off-axis design [153].

can be approximated as

$$P(\nu_\mu \to \nu_\mu) \approx 1 - \sin^2(2\theta)\sin^2\left(\frac{\Delta m^2 L}{4E}\right), \tag{6.17}$$

where E is the neutrino energy, and L is the baseline. Since θ_{13} is not zero, ν_e can appear in the beam, and it is therefore necessary to use the full three-flavour formalism [154], where

$$\sin^2(2\theta) = 4\sin^2(\theta_{23})\cos^2(\theta_{13})\left(1 - \sin^2(\theta_{23})\cos^2(\theta_{13})\right), \tag{6.18}$$

and

$$\Delta m^2 = \Delta m^2_{32} + \Delta m^2_{21}\sin^2(\theta_{12}) + \Delta m^2_{21}\cos(\delta_{\rm CP})\sin(\theta_{13})\tan(\theta_{23})\sin(2\theta_{12}). \tag{6.19}$$

The ν_e appearance probability is given by the approximation

$$P(\nu_\mu \to \nu_e) \approx \sin^2(\theta_{23})\sin^2(2\theta_{13})\sin^2\left(\frac{\Delta m^2 L}{4E}\right). \tag{6.20}$$

6.5.1 GAMBIT Prediction of MINOS Neutrino Energy Spectra

In the current GAMBIT version, only the $\nu_\mu \to \nu_\mu$ channel is incorporated due to the limited information availability. For instance, the MINOS exptected ν_e flux was not published. The neutrino energy spectra are predicted using the same equation as that used for NOνA (Equation (6.9)). The background spectrum is extracted from the MINOS prediction [155].

One single Gaussian reconstruction function is used, which introduces two nuisance parameters: the reconstruction width and the reconstruction energy offset. The unoscillated ν_μ CC energy spectrum and the selection efficiency function at the far detector are extracted from [155]. The energy spectrum is integrated with the cross-sections, which means that the related systematic uncertainties cannot be accounted for.

6.5.2 Validation of MINOS Likelihood Functions

Figures 6.10 and 6.11 show the GAMBIT and MINOS 2D constraints on the relevant neutrino oscillation parameters at the level of 1σ and 90%. Two MINOS results are included in the comparisons [133, 154]; while the former assumed two-flavour oscillation, the latter assumed three-flavour. Both, however, used the same dataset. In the MINOS three-flavour analysis, the θ_{13} parameter was constrained by $\sin^2(\theta_{13}) = 0.0242 \pm 0.0025$, a value derived from a weighted average of the results from the Daya-Bay, RENO, and Double Chooz reactor experiments [154].

The comparisons between GAMBIT and MINOS contours are imperfect, so it is difficult to draw any conclusion. This is because the MINOS constraints were produced utilising both the atmospheric and the beam data. The MINOS beam dataset also included both the neutrino and antineutrino disappearance and appearance channels, while within GAMBIT, only the $\nu_\mu \to \nu_\mu$ channel is incorporated.

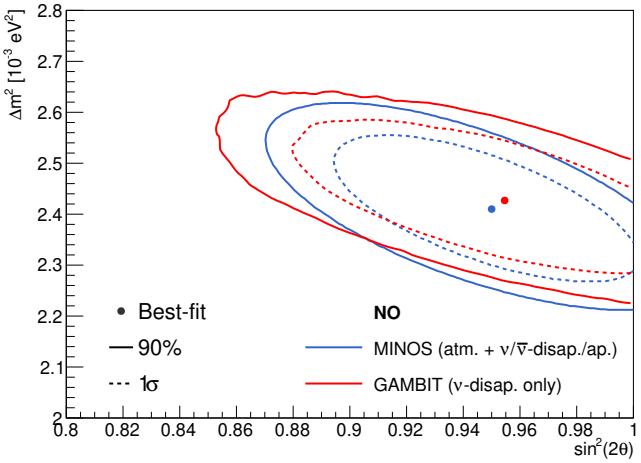


Figure 6.10: A two-flavour comparison between the GAMBIT and MINOS [133] 2D contours. For both results, the θ_{13} was a free parameter without an external constraint. Note, the GAMBIT result only includes the $\nu_\mu \to \nu_\mu$ channel.

Figure 6.12 shows the comparison between the MINOS spectra predicted by GAMBIT and MINOS, with the parameters set to the best-fit values. The observed energy spectrum, marked as discrete data points, is also included. The two spectra do not match exactly due to the imperfect representation of the MINOS experiment within GAMBIT.

Table 6.5 contains the best-fit points determined by GAMBIT and MINOS. The large asymmetrical error bars on the $\sin^2(\theta_{23})$ are caused by the octant degeneracy. The absence of ν_e appearance channels further reduces the ability of the MINOS likelihood function within GAMBIT to predict the octant, as shown by the difference between the 1σ contours. The δ_{CP} parameter is not well-constrained by either study, so the error bar is omitted.

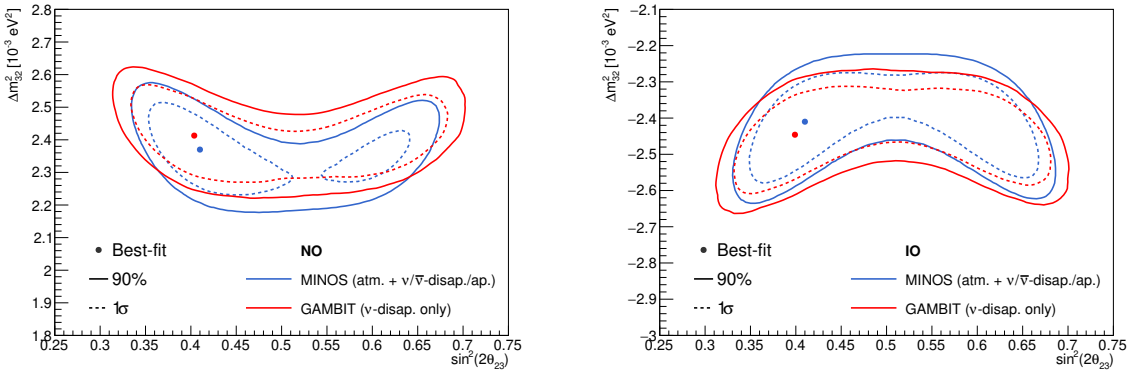


Figure 6.11: 2D contour comparisons between GAMBIT and MINOS [154] in three-flavour, where the external constraint $\sin^2(\theta_{13}) = 0.0242 \pm 0.0025$ based on a weighted average of the results from the Daya-Bay, RENO, and Double Chooz experiments was applied. Note, the GAMBIT result only includes the $\nu_\mu \to \nu_\mu$ channel.

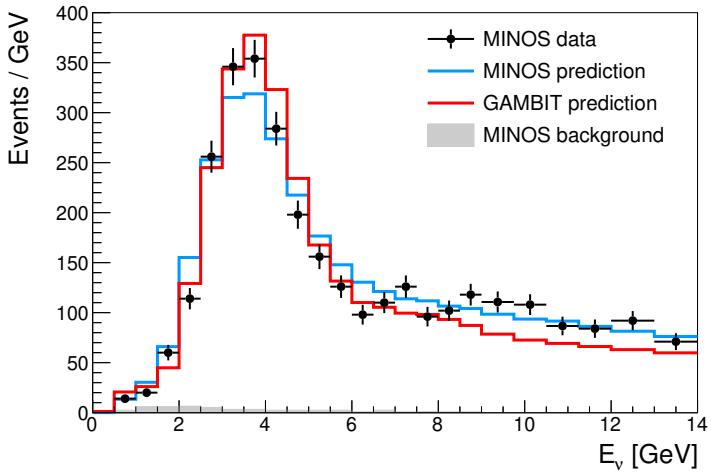


Figure 6.12: Comparison of GAMBIT and MINOS [133] spectra at their respective best-fit points

Table 6.5: Comparison of the best-fit neutrino oscillation parameters between GAMBIT and MINOS [154]

Parameters	Normal ordering		Inverted ordering	
	GAMBIT	MINOS	GAMBIT	MINOS
$\sin^2(\theta_{23})$ (90% C.L.)	$0.40^{+0.30}_{-0.08}$	$0.41^{+0.24}_{-0.06}$	$0.40^{+0.30}_{-0.08}$	$0.41^{+0.26}_{-0.07}$
Δm^2_{32} $[10^{-3}\text{eV}^2]$	$2.41^{+0.12}_{-0.11}$	2.37 ± 0.09	$-(2.45^{+0.12}_{-0.10})$	$-(2.41^{+0.12}_{-0.09})$
δ_{CP} $[\pi]$	1.00	0.44	1.00	0.62
$\Delta\chi^2_{\text{NO-IO}}$ (σ)	0.008 (0.09σ)	0.23 $(\sim 0.48\sigma)$		

6.6 The KamLAND Likelihood Functions in GAMBIT

The Kamioka Liquid Scintillator Antineutrino Detector (KamLAND) experiment is a neutrino oscillation experiment designed to detect neutrinos generated from nuclear power reactors. The detector is located at the underground Kamioka Observatory in Hida, Japan. The KamLAND detector, as shown in Figure 6.13, is composed of two parts: the Outer Detector (OD) and the combination of the LS balloon and PMTs forming the Inner Detector (ID).

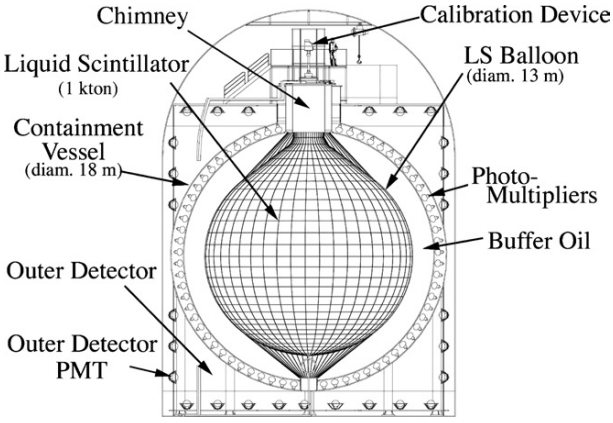


Figure 6.13: A schematic diagram of the KamLAND detector [24]

The KamLAND OD is a 3.2 kt cylindrical water Cherenkov detector consisting of 225 20-inch PMTs designed to study and suppress background events generated from cosmic muons and the surrounding radioactive processes. The water layer of the OD also acts as additional muon shielding. The Inner Detector volume is dominated by a 13-m-diameter balloon filled with 1 kt of liquid scintillator. This balloon is supported by the buoyancy of the buffer oil layer and is contained in an 18-m-diameter containment vessel, on which 1325 17-inch PMTs and 554 20-inch PMTs are mounted.

The KamLAND experiment measures the $\bar{\nu}_e$ flux originated predominantly from 56 nuclear reactors in Japan [n] via the inverse β-decay (IBD) channel,

$$\bar{\nu}_e + p \to e^+ + n. \tag{6.21}$$

The IBD events in KamLAND can be distinctly selected thanks to the delayed coincidence (DC) of the positron annihilation (the 'prompt event') and the following signal from the neutron capture on a proton or a ^{12}C nucleus.

The threshold neutrino energy $E_{\rm th}$ of the IBD process is

$$E_{\rm th} \approx m_{e^+} + m_n - m_p \approx 1.804 \text{ MeV}, \tag{6.22}$$

where we assume no nucleon recoil[o]. In the detector, the product e^+ annihilates and produces a pair of photons (a 'prompt event'). Roughly speaking, any extra energy provided above the threshold energy

[n] This number fluctuates over time as old reactors are decommissioned and new reactors are activated.
[o] The average neutron recoil energy is $\mathcal{O}(10$ KeV) [128].

goes into the kinetic energy of the positron, $T \approx E_\nu - E_{\rm th}$; therefore, the scintillation light is then detected to have an energy of

$$E_{\rm prompt} = 2m_e + T = 2m_e + E_{\bar{\nu}_e} - E_{\rm th}, \tag{6.23}$$

and hence the electron antineutrino energy can be measured by

$$E_{\bar{\nu}_e} \approx E_{\rm prompt} + m_n - m_e - m_p \approx E_{\rm prompt} + 0.782 \text{ MeV}. \tag{6.24}$$

The $\bar{\nu}_e$ disappearance is the only channel that is observed because the reactor neutrinos do not have sufficient energy to produce heavier final state products.

In GAMBIT, there are two module functions representing the KamLAND experiment, one for predicting the $\bar{\nu}_e$ energy spectrum and the other for constraining the related nuisance parameters. Similar to the case of NOνA, the expected number of $\bar{\nu}_e$ events in bin i is given by the equation [p]

$$N_i^{\rm IBD,\bar{\nu}_e} = \int_{E_i}^{E_{i+1}} {\rm d}E_{\rm rec} \int_0^\infty R\left(E_{\rm rec}|E_\nu\right) \frac{{\rm d}\Phi_\nu}{{\rm d}E_\nu} \sigma_{\rm IBD}\left(E_\nu\right) \epsilon\left(E_\nu\right) P_{\bar{\nu}_e \to \bar{\nu}_e}\left(E_\nu\right) {\rm d}E_\nu, \tag{6.25}$$

and the total expected number of events in bin i is

$$N_i = N_i^{\rm bkg} + N_i^{\rm IBD,\bar{\nu}_e}, \tag{6.26}$$

where the symbols inherit the same meanings from Equations (6.9) and (6.10).

The KamLAND likelihood functions in GAMBIT use data from the fourth official data release [129], corresponding to reference [128], which includes data collected from March 2002 to November 2009, summing to a total live-time of 2135 days.

6.6.1 Neutrino Fluxes at KamLAND

The 56 commercial nuclear power reactors across Japan contribute the majority of the total $\bar{\nu}_e$ flux at the KamLAND detector. The baseline of each reactor differs, ranging from the shortest of 88 km (Shika Nuclear Power Plant) to the longest of 830 km (Sendai Nuclear Power Plant). The flux-weighted average baseline is around 180 km. The Korean nuclear reactors also contribute to the $\bar{\nu}_e$ flux, accounting for $(3.4 \pm 0.3)\%$ of the total neutrino flux at KamLAND. The remaining nuclear reactor contribution across the globe and the few Japanese nuclear research reactors is $(1.0 \pm 0.5)\%$.

The $\bar{\nu}_e$ flux $S(E_\nu)$ is related to the thermal energy output, $E_{\rm th}$, by the equation,

$$S(E_\nu) = \frac{E_{\rm th}}{\langle E_{\rm fission} \rangle} \sum_i f_i \frac{{\rm d}N_i}{{\rm d}E_\nu}, \tag{6.27}$$

where

- the sum runs over possible fission fuel elements,
- f_i is the effective [q] fractional fission yield of fission fuel i, $\sum_i f_i = 1$,

[p] Here, for simplicity, ν is used to denote quantities related to electron antineutrino.
[q] Here 'effective' means averaged over a certain operational time.

- $\frac{\mathrm{d}N_i}{\mathrm{d}E_\nu}$ is the $\bar{\nu}_e$ energy spectrum of species i per fission,
- $\langle E_{\text{fission}} \rangle = \sum_i f_i E_i$ is the (yield-weighted) average effective thermal energy per fission, E_i.

Equation (6.27) can be understood as a yield-weighted average of $\bar{\nu}_e$ spectra per fission and scaled by the total number of fission in a time period. And, at the KamLAND detector, assuming 100% efficiency and no oscillation, the reactor $\bar{\nu}_e$ flux is

$$\frac{\mathrm{d}\Phi_\nu}{\mathrm{d}E_\nu} = \sum_j \frac{S_j(E_\nu)}{4\pi L_j^2}, \tag{6.28}$$

where the sum runs over all relevant reactors, and L_j is the distance between reactor j and the detector.

For the nuclear power reactors relevant to KamLAND, 99% of the energy output comes from the fission of ^{235}U, ^{238}U, ^{239}Pu, and ^{241}Pu. The effective fractional yield over the live-time corresponding to the KamLAND result [128] is (0.571 : 0.078 : 0.295 : 0.056) respectively. The thermal power output $P_{\text{th}} = \int E_{\text{th}} dt$ is related to the electric power output P_{el} by an efficiency factor of 0.33, $P_{\text{el}} = 0.33 P_{\text{th}}$ [156].

The neutrino fluxes per fission in GAMBIT for the KamLAND likelihood functions are from [157], which is an update to those used in the KamLAND paper. The recalculation achieved good improvements on the predictions of ^{235}U, ^{239}Pu, and ^{241}Pu spectra, but ^{238}U prediction remained largely theoretical due to the lack of total β spectra measurement. Compared to the spectra used in the KamLAND paper, the recalculation introduced an average +3% shift to the normalisation.

Within GAMBIT, the publicly available operational records of the nuclear facilities published by the Japan Nuclear Energy Safety Organization [158] and the Japan Atomic Industrial Forum [159] are used to calculate the reactor neutrino flux at KamLAND. These records, however, contain only monthly power output, compared to the weekly temporal information during stable operation and sometimes even down to sub-hour granularity that the KamLAND experiment has access to.

Despite the powerful background suppression, some processes can mimic the DC signals and become indistinguishable from the reactor neutrino events. The dominant background comes from the $^{13}\mathrm{C}(\alpha, \mathrm{n})^{16}\mathrm{O}$ reactions, where a neutron and an ^{16}O are generated when an α particle is captured by a ^{13}C atom. The main source of the α particles is the α-decays of ^{210}Po in the LS. The $^{13}\mathrm{C}(\alpha, \mathrm{n})^{16}\mathrm{O}$ was reduced significantly after the LS purification programme in 2007. In GAMBIT, time-dependent energy resolution was introduced as an attempt to capture the difference before and after the LS purification, but it was found to have little impact on the final parameter constraint; therefore, the feature was not enabled in the validation process.

In GAMBIT, a flux normalisation parameter is added to account for the absent flux contribution from nuclear reactors outside Japan. The parameter also accounts for the uncertainty in fiducial volume and other sources of error, such as the non-equilibrium correction and spent nuclear fuel correction. The conversion efficiency from thermal power to electric power also contributes to this uncertainty. Due to the lack of detailed information on how these are estimated in the paper, their effects on the neutrino energy

spectra are highly degenerate. We therefore use only one energy-independent normalisation parameter to represent the overall impact.

GAMBIT calculates the background spectrum by multiplying each contributing background source by a scaling factor then summing the adjusted spectra into one. These background scaling factors are treated as nuisance parameters and profiled away in the scanning process. Figure 6.17a shows the comparison of the unoscillated $\bar{\nu}_e$ fluxes at KamLAND, produced by GAMBIT and KamLAND.

6.6.2 Reconstruction Functions

The KamLAND experiment does not publish migration matrices, so a Gaussian smearing function is used to emulate the effect. There are two parameters that control the smear effect: the energy offset Δ_{rec} and the energy-dependent reconstruction width σ_{rec} where

$$\sigma_{\text{rec}}(E_\nu) = \sigma_{\text{const.}}\sqrt{E_\nu}, \tag{6.29}$$

and $\sigma_{\text{const.}}$ is energy-independent. Both Δ_{rec} and $\sigma_{\text{const.}}$ are treated as nuisance parameters. The Gaussian smearing function is written as

$$R(E_{\text{rec}}|E_\nu) \equiv \frac{1}{\sigma_{\text{rec}}\sqrt{2\pi}} \exp\left\{-\frac{1}{2}\left(\frac{E_{\text{rec}} - (E_\nu + \Delta_{\text{rec}})}{\sigma_{\text{rec}}}\right)^2\right\}. \tag{6.30}$$

6.6.3 Efficiency Function

The selection efficiency is published as a function of E_{prompt} in [128], and each data point is an average across the detector live-time. The efficiency plot was digitised and converted to that as a function of neutrino energy, as shown in Figure 6.14.

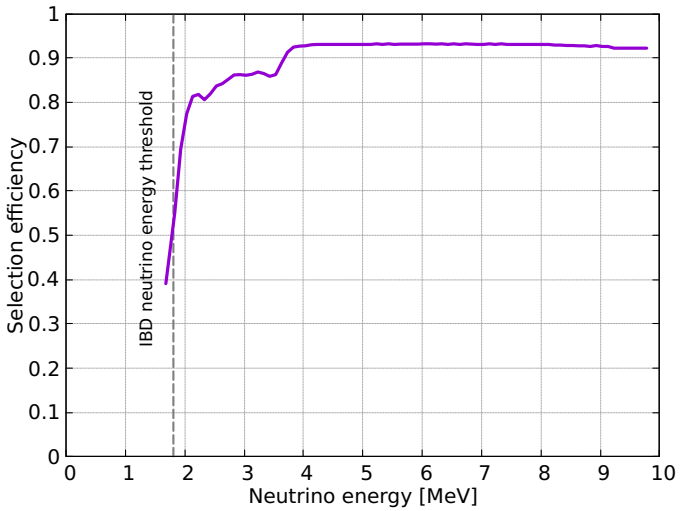


Figure 6.14: The KamLAND selection efficiency function digitised from [128]. The data points close to the energy threshold were added for interpolation.

6.6.4 IBD Cross-sections

The total IBD cross-section is tabulated using the method described in [160], and the result is shown in Figure 6.15. The calculation includes the correction terms that are first order in $1/M$, where M is the

nucleon mass.

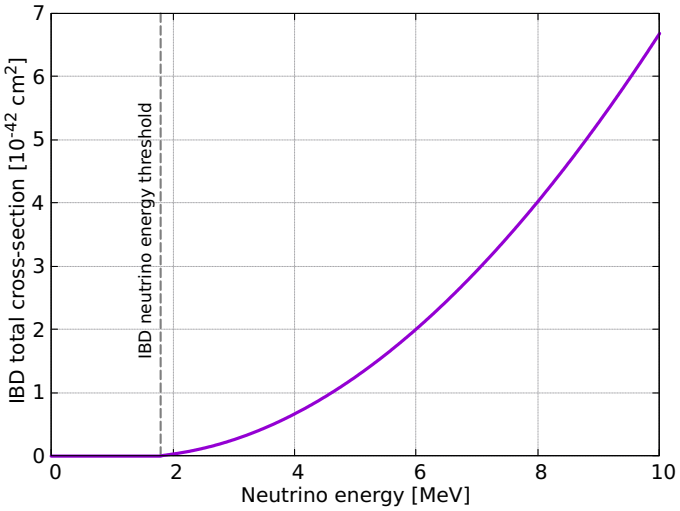


Figure 6.15: The IBD total cross-section used in the KamLAND likelihood functions.

6.6.5 Validation of KamLAND Likelihood Functions

In the validation of the KamLAND likelihood functions within GAMBIT, all nuisance parameters were varied and constrained by Gaussian penalty terms. The neutrino oscillation parameters θ_{12}, θ_{13}, and Δm^2_{21} were free, while the rest were held constant at the following values:

$$\theta_{23} = 0.83,$$
$$\Delta m^2_{32} = 2.45 \times 10^{-3}\ \text{eV}^2,$$
$$\delta_{\text{CP}} = 0,$$

in accordance to the method adopted by KamLAND ([128], parameter values are not specified). Figure 6.16 shows the resulting 2D 1σ and 3σ C.L. contours for the relevant neutrino oscillation parameters, and the best-fit points are listed in Table 6.6.

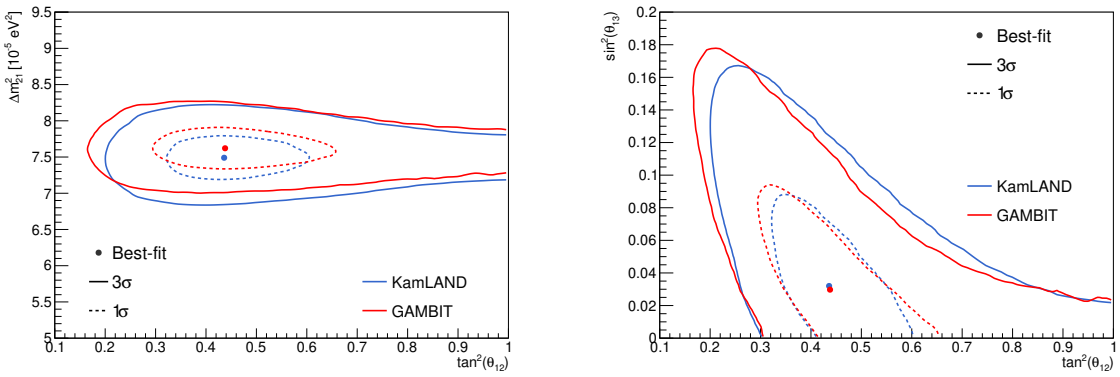


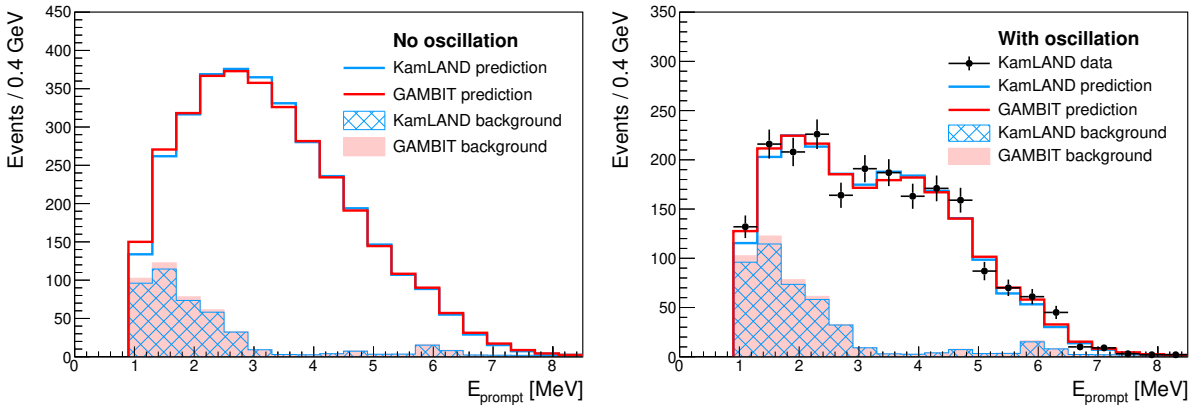
Figure 6.16: The 1σ and 3σ C.L. contours set by GAMBIT and KamLAND [128]. A noticeable shift in the high Δm^2_{21} direction is present, but size is small.

At the best-fit points, the prompt energy spectra at KamLAND as predicted by GAMBIT agree well with the KamLAND prediction and observation, as can be seen in Figure 6.17. The numbers of events

Table 6.6: Comparison of the best-fit neutrino oscillation parameters between GAMBIT and KamLAND (KamLAND-only, 3-ν, free θ_{13}, [128])

Parameters	GAMBIT	KamLAND
$\tan^2(\theta_{12})$	$0.438^{+0.149}_{-0.099}$	$0.436^{+0.102}_{-0.081}$
Δm^2_{21} $[10^{-5}\text{eV}^2]$	7.62 ± 0.18	7.49 ± 0.20
$\sin^2(\theta_{13})$	$0.030^{+0.043}_{-0.030}$	0.032 ± 0.037

under different categories are summarised in Table 6.7. The GAMBIT predicted numbers are consistent with the KamLAND results.



(a) No neutrino oscillation

(b) With neutrino oscillation

Figure 6.17: The unoscillated (left) and oscillated (right) prompt energy spectra predicted by GAMBIT and KamLAND, using the respective best-fit parameter values. The GAMBIT predictions are consistent with the KamLAND results and fit well with the KamLAND observation.

Table 6.7: GAMBIT and KamLAND predicted [128], and KamLAND observed numbers of events at the respective best-fit points. Note, the background counts include the oscillated geo-neutrinos from U and Th decays.

	GAMBIT	KamLAND
Reactor (no osc.)	2868	2879
Reactor (signal)	1636	1634
Background	464.4	431.9
Total expected	2101	2066
KamLAND Observed		2106

The KamLAND likelihood functions within GAMBIT produce results that are consistent with those of KamLAND. However, a minor systematic Δm^2_{21} shift towards the higher value is present. This is likely caused by the difference in the choice of $\bar{\nu}_e$ spectra per fission. Specifically, the updated spectra [157] introduce an average +3% normalisation originating mostly from the low energy region.

6.7 Preliminary Global Fit Results

Preliminary global scans were performed to prepare for the final complete neutrino oscillation global fits, and in this section, the results from these preliminary scans are shown.

In the preliminary scans, all eight neutrino experiments listed in Table 6.2 were included. All neutrino oscillation parameters were free to vary, but all nuisance parameters were held constant at their best-fit points. By doing so, it is possible to validate the reliability of the software and look for potential issues that could emerge in a complete scan. It is worth stressing that the production scans, which are under preparation, will be different from the preliminary scans shown here, where, most importantly, the nuisance parameters will be varied and profiled away.

In these preliminary global fits, the experiments included were assumed to be independent with no correlation. This was mainly due to the fact that the nuisance parameters were held constant, prohibiting accounting for any cross-experiment correlations. However, in production runs, certain correlations, particularly those related to neutrino fluxes and neutrino-nuclear interactions, may become significant and require closer scrutiny. We in addition foresee those related to detector designs and reconstruction to be small and negligible. Background correlations may also be neglected due to the lack of detailed modelling methods, but we expect this to be a minor effect.

Figures 6.18 and 6.19 show the preliminary GAMBIT 2D neutrino oscillation parameter constraints at the levels of 1σ, 2σ, and 3σ, assuming normal mass ordering and inverted mass ordering, respectively. The best-fit neutrino oscillation parameters found by GAMBIT in the preliminary scans are listed in Tables 6.8 and 6.9 and are compared to other neutrino oscillation global fit studies. The comparisons between the best-fit points are visualised in Figures 6.20 to 6.25 and discussed in the following subsections.

It is particularly interesting to point out that the preliminary GAMBIT results, which did not examine the nuisance parameter effects, show a preference for IO. This conclusion may change when the nuisance parameters are taken into account, as suggested by the validations of NOνA likelihood functions in GAMBIT in Section 6.4, for example.

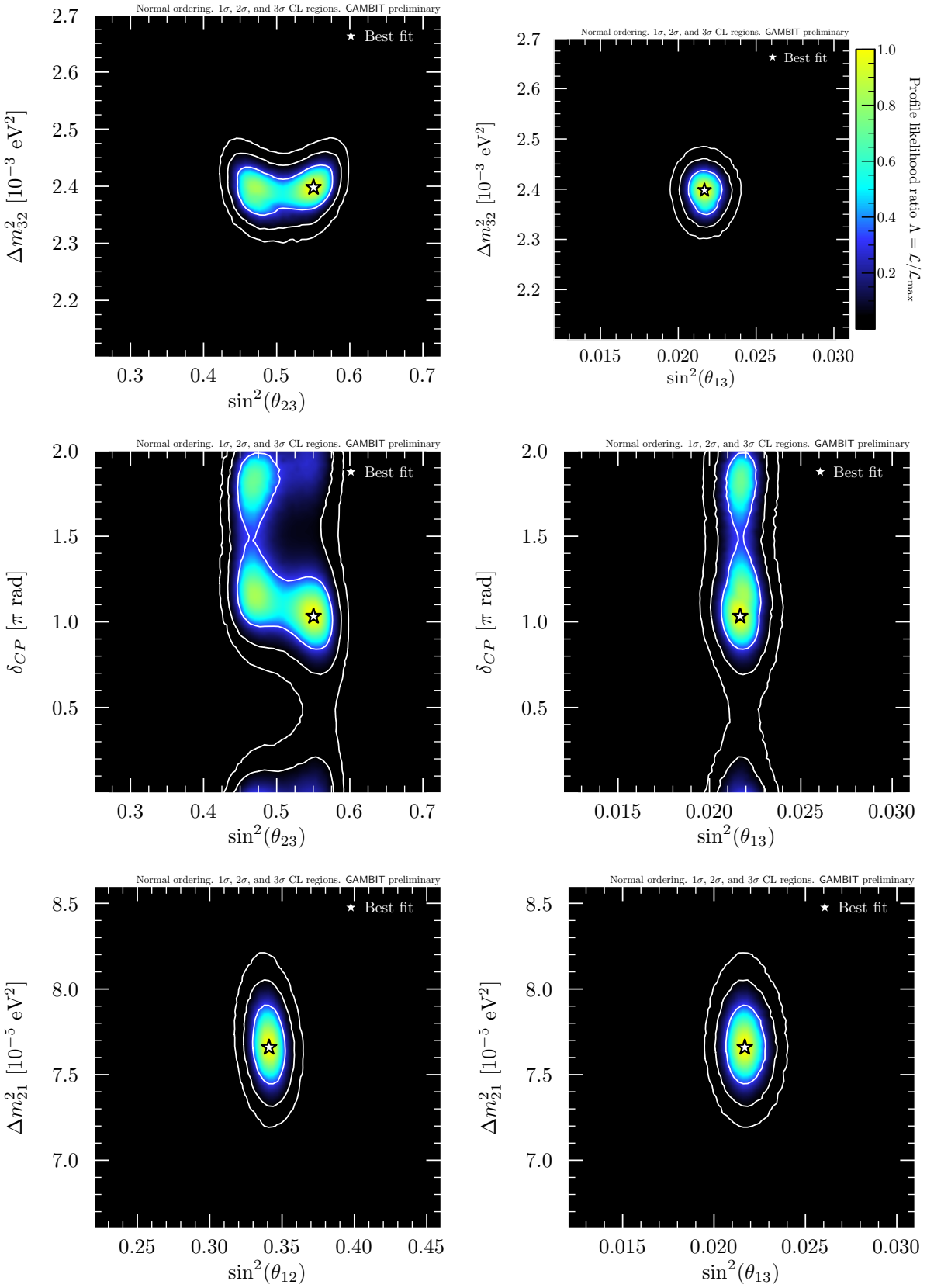


Figure 6.18: Two-dimensional 1σ, 2σ, and 3σ C.L. contours for the neutrino oscillation parameters within GAMBIT, assuming normal mass ordering

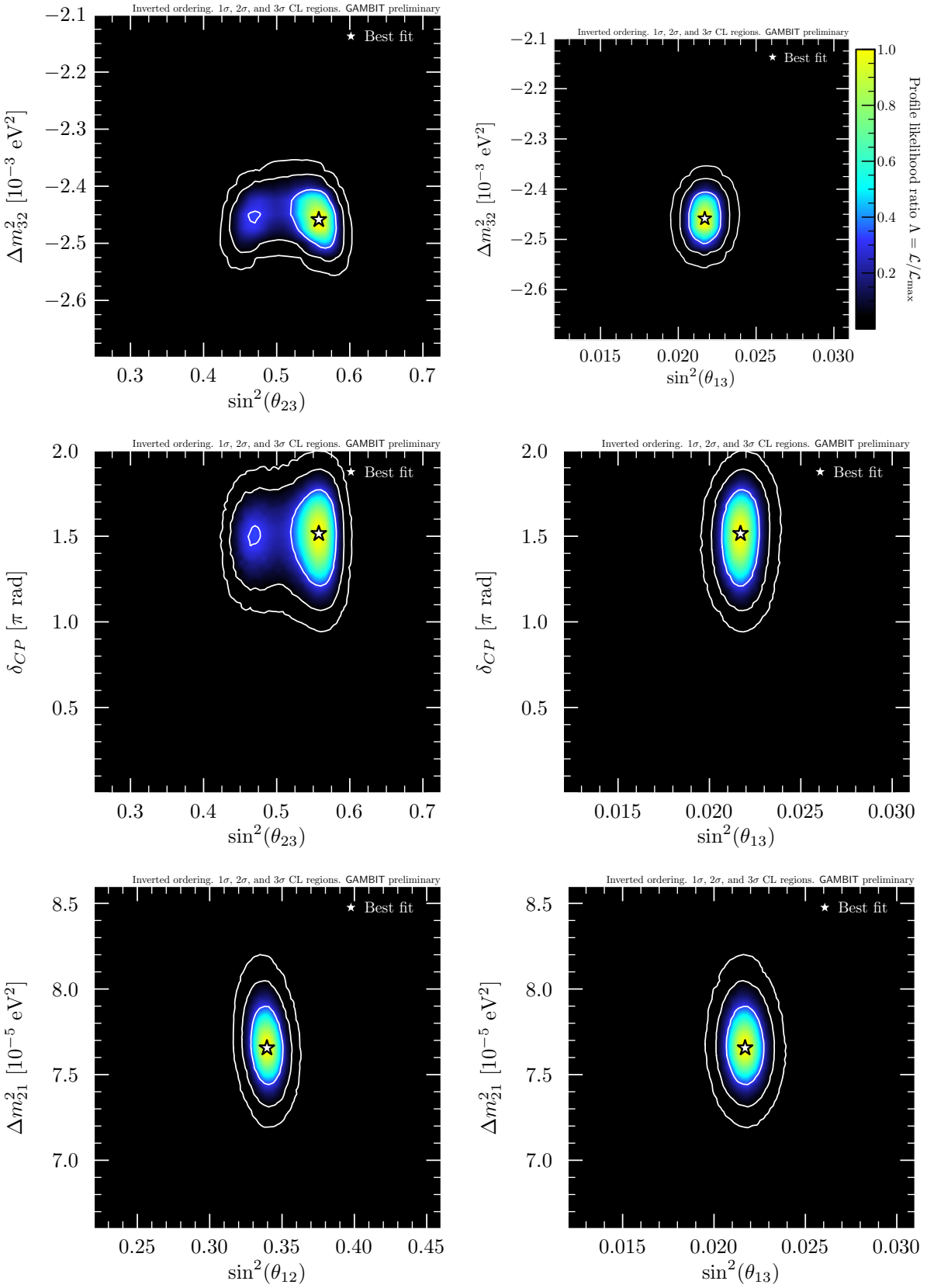


Figure 6.19: Two-dimensional 1σ, 2σ, and 3σ C.L. contours for the neutrino oscillation parameters within GAMBIT, assuming inverted mass ordering

Table 6.8: The best-fit parameters of different neutrino oscillation global studies [45, 119, 46, 47], assuming normal mass ordering

Parameters	Neutrino oscillation global fits (assuming normal ordering)			
	NuFIT	València	Bari	GAMBIT (preliminary)
$\sin^2(\theta_{12})$	$0.307^{+0.012}_{-0.011}$	0.318 ± 0.016	0.303 ± 0.013	0.341 ± 0.008
$\sin^2(\theta_{13})$	$0.02224^{+0.00056}_{-0.00057}$	$0.02200^{+0.00069}_{-0.00062}$	$0.0223^{+0.0007}_{-0.0006}$	$0.0217^{+0.0008}_{-0.0007}$
$\sin^2(\theta_{23})$	$0.454^{+0.019}_{-0.016}$	0.574 ± 0.014	$0.455^{+0.018}_{-0.015}$	$0.550^{+0.019}_{-0.031}$
Δm^2_{21} [10^{-5} eV^2]	$7.41^{+0.21}_{-0.20}$	$7.50^{+0.22}_{-0.20}$	$7.36^{+0.16}_{-0.15}$	$7.66^{+0.16}_{-0.15}$
Δm^2_{32} [10^{-3} eV^2]	$2.43^{+0.02}_{-0.03}$	$2.48^{+0.02}_{-0.03}$	$2.45^{+0.02}_{-0.03}$	2.40 ± 0.03
$\delta_{\rm CP}$ [π rad]	$1.29^{+0.22}_{-0.14}$	$1.08^{+0.13}_{-0.12}$	$1.24^{+018}_{-0.13}$	$1.04^{+0.25}_{-0.13}$

Table 6.9: The best-fit parameters of different neutrino oscillation global studies [45, 119, 46, 47], assuming inverted mass ordering

Parameters	Neutrino oscillation global fits (assuming inverted ordering)			
	NuFIT	València	Bari	GAMBIT (preliminary)
$\sin^2(\theta_{12})$	$0.307^{+0.012}_{-0.011}$	0.318 ± 0.016	0.303 ± 0.013	0.340 ± 0.008
$\sin^2(\theta_{13})$	$0.02222^{+0.00069}_{-0.00057}$	$0.02225^{+0.00064}_{-0.00070}$	0.0223 ± 0.0006	0.0217 ± 0.0007
$\sin^2(\theta_{23})$	$0.568^{+0.016}_{-0.021}$	$0.578^{+0.010}_{-0.017}$	$0.569^{+0.013}_{-0.021}$	$0.558^{+0.017}_{-0.022}$
Δm^2_{21} [10^{-5}eV^2]	$7.41^{+0.21}_{-0.20}$	$7.5^{+0.22}_{-0.20}$	$7.36^{+0.16}_{-0.15}$	$7.66^{+0.16}_{-0.14}$
Δm^2_{32} [10^{-3}eV^2]	$-(2.487^{+0.024}_{-0.027})$	$-(2.53^{+0.02}_{-0.03})$	$-(2.49 \pm 0.03)$	$-(2.46 \pm 0.04)$
$\delta_{\rm CP}$ [π rad]	$1.52^{+0.13}_{-0.14}$	$1.58^{+0.15}_{-0.16}$	$1.52^{+0.14}_{-0.15}$	$1.52^{+0.18}_{-0.22}$
$\Delta\chi^2_{\rm IO-NO}$ (σ)	9.1 (3.0σ)	6.4 (2.5σ)	6.5 (2.5σ)	-1.7 (1.3σ)

6.7.1 Comparing Best-fit $\sin^2(\theta_{12})$

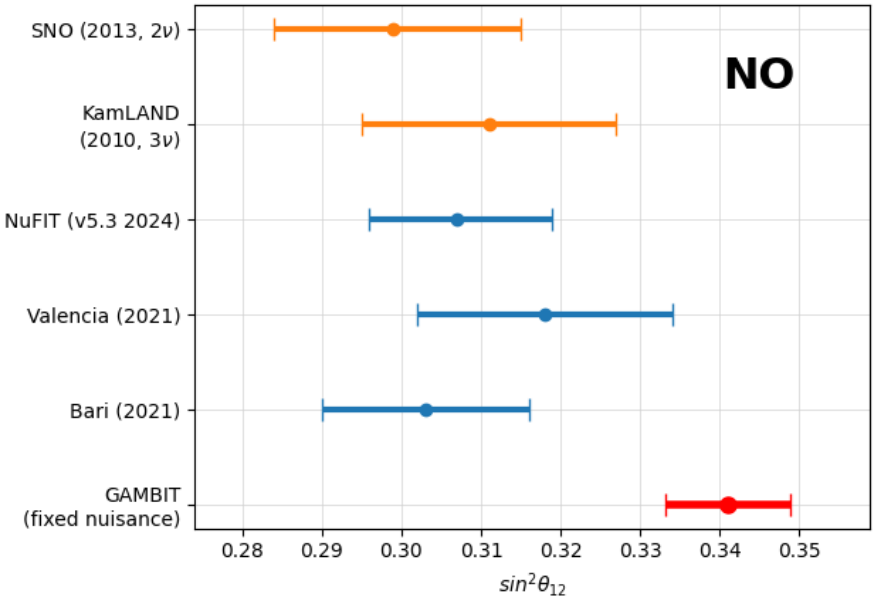


Figure 6.20: Comparison of the best-fit values and 1σ C.L. for $\sin^2(\theta_{12})$ by GAMBIT (red), the dominant experiments (orange, reference listed in Table 6.2), and global fits (blue, [45, 119, 46, 47]), assuming NO.

Figure 6.20 shows the best-fit values for $\sin^2(\theta_{12})$ determined by GAMBIT, the dominant experiments SNO and KamLAND (refer to Table 6.2 for the main citations), and the global fit studies [45, 119, 46, 47].

A large discrepancy can be seen between the GAMBIT value and other results in Figure 6.20. This is suspected to be the result of the adaptation of a different solar model. Two main factors are important when it comes to the configuration of a solar model; one is the 'generation' of the model, and the other is the solar abundance. In GAMBIT, the B16(AGSS09) solar model, which is based on a new generation of solar models [161] and the revised solar abundance study [162], is used. Compared to the preceding solar models, such as the GS98 (high metallicity) model based on [163], the AGSS09 model yields a substantially lower solar metallicity. Although the AGSS09 model has become the new standard for the determination of the element abundances for astronomical objects that are solar-dependent, several problems related to solar properties have also been introduced[r]. It is currently not possible to experimentally determine which metallicity is correct due to the large uncertainties in the solar flux measurements.

The result published by SNO was obtained using the BS05(OP) solar model [164] for its conservative model uncertainties. The Super-K solar experiment (not included in this study) used the SNO measurement to constrain the ^{8}B flux, which explains why the Super-K result also prefers a lower value of $\sin^2(\theta_{12})$ [165].

A separate study is in progress to quantify the dependency of the global fit on the choice solar model.

[r]For a comprehensive review of solar models, refer to [161].

6.7.2 Comparing Best-fit $\sin^2(\theta_{13})$

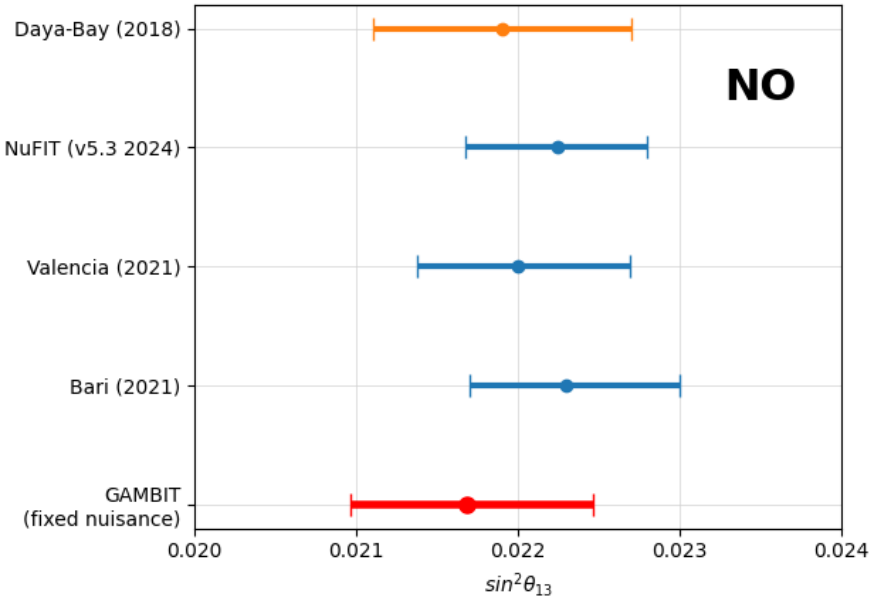


Figure 6.21: Comparison of the best-fit values and 1σ C.L. for $\sin^2(\theta_{13})$ by GAMBIT (red), the dominant experiment (orange, reference listed in Table 6.2), and global fits (blue, [45, 119, 46, 47]), assuming NO.

The resulting constraint on the mixing angle θ_{13} estimated by GAMBIT agrees with the Daya-Bay experiment and other global fit studies well, as shown in Figure 6.21. The small divergence from the rest of the global fits can be explained by the fact that the Daya-Bay experiment is the only dominant experiment included in GAMBIT.

6.7.3 Comparing Best-fit $\sin^2(\theta_{23})$

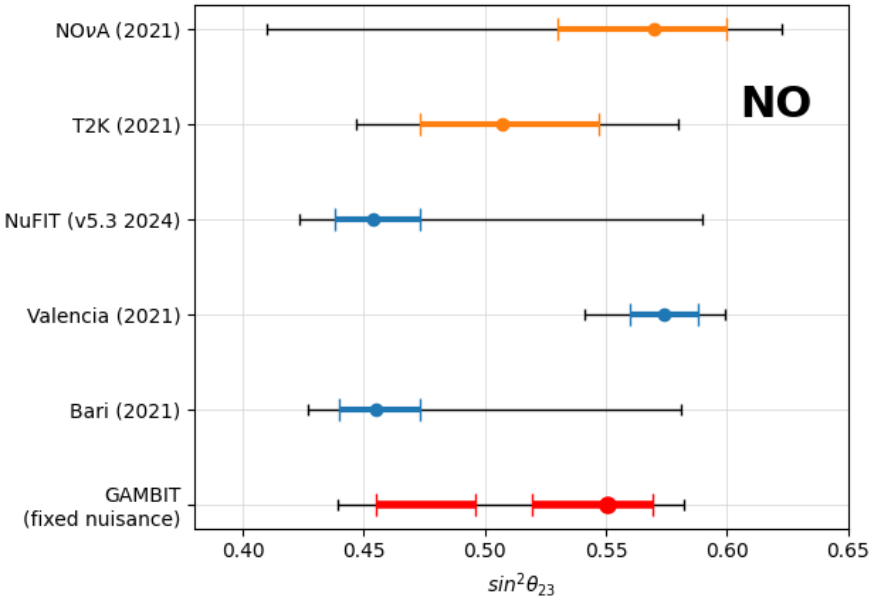


Figure 6.22: Comparison of the best-fit values, 1σ (coloured), and 2σ (black) C.L. for $\sin^2(\theta_{23})$ by GAMBIT (red), the dominant experiments (orange, reference listed in Table 6.2 except T2K for which the values are sourced from [166] for the T2K-only values), and global fits (blue, [45, 119, 46, 47]), assuming NO.

The data points in Figure 6.22 are separated into two groups, one in favour of the LO solution and the other in favour of the UO. This grouping is mainly caused by the difference in the Super-K atmospheric data included[s]. Since the latest Super-K atmospheric data [167] exhibits a stronger preference towards the LO solution, the NuFIT (ver. 5.3) and Bari results, which included the latest dataset, both support the LO. The València and the GAMBIT results prefer the UO since the 2018 Super-K dataset [130] was used.

The black bounds in Figure 6.22 indicate the 2σ intervals. They show that apart from the València result, which excludes the LO option at a level of $\sim 2.4\sigma$, none excludes the LO solution at 2σ. The GAMBIT preliminary scan did not exclude the LO solution at 1σ, hence the GAMBIT result in Figure 6.22 is shown with two disconnected regions.

[s]Note that the octant degeneracy is slightly broken by the atmospheric data due to the matter effects as neutrinos travel through the Earth.

6.7.4 Comparing Best-fit Δm^2_{21}

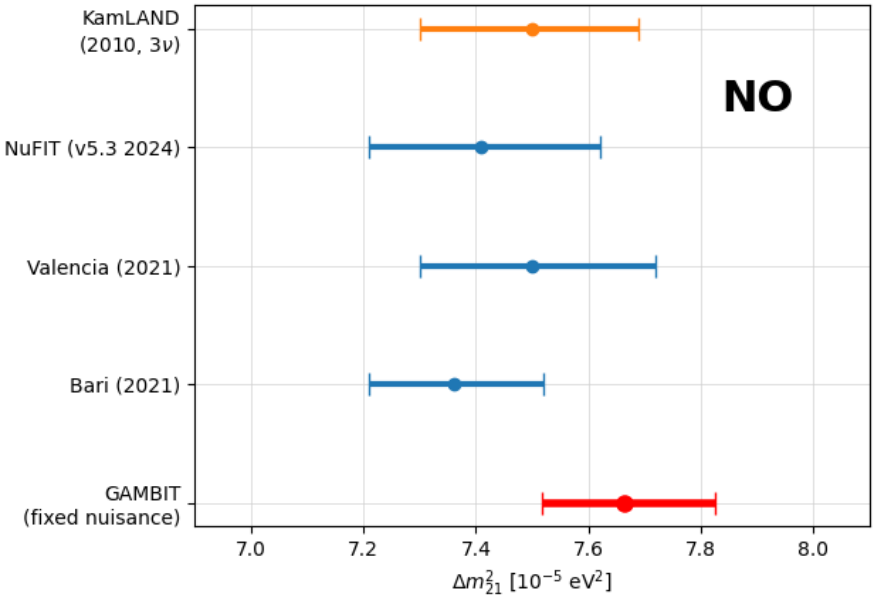


Figure 6.23: Comparison of the best-fit values and 1σ C.L. for Δm^2_{21} by GAMBIT (red), the dominant experiment (orange, reference listed in Table 6.2), and global fits (blue, [45, 119, 46, 47]), assuming NO.

Figure 6.23 compares the GAMBIT constraint on Δm^2_{21} to those set in other studies. The dominant experiment that produces the most stringent limits on Δm^2_{21} is the KamLAND experiment. And because of the slight systematic upward shift seen in the left panel of Figure 6.16, the GAMBIT best-fit value also sits slightly higher than the other results. But overall, all measurements are decently consistent.

6.7.5 Comparing Best-fit Δm^2_{32}

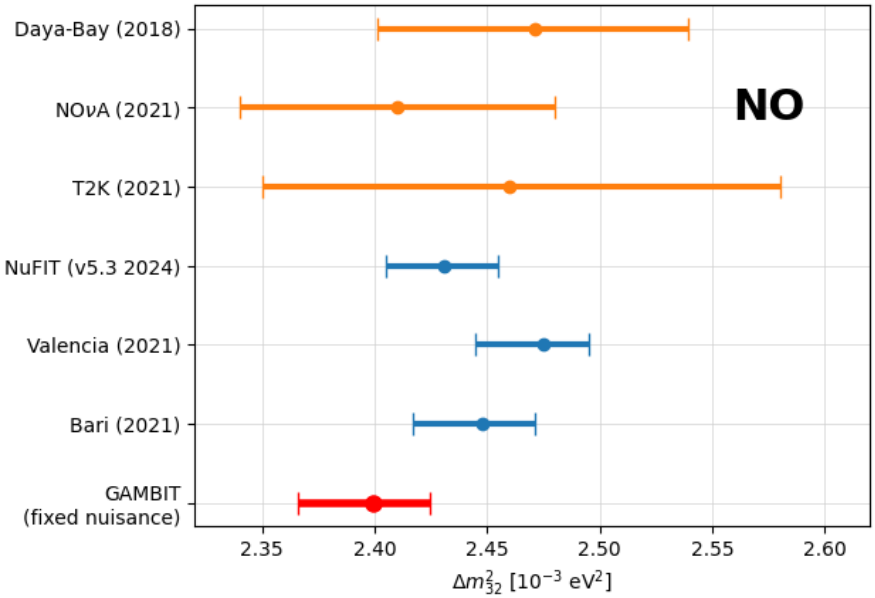


Figure 6.24: Comparison of the best-fit values and 1σ C.L. for Δm^2_{32} by GAMBIT (red), the dominant experiments (orange, reference listed in Table 6.2 except T2K for which the values are sourced from [166] for the T2K-only values), and global fits (blue, [45, 119, 46, 47]), and global fits (blue, [45, 119, 46, 47]), assuming NO.

The Δm^2_{32} best-fit value is slightly smaller than the results obtained in other studies, as seen in Figure 6.24. There are two reasons for this issue. First, the nuisance parameters were not scanned but rather were held constant at the best-fit values, reducing the freedom greatly. Second, there was an inconsistency between the default and the the production settings for the MINOS likelihood function. It further amplified the problem, pulling the GAMBIT best-fit Δm^2_{32} value lower. The inconsistency was corrected in subsequent runs; however, the results could not be generated in time due to computational resource constraints.

6.7.6 Comparing Best-fit δ_{CP}

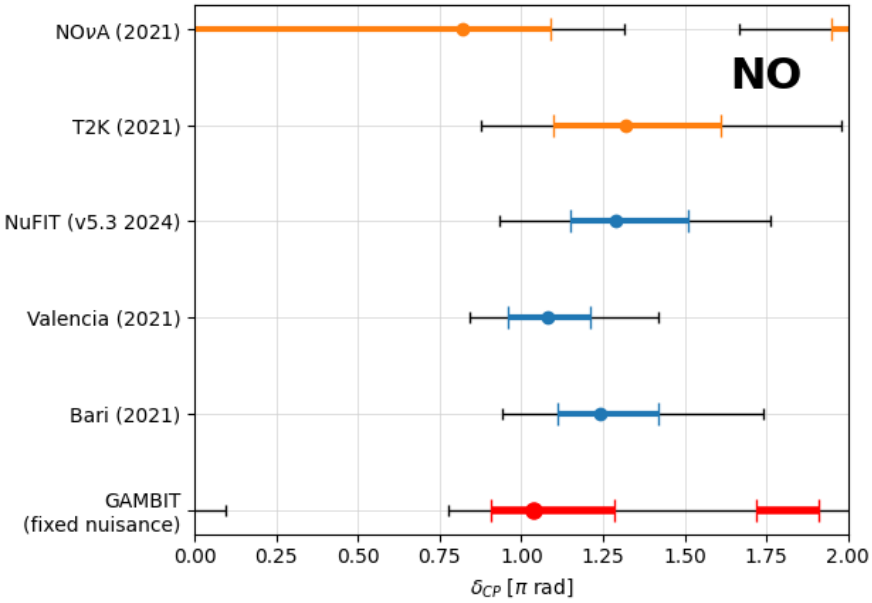


Figure 6.25: Comparison of the best-fit values, 1σ (coloured), and 2σ (black) C.L. for δ_{CP} by GAMBIT (red), the dominant experiments (orange, reference listed in Table 6.2 except T2K for which the values are sourced from [166] for the T2K-only values), and global fits (blue, [45, 119, 46, 47]), and global fits (blue, [45, 119, 46, 47]), assuming NO.

The comparison of the best-fit δ_{CP} values determined by GAMBIT and other studies is shown in Figure 6.25. All results are relatively consistent and provide strong support for $\delta_{\text{CP}} \neq 0$, except NO$\nu$A which does not rule out $\delta_{\text{CP}} = 0$. Combining the results, GAMBIT cannot reject $\delta_{\text{CP}} = 0$ at the 2σ-level. GAMBIT also sees two likelihood peaks, both of which are above the 1σ threshold and can also be seen in the $\sin^2(\theta_{23})$ vs δ_{CP} plot in Figure 6.18.

6.8 A Discussion on Data Sharing

The technique of global fit, which combines the strengths of multiple experiments to constrain the theory parameters more strongly than what each experiment can do by itself, has been demonstrated in many areas to be a powerful method. However, in many fields, including but not limited to neutrino oscillation physics, inefficiencies in data sharing can hinder the development process. Throughout the project, the limited amount of publicly accessible data has been a large challenge. It not only leads to inaccuracies in the implementations but also prevents some experiment results from being recreated altogether.

To maximise the scientific impact and to extend the importance of a research project beyond its experiment lifetime and publication, it is vital to implement mechanisms for data and analysis sharing and preservation in the experiment design so that they can be reused and reinterpreted[t] in the future generation.

In the field of neutrino physics, there are some examples of data sharing, such as the data release pages created by some collaborations [168, 169, 129]. These datasets, however, are not on their own sufficient to reproduce the publication results, partly due to the experiment's complexity and costs of management. The data, raw or reconstructed, are often inaccessible or require analysis software that is restricted to internal use. In some cases, the information from the data release is incomplete or inadequate for groups external to the original research collaborations to conduct further analyses, such as global fits that require precise and granular reconstruction and comprehensive uncertainty treatments. Conveniently, many examples and protocols already exist that neutrino experiments can learn from and adapt. For instance, the Large Hadron Collider (LHC) communities share supplementary material in databases such as 'HEPData' [170].

There are many studies on the importance of data openness. In paper [171], the authors propose a set of guidelines and recommendations to advocate for the reliable preservation of data and analyses. The concepts developed in the paper focus on the reinterpretation and recasting[u] of the experiment results, from which the field of neutrino oscillation can greatly benefit. The Reinterpretation Forum [172], driven by mainly the LHC phenomenology community consisting of an even mix of theorists and experimentalists, is another effort to ensure that the experimental results are providing continuous scientific value beyond their original purposes. Practical examples of statistical model publishing are described and discussed in detail in [173].

From the point of view of developing a neutrino oscillation global fit, and specifically for the development of the likelihood functions for accelerator and reactor neutrino experiments, there are a few key ingredients.

[t] A reinterpretation, for example, can be an update or an alternative to the theoretical modelling of neutrino interaction in an existing analysis. It can also be a study that combines the results of various analyses.

[u] This refers to the process of reproducing and possibly replacing the original parts of an analysis in a simulation.

Neutrino fluxes Neutrino fluxes for all flavours at the FD without oscillation should be released as a function of true neutrino energy. Alternatively, the combination of publishing the neutrino fluxes at the ND along with the near-to-far extrapolation matrices is also a good option.

Neutrino cross-sections Neutrino cross-sections of different processes, on different targets, and after the final tuning or reweight should be released as a function of true neutrino energy. FSIs can possibly be represented as confusion matrices quantifying how many true events of each interaction (CCQE, RES, etc.) are reconstructed to be a certain event topology.

Selection efficiencies Neutrino CC event selection efficiencies should be published as a function of neutrino true energy for all samples. It is useful to separate the efficiency into separated contributions based on the neutrino interaction types.

Reconstruction effects The reconstruction effects should be released in the form of 2D migration matrices R, where the matrix element R_{ij} is a fraction representing the portion of events in true energy bin i are reconstructed as energy bin j, for all interaction channels and for all samples.

In some cases where the above information is not practical to be released, an external group may need to develop an in-house replacement model[v] that depends on a set of nuisance parameters that need to be tuned to official data. When tuning the replacement model, it is beneficial if there exist several public neutrino energy spectra produced with different sets of neutrino oscillation parameters to characterise the reconstruction response.

In a broader scope, there remain several challenges to be solved.

ML-based algorithms As briefly described in Section 6.4, NOνA uses many ML-based reconstruction algorithms in their analyses. These trained NNs are not public and are especially difficult to reproduce in a binned analysis where event-level information is not utilised. It is therefore worth implementing a parameterised representation of the NN, or 'surrogate models' for situations where the sharing of the low-level inputs to the ML models or the models themselves are unrealistic, as proposed in [174].

Definitions and naming of parameters The importance of establishing a coherent parameter naming convention, both within an experiment and across experiments, is sometimes underestimated. An unambiguous naming system enables comparisons of experiment parameters and the possibility for consistent model combinations and global studies.

Event-level data Apart from publishing and preserving binned data, there is the possibility of releasing data at the event level, for example, the data preservation project of the Main Injector Neutrino ExpeRiment to study ν-A interactions (MINERνA) experiment [175]. Accompanying the reconstructed event data is an analysis framework built by the MINERνA collaboration, within which new analyses can

[v] A replacement model can be, for example, a Gaussian reconstruction function, similar to those used throughout the neutrino oscillation project in this thesis.

be performed. Long-term challenges such as data storage and the release of raw data are still difficult to solve.

In a reinterpretation analysis, insufficient public information can lead to an unrepresentative recreation of an experiment and distort the result. This problem can also manifest itself in the inaccuracy of parameter estimation, highlighting the importance of data sharing. Moreover, the benefits of data publication extend beyond the assurance of reproducibility. It also significantly magnifies the scientific value of an experiment, allowing the results to be re-examined and re-purposed some time beyond its original timeline.

Chapter 7

Conclusion

In this thesis, the T2K ND280 detector after the Upgrade was described and, in particular, the SuperFGD design was summarised in detail. The SuperFGD is a highly granular particle tracker made up of roughly two million 1 cm^3 plastic scintillating cubes. It was installed in the ND280 as a part of the general ND280 in 2023. It provides the ND280 suite not only an additional 2 t of active mass, but also the high spatial and energy resolutions to measure neutrino interactions at an unprecedented accuracy.

The calibration items for the SuperFGD were summarised. All aspects of the SuperFGD calibration must be robust and precise to ensure that the detector can perform to its full potential and produce accurate measurements. The charge calibration, which includes the measurement of gains and pedestals, was described. For the HG calibration, the 'multi-peak' method was implemented and was adopted as the main HG algorithm. Alternative methods were also developed as backup, and in particular, the 'autocorrelation' was described in detail. A pedestal search algorithm was also developed. The search method extrapolates multiple HG finger plots of different gains to look for the best configuration which results in the least spread in y-intercepts. A LG calibration algorithm that fits the LG ADC measurements to the HG ADC values using a linear function within the unsaturated region was developed. The ToT method was improved from the early version, which produced two sets of calibration constants. Instead, the updated ToT algorithm utilises the LG $\rightarrow$ HG calibration result to produce a continuous transition from HG to LG, lowering the number of calibration constants and reducing the fitting dependency on the saturation region between HG and LG.

A Transformer model developed in a previous study was trained using new datasets simulated by the ND280 software suite. Additional noise was added to a new dataset to emulate the defects in the calibration process. Compared to a controlled model that was trained with a dataset without the calibration noise, the one trained with a noisy dataset consistently produced results more accurately, demonstrating resilience against inaccurate calibration. The performance of reconstructing event vertices, topology, and kinematics was promising, and therefore, it is interesting to carry out further testing on the training method using real data collected by the SuperFGD.

The development of a Standard Model neutrino oscillation global fit within the GAMBIT software package was shown in the thesis. The incorporation of the NOνA, MINOS, and KamLAND likelihood functions was achieved, and the validation plots for these experiments containing GAMBIT-produced contraints on the relevant neutrino oscillation parameters and their comparisons to the respective experimental counterparts were included. Most validation results showed good agreement with the experiment observations, except those of the MINOS likelihood functions, which did not precisely recreate the experimental results due to the lack of data availability.

Combining NOνA, MINOS, and KamLAND with the other neutrino oscillation experiments implemented in GAMBIT, including SNO, Daya-Bay, Super-K, IceCube, and T2K, a validation global fit study was performed. The resulting parameter constraints are emphasised here in Table 7.1. In total, this initial study included eight experiments. All neutrino oscillation parameters were varied, but the nuisance parameters were kept constant at the best-fit points to reduce the dimension of the parameter space. While not definitive, the combined results indicate that the likelihood functions are performing as intended and yielding outcomes reasonably consistent with existing global fit studies. Some exceptions, such as the inverted mass ordering supported by the GAMBIT result, were discussed. There is also disagreement on the octant of θ_{23}, but neither is excluded at the level of 3σ. The accuracies of the measurements in this initial global study are all $< 5\%$, apart from δ_{CP}, which is still not strongly constrained by experiments. It is expected, however, that the current constraints are not fully representative and will likely alter when the nuisance parameters are taken into consideration in the final production runs.

Table 7.1: A summary table of the preliminary constraints on the neutrino oscillation parameters set by GAMBIT

Parameters	Normal ordering	Inverted ordering
$\sin^2(\theta_{12})$	$0.341^{+0.008}_{-0.008}$	$0.340^{+0.008}_{-0.008}$
$\sin^2(\theta_{13})$	$0.0217^{+0.0008}_{-0.0007}$	$0.0217^{+0.0007}_{-0.0007}$
$\sin^2(\theta_{23})$	$0.550^{+0.019}_{-0.031}$	$0.558^{+0.017}_{-0.022}$
Δm^2_{21} $[10^{-5}\mathrm{eV}^2]$	$7.66^{+0.16}_{-0.15}$	$7.66^{+0.16}_{-0.14}$
Δm^2_{32} $[10^{-3}\mathrm{eV}^2]$	$2.40^{+0.03}_{-0.03}$	$-(2.46^{+0.04}_{-0.04})$
δ_{CP} $[\pi]$	$1.04^{+0.25}_{-0.13}$	$1.52^{+0.18}_{-0.22}$
$\Delta\chi^2_{\mathrm{IO-NO}}$ (σ)		-1.7 (1.3σ)

Several challenges are to be tackled before the complete neutrino oscillation study within GAMBIT can be performed. During the trial runs, it was observed that the efficiency of exploring the full parameter space might be insufficient. This could be improved by excluding the nuisance parameters that contribute insignificantly from the scan based on a principal component analysis. More experiments, namely those which provide strong constraints on the solar and reactor sectors such as RENO and Super-K, can be implemented. Furthermore, the implemented neutrino experiments within GAMBIT can be updated.

Data sharing is crucial for advancing neutrino physics, especially as the field is progressing towards

the precision era. The complexity and diversity of experiments generate vast amounts of data that can be studied in different ways. An example can be seen in Chapter 6, where experiments of various designs were combined to create stronger constraints on neutrino oscillation measurements. This openness fosters innovation, ensures that findings are robust and reliable, and enables reproducibility, a cornerstone of scientific development. Ultimately, the benefits of data release extend beyond a few individuals and are shared by the physics community as a whole. After all, Science—born from humankind's innate curiosity about Nature—has always been a collaborative endeavour since the earliest times. And as we continue to unravel the mysteries of the subatomic world, collaboration will prove vital, accelerating the exapansion of the horizons of modern physics.

Appendix A

Additional Materials for the GAMBIT Neutrino Oscillation Project

A.1 NOνA selection efficiency functions

The FD selection efficiecy plots were directly obtained from the NOνA collaboration. Note the efficiency plot for selecting μ_ν can be found in Section 6.4. The ν_e and $\bar{\nu}_e$ include the peripheral samples.

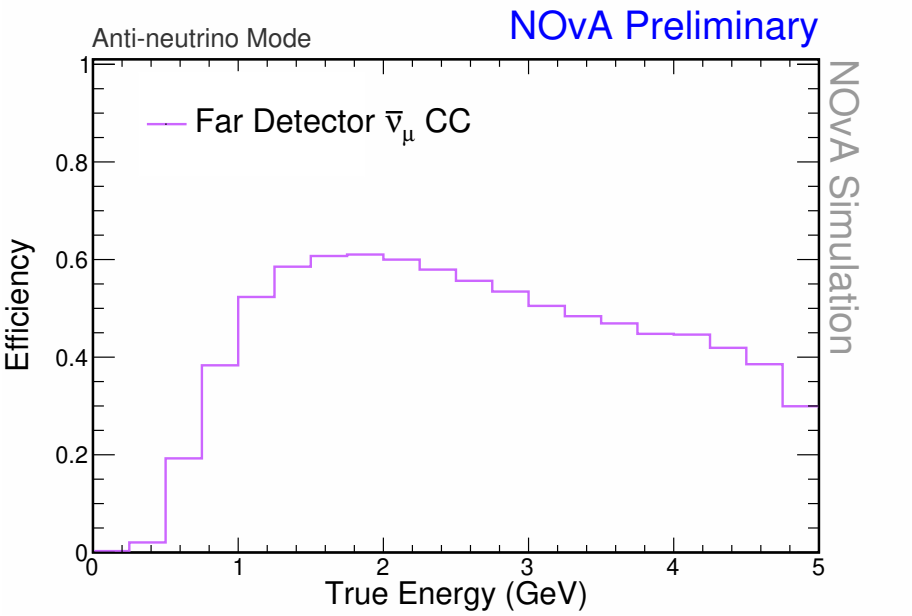


Figure A.1: The $\bar{\nu}_\mu$ selection efficiency at NOνA FD

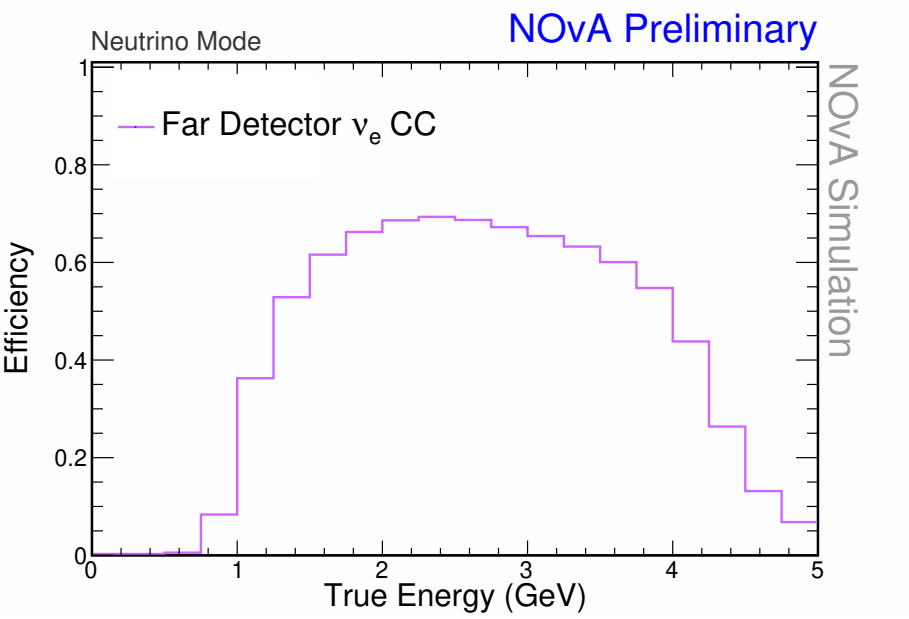


Figure A.2: The ν_e selection efficiency at NOνA FD

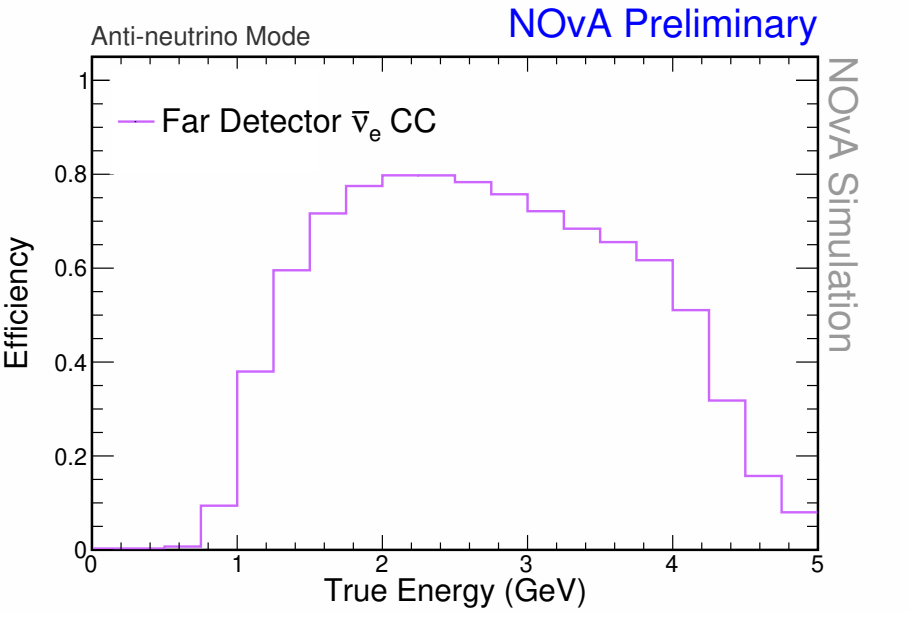


Figure A.3: The $\bar{\nu}_e$ selection efficiency at NOνA FD

Bibliography

[1] Y. Fukuda et al. "Evidence for Oscillation of Atmospheric Neutrinos". In: *Physical Review Letters* 81.8 (Aug. 1998), 1562–1567. ISSN: 1079-7114. DOI: 10.1103/physrevlett.81.1562. URL: http://dx.doi.org/10.1103/PhysRevLett.81.1562.

[2] Q. R. Ahmad et al. "Measurement of the Rate of $\nu_e + d \rightarrow p + p + e^-$ Interactions Produced by B8 Solar Neutrinos at the Sudbury Neutrino Observatory". In: *Physical Review Letters* 87.7 (July 2001). ISSN: 1079-7114. DOI: 10.1103/physrevlett.87.071301. URL: http://dx.doi.org/10.1103/PhysRevLett.87.071301.

[3] K. Abe, R. Akutsu, et al. "Constraint on the matter–antimatter symmetry-violating phase in neutrino oscillations". In: *Nature* 580.7803 (2020). [Erratum: Nature 583, E16 (2020)], pp. 339–344. DOI: 10.1038/s41586-020-2177-0. arXiv: 1910.03887 [hep-ex].

[4] B. Pontecorvo. "Inverse beta processes and nonconservation of lepton charge". In: *Zh. Eksp. Teor. Fiz.* 34 (1957), p. 247.

[5] Hyper-Kamiokande Proto-Collaboration et al. *Hyper-Kamiokande Design Report*. 2018. arXiv: 1805.04163 [physics.ins-det].

[6] R. Acciarri et al. *Long-Baseline Neutrino Facility (LBNF) and Deep Underground Neutrino Experiment (DUNE) Conceptual Design Report Volume 1: The LBNF and DUNE Projects*. 2016. arXiv: 1601.05471 [physics.ins-det].

[7] K. Abe et al. *T2K ND280 Upgrade – Technical Design Report*. 2020. arXiv: 1901.03750 [physics.ins-det].

[8] Peter Athron et al. "GAMBIT: the global and modular beyond-the-standard-model inference tool". In: *The European Physical Journal C* 77.11 (Nov. 2017). ISSN: 1434-6052. DOI: 10.1140/epjc/s10052-017-5321-8. URL: http://dx.doi.org/10.1140/epjc/s10052-017-5321-8.

[9] Peter Athron et al. "GAMBIT: the global and modular beyond-the-standard-model inference tool: Addendum for GAMBIT 1.1: Mathematica backends, SUSYHD interface and updated likelihoods". In: *The European Physical Journal C* 78.2 (Feb. 2018). ISSN: 1434-6052. DOI: 10.1140/epjc/s10052-017-5513-2. URL: http://dx.doi.org/10.1140/epjc/s10052-017-5513-2.

[10] Wolfgang Pauli. "Pauli letter collection: letter to Lise Meitner". Typed copy. URL: https://cds.cern.ch/record/83282.

[11] J. Chadwick. "The Existence of a Neutron". In: *Proc. Roy. Soc. Lond. A* 136.830 (1932), pp. 692–708. DOI: 10.1098/rspa.1932.0112.

[12] E. Fermi. "Versuch einer Theorie der β-Strahlen. I". In: *Zeitschrift für Physik* 88.3 (Mar. 1934), pp. 161–177. ISSN: 0044-3328. DOI: 10.1007/BF01351864. URL: https://doi.org/10.1007/BF01351864.

[13] F. Reines and C. L. Cowan. "Detection of the Free Neutrino". In: *Phys. Rev.* 92.3 (Nov. 1953), pp. 830–831. DOI: 10.1103/PhysRev.92.830. URL: https://link.aps.org/doi/10.1103/PhysRev.92.830.

[14] C. L. Cowan et al. "Detection of the Free Neutrino: a Confirmation". In: *Science* 124.3212 (1956), pp. 103–104. DOI: 10.1126/science.124.3212.103. eprint: https://www.science.org/doi/pdf/10.1126/science.124.3212.103. URL: https://www.science.org/doi/abs/10.1126/science.124.3212.103.

[15] G. Danby et al. "Observation of High-Energy Neutrino Reactions and the Existence of Two Kinds of Neutrinos". In: *Phys. Rev. Lett.* 9.1 (July 1962), pp. 36–44. DOI: 10.1103/PhysRevLett.9.36. URL: https://link.aps.org/doi/10.1103/PhysRevLett.9.36.

[16] K. Kodama et al. "Observation of tau neutrino interactions". In: *Physics Letters B* 504.3 (Apr. 2001), 218–224. ISSN: 0370-2693. DOI: 10.1016/s0370-2693(01)00307-0. URL: http://dx.doi.org/10.1016/S0370-2693(01)00307-0.

[17] MissMJ. *Standard Model of Elementary Particles*. Last accessed: 2024-08-30. URL: https://en.wikipedia.org/wiki/Standard_Model.

[18] John N. Bahcall and R. Davis. "Solar Neutrinos - a Scientific Puzzle". In: *Science* 191 (1976), pp. 264–267. DOI: 10.1126/science.191.4224.264.

[19] K. S. Hirata et al. "Observation of ^{8}B solar neutrinos in the Kamiokande-II detector". In: *Phys. Rev. Lett.* 63.1 (July 1989), pp. 16–19. DOI: 10.1103/PhysRevLett.63.16. URL: https://link.aps.org/doi/10.1103/PhysRevLett.63.16.

[20] P. Anselmann et al. "Solar neutrinos observed by GALLEX at Gran Sasso". In: *Physics Letters B* 285.4 (1992), pp. 376–389. ISSN: 0370-2693. DOI: https://doi.org/10.1016/0370-2693(92)91521-A. URL: https://www.sciencedirect.com/science/article/pii/037026939291521A.

[21] J.N. Abdurashitov et al. "Results from SAGE (The Russian-American gallium solar neutrino experiment)". In: *Physics Letters B* 328.1 (1994), pp. 234–248. ISSN: 0370-2693. DOI: https://doi.org/10.1016/0370-2693(94)90454-5. URL: https://www.sciencedirect.com/science/article/pii/0370269394904545.

[22] S. P. Mikheyev and A. Yu. Smirnov. "Resonance Amplification of Oscillations in Matter and Spectroscopy of Solar Neutrinos". In: *Sov. J. Nucl. Phys.* 42 (1985), pp. 913–917.

[23] L. Wolfenstein. "Neutrino oscillations in matter". In: *Phys. Rev. D* 17.9 (May 1978), pp. 2369–2374. DOI: 10.1103/PhysRevD.17.2369. URL: https://link.aps.org/doi/10.1103/PhysRevD.17.2369.

[24] K. Eguchi et al. "First Results from KamLAND: Evidence for Reactor Antineutrino Disappearance". In: *Phys. Rev. Lett.* 90.2 (Jan. 2003), p. 021802. DOI: 10.1103/PhysRevLett.90.021802. URL: https://link.aps.org/doi/10.1103/PhysRevLett.90.021802.

[25] T. J. Haines et al. "Calculation of Atmospheric Neutrino-Induced Backgrounds in a Nucleon-Decay Search". In: *Phys. Rev. Lett.* 57.16 (Oct. 1986), pp. 1986–1989. DOI: 10.1103/PhysRevLett.57.1986. URL: https://link.aps.org/doi/10.1103/PhysRevLett.57.1986.

[26] Masayuki Nakahata et al. "Atmospheric neutrino background and pion nuclear effect for KAMIOKA nucleon decay experiment". In: *Journal of the Physical Society of Japan* 55.11 (1986), pp. 3786–3805.

[27] Takaaki Kajita. "Atmospheric neutrinos". In: *New Journal of Physics* 6.1 (Dec. 2004), p. 194. DOI: 10.1088/1367-2630/6/1/194. URL: https://dx.doi.org/10.1088/1367-2630/6/1/194.

[28] B. Achkar et al. "Search for neutrino oscillations at 15, 40 and 95 meters from a nuclear power reactor at Bugey". In: *Nuclear Physics B* 434.3 (1995), pp. 503–532. ISSN: 0550-3213. DOI: https://doi.org/10.1016/0550-3213(94)00513-E. URL: https://www.sciencedirect.com/science/article/pii/055032139400513E.

[29] A. Piepke. "Final results from the Palo Verde neutrino oscillation experiment". In: *Progress in Particle and Nuclear Physics* 48.1 (2002), pp. 113–121. ISSN: 0146-6410. DOI: https://doi.org/10.1016/S0146-6410(02)00117-5. URL: https://www.sciencedirect.com/science/article/pii/S0146641002001175.

[30] M. Apollonio et al. "Search for neutrino oscillations on a long base-line at the CHOOZ nuclear power station". In: *The European Physical Journal C* 27.3 (Apr. 2003), 331–374. ISSN: 1434-6052. DOI: 10.1140/epjc/s2002-01127-9. URL: http://dx.doi.org/10.1140/epjc/s2002-01127-9.

[31] G.L. Fogli et al. "Global analysis of neutrino masses and mixing". In: *Progress in Particle and Nuclear Physics* 57.1 (2006). International Workshop of Nuclear Physics 27th course, pp. 71–78. ISSN: 0146-6410. DOI: https://doi.org/10.1016/j.ppnp.2005.12.003. URL: https://www.sciencedirect.com/science/article/pii/S014664100500150X.

[32] K. Abe et al. "Indication of Electron Neutrino Appearance from an Accelerator-Produced Off-Axis Muon Neutrino Beam". In: *Physical Review Letters* 107.4 (July 2011). ISSN: 1079-7114. DOI: 10.1103/physrevlett.107.041801. URL: http://dx.doi.org/10.1103/PhysRevLett.107.041801.

[33] P. Adamson et al. "Improved Search for Muon-Neutrino to Electron-Neutrino Oscillations in MINOS". In: *Physical Review Letters* 107.18 (Oct. 2011). ISSN: 1079-7114. DOI: 10.1103/physrevlett.107.181802. URL: http://dx.doi.org/10.1103/PhysRevLett.107.181802.

[34] G. L. Fogli et al. "Evidence of $\theta_{13} > 0$ from global neutrino data analysis". In: *Phys. Rev. D* 84.5 (Sept. 2011), p. 053007. DOI: 10.1103/PhysRevD.84.053007. URL: https://link.aps.org/doi/10.1103/PhysRevD.84.053007.

[35] Thomas Schwetz, Mariam Tórtola, and J W F Valle. "Global neutrino data and recent reactor fluxes: the status of three-flavour oscillation parameters". In: *New Journal of Physics* 13.6 (June 2011), p. 063004. ISSN: 1367-2630. DOI: 10.1088/1367-2630/13/6/063004. URL: http://dx.doi.org/10.1088/1367-2630/13/6/063004.

[36] Y. Abe et al. "Indication of Reactor $\bar{\nu}_e$ Disappearance in the Double Chooz Experiment". In: *Phys. Rev. Lett.* 108.13 (Mar. 2012), p. 131801. DOI: 10.1103/PhysRevLett.108.131801. URL: https://link.aps.org/doi/10.1103/PhysRevLett.108.131801.

[37] F. P. An et al. "Observation of Electron-Antineutrino Disappearance at Daya Bay". In: *Phys. Rev. Lett.* 108.17 (Apr. 2012), p. 171803. DOI: 10.1103/PhysRevLett.108.171803. URL: https://link.aps.org/doi/10.1103/PhysRevLett.108.171803.

[38] J. K. Ahn et al. "Observation of Reactor Electron Antineutrinos Disappearance in the RENO Experiment". In: *Physical Review Letters* 108.19 (May 2012). ISSN: 1079-7114. DOI: 10.1103/physrevlett.108.191802. URL: http://dx.doi.org/10.1103/PhysRevLett.108.191802.

[39] Evgeny Kh. Akhmedov and Joachim Kopp. "Neutrino oscillations: quantum mechanics vs. quantum field theory". In: *Journal of High Energy Physics* 2010.4 (Apr. 2010). ISSN: 1029-8479. DOI: 10.1007/jhep04(2010)008. URL: http://dx.doi.org/10.1007/JHEP04(2010)008.

[40] Z. Maki, M. Nakagawa, and S. Sakata. "Remarks on the unified model of elementary particles". In: *11th International Conference on High-energy Physics*. 1962, pp. 663–666.

[41] Charles P. Enz. "50 years ago Pauli invented the neutrino". In: *Of Matter and Spirit*, pp. 73–80. DOI: 10.1142/9789812819017_0003. eprint: https://www.worldscientific.com/doi/pdf/10.1142/9789812819017_0003. URL: https://www.worldscientific.com/doi/abs/10.1142/9789812819017_0003.

[42] M. Aker et al. *First direct neutrino-mass measurement with sub-eV sensitivity*. 2021. arXiv: 2105.08533 [hep-ex].

[43] L. Wolfenstein. "Neutrino Oscillations in Matter". In: *Phys. Rev. D* 17 (1978), pp. 2369–2374. DOI: 10.1103/PhysRevD.17.2369.

[44] S. P. Mikheyev and A. Yu. Smirnov. "Resonance Amplification of Oscillations in Matter and Spectroscopy of Solar Neutrinos". In: *Sov. J. Nucl. Phys.* 42 (1985), pp. 913–917.

[45] Ivan Esteban et al. "The fate of hints: updated global analysis of three-flavor neutrino oscillations". In: *Journal of High Energy Physics* 2020.9 (Sept. 2020). ISSN: 1029-8479. DOI: 10.1007/jhep09(2020)178. URL: http://dx.doi.org/10.1007/JHEP09(2020)178.

[46] P. F. de Salas et al. "2020 global reassessment of the neutrino oscillation picture". In: *Journal of High Energy Physics* 2021.2 (Feb. 2021). ISSN: 1029-8479. DOI: 10.1007/jhep02(2021)071. URL: http://dx.doi.org/10.1007/JHEP02(2021)071.

[47] Francesco Capozzi et al. "Unfinished fabric of the three neutrino paradigm". In: *Phys. Rev. D* 104.8 (Oct. 2021), p. 083031. DOI: 10.1103/PhysRevD.104.083031. URL: https://link.aps.org/doi/10.1103/PhysRevD.104.083031.

[48] Raul Jimenez et al. "Neutrino masses and mass hierarchy: evidence for the normal hierarchy". In: *Journal of Cosmology and Astroparticle Physics* 2022.09 (Sept. 2022), p. 006. ISSN: 1475-7516. DOI: 10.1088/1475-7516/2022/09/006. URL: http://dx.doi.org/10.1088/1475-7516/2022/09/006.

[49] Stefano Gariazzo et al. "Neutrino mass and mass ordering: no conclusive evidence for normal ordering". In: *Journal of Cosmology and Astroparticle Physics* 2022.10 (Oct. 2022), p. 010. ISSN: 1475-7516. DOI: 10.1088/1475-7516/2022/10/010. URL: http://dx.doi.org/10.1088/1475-7516/2022/10/010.

[50] Angel Abusleme et al. "JUNO physics and detector". In: *Prog. Part. Nucl. Phys.* 123 (2022), p. 103927. DOI: 10.1016/j.ppnp.2021.103927. arXiv: 2104.02565 [hep-ex].

[51] Sandhya Choubey, Monojit Ghosh, and Deepak Raikwal. "Neutrino mass ordering: Circumventing the challenges using synergy between T2HK and JUNO". In: *Physical Review D* 106.11 (Dec. 2022). ISSN: 2470-0029. DOI: 10.1103/physrevd.106.115013. URL: http://dx.doi.org/10.1103/PhysRevD.106.115013.

[52] R. Arnold et al. "Probing new physics models of neutrinoless double beta decay with SuperNEMO". In: *The European Physical Journal C* 70.4 (Nov. 2010), 927–943. ISSN: 1434-6052. DOI: 10.1140/epjc/s10052-010-1481-5. URL: http://dx.doi.org/10.1140/epjc/s10052-010-1481-5.

[53] N. Abgrall et al. "The large enriched germanium experiment for neutrinoless double beta decay (LEGEND)". In: *AIP Conference Proceedings*. Author(s), 2017. DOI: 10.1063/1.5007652. URL: http://dx.doi.org/10.1063/1.5007652.

[54] V. Albanese et al. "The SNO+ experiment". In: *Journal of Instrumentation* 16.08 (Aug. 2021), P08059. ISSN: 1748-0221. DOI: 10.1088/1748-0221/16/08/p08059. URL: http://dx.doi.org/10.1088/1748-0221/16/08/P08059.

[55] K. Abe et al. "The T2K experiment". In: *Nuclear Instruments and Methods in Physics Research Section A: Accelerators, Spectrometers, Detectors and Associated Equipment* 659.1 (Dec. 2011), 106–135. ISSN: 0168-9002. DOI: 10.1016/j.nima.2011.06.067. URL: http://dx.doi.org/10.1016/j.nima.2011.06.067.

[56] K. Abe et al. "Indication of Electron Neutrino Appearance from an Accelerator-Produced Off-Axis Muon Neutrino Beam". In: *Physical Review Letters* 107.4 (July 2011). ISSN: 1079-7114. DOI: 10.1103/physrevlett.107.041801. URL: http://dx.doi.org/10.1103/PhysRevLett.107.041801.

[57] K. Abe et al. "Updated T2K measurements of muon neutrino and antineutrino disappearance using 3.6×1021 protons on target". In: *Phys. Rev. D* 108.7 (2023), p. 072011. DOI: 10.1103/PhysRevD.108.072011. arXiv: 2305.09916 [hep-ex].

[58] K. Abe et al. "Measurement of the inclusive ν_μ charged current cross section on carbon in the near detector of the T2K experiment". In: *Phys. Rev. D* 87 (9 May 2013), p. 092003. DOI: 10.1103/PhysRevD.87.092003. URL: https://link.aps.org/doi/10.1103/PhysRevD.87.092003.

[59] K. Abe et al. "Measurements of neutrino oscillation parameters from the T2K experiment using 3.6×10^{21} protons on target". In: *The European Physical Journal C* 83.9 (Sept. 2023). ISSN: 1434-6052. DOI: 10.1140/epjc/s10052-023-11819-x. URL: http://dx.doi.org/10.1140/epjc/s10052-023-11819-x.

[60] K. Abe et al. "Measurements of neutrino oscillation in appearance and disappearance channels by the T2K experiment with 6.6×10^{20} protons on target". In: *Physical Review D* 91.7 (Apr. 2015). ISSN: 1550-2368. DOI: 10.1103/physrevd.91.072010. URL: http://dx.doi.org/10.1103/PhysRevD.91.072010.

[61] K. Abe et al. "Improved constraints on neutrino mixing from the T2K experiment with 3.13×10^{21} protons on target". In: *Physical Review D* 103.11 (June 2021). ISSN: 2470-0029. DOI: 10.1103/physrevd.103.112008. URL: http://dx.doi.org/10.1103/PhysRevD.103.112008.

[62] K. Abe et al. "T2K neutrino flux prediction". In: *Phys. Rev. D* 87.1 (Jan. 2013), p. 012001. DOI: 10.1103/PhysRevD.87.012001. URL: https://link.aps.org/doi/10.1103/PhysRevD.87.012001.

[63] K. Abe et al. "First T2K measurement of transverse kinematic imbalance in the muon-neutrino charged-current single-π^+ production channel containing at least one proton". In: *Physical Review D* 103.11 (June 2021). ISSN: 2470-0029. DOI: 10.1103/physrevd.103.112009. URL: http://dx.doi.org/10.1103/PhysRevD.103.112009.

[64] K. Abe et al. "Simultaneous measurement of the muon neutrino charged-current cross section on oxygen and carbon without pions in the final state at T2K". In: *Physical Review D* 101.11 (June 2020). ISSN: 2470-0029. DOI: 10.1103/physrevd.101.112004. URL: http://dx.doi.org/10.1103/PhysRevD.101.112004.

[65] K. Abe et al. "First measurement of the charged current $\bar{\nu}_\mu$ double differential cross section on a water target without pions in the final state". In: *Physical Review D* 102.1 (July 2020). ISSN: 2470-0029. DOI: 10.1103/physrevd.102.012007. URL: http://dx.doi.org/10.1103/PhysRevD.102.012007.

[66] K. Abe et al. "Search for heavy neutrinos with the T2K near detector ND280". In: *Physical Review D* 100.5 (Sept. 2019). ISSN: 2470-0029. DOI: 10.1103/physrevd.100.052006. URL: http://dx.doi.org/10.1103/PhysRevD.100.052006.

[67] S. Assylbekov et al. "The T2K ND280 off-axis pi–zero detector". In: *Nuclear Instruments and Methods in Physics Research Section A: Accelerators, Spectrometers, Detectors and Associated Equipment* 686 (Sept. 2012), 48–63. ISSN: 0168-9002. DOI: 10.1016/j.nima.2012.05.028. URL: http://dx.doi.org/10.1016/j.nima.2012.05.028.

[68] S. Aoki et al. "The T2K Side Muon Range Detector (SMRD)". In: *Nuclear Instruments and Methods in Physics Research Section A: Accelerators, Spectrometers, Detectors and Associated Equipment* 698 (Jan. 2013), 135–146. ISSN: 0168-9002. DOI: 10.1016/j.nima.2012.10.001. URL: http://dx.doi.org/10.1016/j.nima.2012.10.001.

[69] P.-A. Amaudruz et al. "The T2K fine-grained detectors". In: *Nuclear Instruments and Methods in Physics Research Section A: Accelerators, Spectrometers, Detectors and Associated Equipment* 696 (Dec. 2012), 1–31. ISSN: 0168-9002. DOI: 10.1016/j.nima.2012.08.020. URL: http://dx.doi.org/10.1016/j.nima.2012.08.020.

[70] T2K ND280 TPC collaboration. *Time Projection Chambers for the T2K Near Detectors*. 2010. arXiv: 1012.0865 [physics.ins-det]. URL: https://arxiv.org/abs/1012.0865.

[71] T2K ND280 TPC collaboration. *Time Projection Chambers for the T2K Near Detectors*. 2010. arXiv: 1012.0865 [physics.ins-det]. URL: https://arxiv.org/abs/1012.0865.

[72] D Allan et al. "The electromagnetic calorimeter for the T2K near detector ND280". In: *Journal of Instrumentation* 8.10 (Oct. 2013), P10019–P10019. ISSN: 1748-0221. DOI: 10.1088/1748-0221/8/10/p10019. URL: http://dx.doi.org/10.1088/1748-0221/8/10/P10019.

[73] D. Attie et al. *Characterization of Charge Spreading and Gain of Encapsulated Resistive Micromegas Detectors for the Upgrade of the T2K Near Detector Time Projection Chambers*. 2023. arXiv: 2303.04481 [physics.ins-det]. URL: https://arxiv.org/abs/2303.04481.

[74] A. Korzenev et al. "A 4π time-of-flight detector for the ND280/T2K upgrade". In: *Journal of Instrumentation* 17.01 (Jan. 2022), P01016. ISSN: 1748-0221. DOI: 10.1088/1748-0221/17/01/p01016. URL: http://dx.doi.org/10.1088/1748-0221/17/01/P01016.

[75] A. Korzenev et al. "A 4π time-of-flight detector for the ND280/T2K upgrade". In: *Journal of Instrumentation* 17.01 (Jan. 2022), P01016. ISSN: 1748-0221. DOI: 10.1088/1748-0221/17/01/p01016. URL: http://dx.doi.org/10.1088/1748-0221/17/01/P01016.

[76] M. Koshiba. "22-KTON WATER CHERENKOV DETECTOR (JACK)". In: *International Colloquium on Baryon Nonconservation (ICOBAN '84)*. 1985.

[77] K. Hirata et al. "Observation of a neutrino burst from the supernova SN1987A". In: *Phys. Rev. Lett.* 58 (14 Apr. 1987), pp. 1490–1493. DOI: 10.1103/PhysRevLett.58.1490. URL: https://link.aps.org/doi/10.1103/PhysRevLett.58.1490.

[78] K. Abe et al. "First gadolinium loading to Super-Kamiokande". In: *Nuclear Instruments and Methods in Physics Research Section A: Accelerators, Spectrometers, Detectors and Associated Equipment* 1027 (Mar. 2022), p. 166248. ISSN: 0168-9002. DOI: 10.1016/j.nima.2021.166248. URL: http://dx.doi.org/10.1016/j.nima.2021.166248.

[79] K. Abe et al. "Second gadolinium loading to Super-Kamiokande". In: *Nuclear Instruments and Methods in Physics Research Section A: Accelerators, Spectrometers, Detectors and Associated Equipment* 1065 (Aug. 2024), p. 169480. ISSN: 0168-9002. DOI: 10.1016/j.nima.2024.169480. URL: http://dx.doi.org/10.1016/j.nima.2024.169480.

[80] Y. Itow et al. *The JHF-Kamioka neutrino project*. 2001. arXiv: hep-ex/0106019 [hep-ex]. URL: https://arxiv.org/abs/hep-ex/0106019.

[81] Kamioka Observatory, ICRR (Institute for Cosmic Ray Research), The University of Tokyo. *The Super-K Detector*. Last access: 2024-08-31. URL: https://www-sk.icrr.u-tokyo.ac.jp/en/sk/experience/gallery/.

[82] M Jiang et al. "Atmospheric neutrino oscillation analysis with improved event reconstruction in Super-Kamiokande IV". In: *Progress of Theoretical and Experimental Physics* 2019.5 (May 2019), 053F01. ISSN: 2050-3911. DOI: 10.1093/ptep/ptz015. eprint: https://academic.oup.com/ptep/article-pdf/2019/5/053F01/28638877/ptz015.pdf. URL: https://doi.org/10.1093/ptep/ptz015.

[83] C. Jarlskog. "A Basis Independent Formulation of the Connection Between Quark Mass Matrices, CP Violation and Experiment". In: *Z. Phys. C* 29 (1985), pp. 491–497. DOI: 10.1007/BF01565198.

[84] S Fedotov et al. "Scintillator cubes for 3D neutrino detector SuperFGD". In: *Journal of Physics: Conference Series* 2374.1 (Nov. 2022), p. 012106. ISSN: 1742-6596. DOI: 10.1088/1742-6596/2374/1/012106. URL: http://dx.doi.org/10.1088/1742-6596/2374/1/012106.

[85] Ltd Kuraray Co. *Plastic Scintillating Fibers*. Last accessed: 2024-07-25. URL: https://www.kuraray.co.jp/uploads/5a717515df6f5/PR0150_psf01.pdf.

[86] Hamamatsu Photonics. *Hamamatsu S13360 Series*. Last accessed: 2024-07-25. URL: https://www.hamamatsu.com/content/dam/hamamatsu-photonics/sites/documents/99_SALES_LIBRARY/ssd/s13360_series_kapd1052e.pdf.

[87] Claudio (LPNHE) Giganti and Thorsten (IFAE) Lux. *NP07: ND280 Upgrade project - SPSC Repor*. Tech. rep. Geneva: CERN, 2022. URL: https://cds.cern.ch/record/2805467.

[88] Super-FGD Japan group and Super-FGD electronics group. *T2K ND280 Upgrade Document: SuperFGD Assembly and Integration in Japan*.

[89] Hamamatsu Photonics. *MPPC Technical Note*. Last accessed: 2024-07-25. URL: https://www.hamamatsu.com/content/dam/hamamatsu-photonics/sites/documents/99_SALES_LIBRARY/ssd/mppc_kapd9008e.pdf.

[90] A. Blondel et al. "The SuperFGD Prototype charged particle beam tests". In: *Journal of Instrumentation* 15.12 (Dec. 2020), P12003–P12003. ISSN: 1748-0221. DOI: 10.1088/1748-0221/15/12/p12003. URL: http://dx.doi.org/10.1088/1748-0221/15/12/P12003.

[91] T Arihara et al. "Development of the in-situ calibration system using leds and light guide plates for the SuperFGD". In: *Journal of Physics: Conference Series* 2374.1 (Nov. 2022), p. 012118. DOI: 10.1088/1742-6596/2374/1/012118.

[92] Takuji Arihara. *(T2K internal talk) optics part of calibration system*. Nov. 2020.

[93] Miroslav Morháč et al. "Background elimination methods for multidimensional coincidence γ-ray spectra". In: *Nuclear Instruments and Methods in Physics Research Section A: Accelerators, Spectrometers, Detectors and Associated Equipment* 401.1 (1997), pp. 113–132. ISSN: 0168-9002. DOI: https://doi.org/10.1016/S0168-9002(97)01023-1. URL: https://www.sciencedirect.com/science/article/pii/S0168900297010231.

[94] Miroslav Morháč et al. "Efficient one- and two-dimensional gold deconvolution and its application to γ-ray spectra decomposition". In: *Nuclear Instruments and Methods in Physics Research Section A: Accelerators, Spectrometers, Detectors and Associated Equipment* 401.2 (1997), pp. 385–408. ISSN: 0168-9002. DOI: https://doi.org/10.1016/S0168-9002(97)01058-9. URL: https://www.sciencedirect.com/science/article/pii/S0168900297010589.

[95] Miroslav Morháč et al. "Identification of peaks in multidimensional coincidence γ-ray spectra". In: *Nuclear Instruments and Methods in Physics Research Section A: Accelerators, Spectrometers, Detectors and Associated Equipment* 443.1 (2000), pp. 108–125. ISSN: 0168-9002. DOI: https://doi.org/10.1016/S0168-9002(99)01005-0. URL: https://www.sciencedirect.com/science/article/pii/S0168900299010050.

[96] Z.K. Silagadze. "A new algorithm for automatic photopeak searches". In: *Nuclear Instruments and Methods in Physics Research Section A: Accelerators, Spectrometers, Detectors and Associated Equipment* 376.3 (1996), pp. 451–454. ISSN: 0168-9002. DOI: https://doi.org/10.1016/0168-9002(96)00230-6. URL: https://www.sciencedirect.com/science/article/pii/0168900296002306.

[97] Lorenzo Giannessi. *(T2K summer workshop) Super-FGD performance and simulation.* July 2024. URL: https://indico.cern.ch/event/1401202/contributions/6041560/.

[98] J. B. Birks. "Scintillations from Organic Crystals: Specific Fluorescence and Relative Response to Different Radiations". In: *Proc. Phys. Soc. A* 64 (1951), pp. 874–877. DOI: 10.1088/0370-1298/64/10/303.

[99] Yann LeCun, Y. Bengio, and Geoffrey Hinton. "Deep Learning". In: *Nature* 521 (May 2015), pp. 436–44. DOI: 10.1038/nature14539.

[100] Ashish Vaswani et al. *Attention Is All You Need.* 2023. arXiv: 1706.03762 [cs.CL]. URL: https://arxiv.org/abs/1706.03762.

[101] Partha Pratim Ray. "ChatGPT: A comprehensive review on background, applications, key challenges, bias, ethics, limitations and future scope". In: *Internet of Things and Cyber-Physical Systems* 3 (2023), pp. 121–154. ISSN: 2667-3452. DOI: https://doi.org/10.1016/j.iotcps.2023.04.003. URL: https://www.sciencedirect.com/science/article/pii/S266734522300024X.

[102] Jacob Devlin et al. *BERT: Pre-training of Deep Bidirectional Transformers for Language Understanding.* 2019. arXiv: 1810.04805 [cs.CL]. URL: https://arxiv.org/abs/1810.04805.

[103] Dzmitry Bahdanau, Kyunghyun Cho, and Yoshua Bengio. *Neural Machine Translation by Jointly Learning to Align and Translate.* 2016. arXiv: 1409.0473 [cs.CL]. URL: https://arxiv.org/abs/1409.0473.

[104] Saidul Islam et al. *A Comprehensive Survey on Applications of Transformers for Deep Learning Tasks.* 2023. arXiv: 2306.07303 [cs.LG]. URL: https://arxiv.org/abs/2306.07303.

[105] José Maurício, Inês Domingues, and Jorge Bernardino. "Comparing Vision Transformers and Convolutional Neural Networks for Image Classification: A Literature Review". In: *Applied Sciences* 13.9 (2023). ISSN: 2076-3417. DOI: 10.3390/app13095521. URL: https://www.mdpi.com/2076-3417/13/9/5521.

[106] Shigeki Karita et al. "A Comparative Study on Transformer vs RNN in Speech Applications". In: *2019 IEEE Automatic Speech Recognition and Understanding Workshop (ASRU)*. IEEE, Dec. 2019. DOI: 10.1109/asru46091.2019.9003750. URL: http://dx.doi.org/10.1109/ASRU46091.2019.9003750.

[107] Saúl Alonso-Monsalve et al. "Deep-learning-based decomposition of overlapping-sparse images: application at the vertex of neutrino interactions". In: (Oct. 2023). arXiv: 2310.19695 [cs.CV].

[108] Yang You et al. *Large Batch Optimization for Deep Learning: Training BERT in 76 minutes*. 2020. arXiv: 1904.00962 [cs.LG]. URL: https://arxiv.org/abs/1904.00962.

[109] Yang You, Igor Gitman, and Boris Ginsburg. *Large Batch Training of Convolutional Networks*. 2017. arXiv: 1708.03888 [cs.CV]. URL: https://arxiv.org/abs/1708.03888.

[110] Diederik P. Kingma and Jimmy Ba. *Adam: A Method for Stochastic Optimization*. 2017. arXiv: 1412.6980 [cs.LG]. URL: https://arxiv.org/abs/1412.6980.

[111] Ian J. Goodfellow et al. *Generative Adversarial Networks*. 2014. arXiv: 1406.2661 [stat.ML]. URL: https://arxiv.org/abs/1406.2661.

[112] S. Agostinelli et al. "Geant4—a simulation toolkit". In: *Nuclear Instruments and Methods in Physics Research Section A: Accelerators, Spectrometers, Detectors and Associated Equipment* 506.3 (2003), pp. 250–303. ISSN: 0168-9002. DOI: https://doi.org/10.1016/S0168-9002(03)01368-8.

[113] Yoshi Uchida. *ND280 software processing flowchart*. 2009.

[114] M. A. Acero et al. "Improved measurement of neutrino oscillation parameters by the NOvA experiment". In: *Phys. Rev. D* 106.3 (Aug. 2022), p. 032004. DOI: 10.1103/PhysRevD.106.032004. URL: https://link.aps.org/doi/10.1103/PhysRevD.106.032004.

[115] Connor Shorten and Taghi M. Khoshgoftaar. "A survey on Image Data Augmentation for Deep Learning". In: *Journal of Big Data* 6 (2019), pp. 1–48. URL: https://api.semanticscholar.org/CorpusID:195811894.

[116] Philip Hamacher-Baumann, Xianguo Lu, and Justo Martín-Albo. "Neutrino-hydrogen interactions with a high-pressure time projection chamber". In: *Phys. Rev. D* 102 (3 2020), p. 033005. DOI: 10.1103/PhysRevD.102.033005. URL: https://link.aps.org/doi/10.1103/PhysRevD.102.033005.

[117] R. L. Workman and Others. "Review of Particle Physics". In: *PTEP* 2022 (2022), p. 083C01. DOI: 10.1093/ptep/ptac097.

[118] Gian Luigi Fogli, E. Lisi, and D. Montanino. "A comprehensive analysis of solar, atmospheric, accelerator and reactor neutrino experiments in a hierarchical three generation scheme". In: *Phys. Rev. D* 49 (1994), pp. 3626–3642. DOI: 10.1103/PhysRevD.49.3626.

[119] NuFIT Collaboration. *v5.3: Three-neutrino fit based on data available in March 2024*. Last accessed: 2024-08-10. 2024. URL: http://www.nu-fit.org/?q=node/278.

[120] Peter Athron et al. "Status of the scalar singlet dark matter model". In: *The European Physical Journal C* 77.8 (Aug. 2017). ISSN: 1434-6052. DOI: 10.1140/epjc/s10052-017-5113-1. URL: http://dx.doi.org/10.1140/epjc/s10052-017-5113-1.

[121] Peter Athron et al. "Global fits of GUT-scale SUSY models with GAMBIT". In: *The European Physical Journal C* 77.12 (Dec. 2017). ISSN: 1434-6052. DOI: 10.1140/epjc/s10052-017-5167-0. URL: http://dx.doi.org/10.1140/epjc/s10052-017-5167-0.

[122] Peter Athron et al. "A global fit of the MSSM with GAMBIT". In: *The European Physical Journal C* 77.12 (Dec. 2017). ISSN: 1434-6052. DOI: 10.1140/epjc/s10052-017-5196-8. URL: http://dx.doi.org/10.1140/epjc/s10052-017-5196-8.

[123] Patrick Stöcker et al. "Strengthening the bound on the mass of the lightest neutrino with terrestrial and cosmological experiments". In: *Physical Review D* 103.12 (June 2021). ISSN: 2470-0029. DOI: 10.1103/physrevd.103.123508. URL: http://dx.doi.org/10.1103/PhysRevD.103.123508.

[124] Marcin Chrzaszcz et al. "A Frequentist analysis of three right-handed neutrinos with GAMBIT". In: *The European Physical Journal C* 80.6 (June 2020). ISSN: 1434-6052. DOI: 10.1140/epjc/s10052-020-8073-9. URL: http://dx.doi.org/10.1140/epjc/s10052-020-8073-9.

[125] Wilf Shorrock. "Determining the basic properties of a new particle detector concept for the T2K experiment and implementing the T2K calculation for a three-neutrino global fit with GAMBIT". PhD thesis. Imperial College London, 2022.

[126] B. Aharmim et al. "Combined analysis of all three phases of solar neutrino data from the Sudbury Neutrino Observatory". In: *Physical Review C* 88.2 (Aug. 2013). ISSN: 1089-490X. DOI: 10.1103/physrevc.88.025501. URL: http://dx.doi.org/10.1103/PhysRevC.88.025501.

[127] D. Adey et al. "Measurement of the Electron Antineutrino Oscillation with 1958 Days of Operation at Daya Bay". In: *Physical Review Letters* 121.24 (Dec. 2018). ISSN: 1079-7114. DOI: 10.1103/physrevlett.121.241805. URL: http://dx.doi.org/10.1103/PhysRevLett.121.241805.

[128] A. Gando et al. "Constraints on θ_{13} from a three-flavor oscillation analysis of reactor antineutrinos at KamLAND". In: *Physical Review D* 83.5 (Mar. 2011). ISSN: 1550-2368. DOI: 10.1103/physrevd.83.052002. URL: http://dx.doi.org/10.1103/PhysRevD.83.052002.

[129] KamLAND Collaboration. *The KamLAND data release page*. Last accessed: 2024-08-25. URL: https://www.awa.tohoku.ac.jp/KamLAND/4th_result_data_release/4th_result_data_release.html.

[130] K. Abe et al. "Atmospheric neutrino oscillation analysis with external constraints in Super-Kamiokande I-IV". In: *Physical Review D* 97.7 (Apr. 2018). ISSN: 2470-0029. DOI: 10.1103/physrevd.97.072001. URL: http://dx.doi.org/10.1103/PhysRevD.97.072001.

[131] M. G. Aartsen et al. "Measurement of Atmospheric Neutrino Oscillations at 6–56 GeV with IceCube DeepCore". In: *Phys. Rev. Lett.* 120 (7 2018), p. 071801. DOI: 10.1103/PhysRevLett.120.071801. URL: https://link.aps.org/doi/10.1103/PhysRevLett.120.071801.

[132] The corresponding NOvA data release can be found here: https://publicdocs.fnal.gov/cgi-bin/ShowDocument?docid=17.

[133] P. Adamson et al. "Measurement of Neutrino and Antineutrino Oscillations Using Beam and Atmospheric Data in MINOS". In: *Physical Review Letters* 110.25 (June 2013). ISSN: 1079-7114. DOI: 10.1103/physrevlett.110.251801. URL: http://dx.doi.org/10.1103/PhysRevLett.110.251801.

[134] Gregory D. Martinez et al. "Comparison of statistical sampling methods with ScannerBit, the GAMBIT scanning module". In: *The European Physical Journal C* 77.11 (Nov. 2017). ISSN: 1434-6052. DOI: 10.1140/epjc/s10052-017-5274-y. URL: http://dx.doi.org/10.1140/epjc/s10052-017-5274-y.

[135] Rainer Storn and Kenneth Price. "Differential Evolution - A Simple and Efficient Heuristic for Global Optimization over Continuous Spaces". In: *Journal of Global Optimization* 11 (Jan. 1997), pp. 341–359. DOI: 10.1023/A:1008202821328.

[136] Swagatam Das and Ponnuthurai Nagaratnam Suganthan. "Differential Evolution: A Survey of the State-of-the-Art". In: *IEEE Transactions on Evolutionary Computation* 15.1 (2011), pp. 4–31. DOI: 10.1109/TEVC.2010.2059031.

[137] D. S. Ayres et al. *The NOvA Technical Design Report*. Tech. rep. Oct. 2007. DOI: 10.2172/935497.

[138] P. Adamson et al. "The NuMI neutrino beam". In: *Nuclear Instruments and Methods in Physics Research Section A: Accelerators, Spectrometers, Detectors and Associated Equipment* 806 (2016), pp. 279–306. ISSN: 0168-9002. DOI: https://doi.org/10.1016/j.nima.2015.08.063. URL: https://www.sciencedirect.com/science/article/pii/S016890021501027X.

[139] Fermilab. *The 14,000-ton NOvA neutrino detector at Fermilab*. Last accessed: 2024-08-07. URL: https://nusoft.fnal.gov/nova/public/img/15-0166-16.jpg.

[140] Fermilab Reidar Hahn. *The 300-ton NOvA neutrino detector at Fermilab*. Last accessed: 2024-08-07. URL: https://vms.fnal.gov/asset/detail?recid=1937180.

[141] Nitish Nayak. "A Joint Measurement of ν_μ-Disappearance and ν_e-Appearance in the NuMI beam using the NOvA Experiment". PhD thesis. University of California, Irvine, 2021.

[142] K. Abe et al. "Updated T2K measurements of muon neutrino and antineutrino disappearance using 3.6×10^{21} protons on target". In: *Phys. Rev. D* 108.7 (Oct. 2023), p. 072011. DOI: 10.1103/PhysRevD.108.072011. URL: https://link.aps.org/doi/10.1103/PhysRevD.108.072011.

[143] Ivan Esteban et al. "Global analysis of three-flavour neutrino oscillations: synergies and tensions in the determination of θ_{23}, δ_{CP}, and the mass ordering". In: *Journal of High Energy Physics* 2019.1 (Jan. 2019). ISSN: 1029-8479. DOI: 10.1007/jhep01(2019)106. URL: http://dx.doi.org/10.1007/JHEP01(2019)106.

[144] C. Andreopoulos et al. "The GENIE neutrino Monte Carlo generator". In: *Nuclear Instruments and Methods in Physics Research Section A: Accelerators, Spectrometers, Detectors and Associated Equipment* 614.1 (Feb. 2010), 87–104. ISSN: 0168-9002. DOI: 10.1016/j.nima.2009.12.009. URL: http://dx.doi.org/10.1016/j.nima.2009.12.009.

[145] Costas Andreopoulos et al. *The GENIE Neutrino Monte Carlo Generator: Physics and User Manual*. 2015. arXiv: 1510.05494 [hep-ph]. URL: https://arxiv.org/abs/1510.05494.

[146] M. A. Acero et al. "Adjusting neutrino interaction models and evaluating uncertainties using NOvA near detector data". In: *The European Physical Journal C* 80.12 (Dec. 2020). ISSN: 1434-6052. DOI: 10.1140/epjc/s10052-020-08577-5. URL: http://dx.doi.org/10.1140/epjc/s10052-020-08577-5.

[147] Roger Wendell. *Prob3++ Software Repository*. Last accessed: 2024-08-07. URL: https://github.com/rogerwendell/Prob3plusplus.

[148] V. Barger et al. "Matter effects on three-neutrino oscillations". In: *Phys. Rev. D* 22.11 (Dec. 1980), pp. 2718–2726. DOI: 10.1103/PhysRevD.22.2718. URL: https://link.aps.org/doi/10.1103/PhysRevD.22.2718.

[149] C Patrignani et al. "Review of Particle Physics, 2016-2017". In: *Chin. Phys. C* 40.10 (2016). Version 2017 update, p. 100001. DOI: 10.1088/1674-1137/40/10/100001. URL: https://cds.cern.ch/record/2241948.

[150] I. Ambats et al. *The MINOS Detectors Technical Design Report*. Tech. rep. Oct. 1998. DOI: 10.2172/1861363.

[151] MINOS Collaboration. *MINOS far detector*. Last accessed: 2024-08-10. URL: https://history.fnal.gov/historical/experiments/minos_sheds_light.html.

[152] Justin Evans. *The MINOS experiment: results and prospects*. 2013. arXiv: 1307.0721 [hep-ex]. URL: https://arxiv.org/abs/1307.0721.

[153] Ashley Timmons. *The Results of MINOS and the Future with MINOS+*. 2015. arXiv: 1511.06178 [hep-ex]. URL: https://arxiv.org/abs/1511.06178.

[154] P. Adamson et al. "Combined Analysis of ν_μ Disappearance and $\nu_\mu \to \nu_e$ Appearance in MINOS Using Accelerator and Atmospheric Neutrinos". In: *Physical Review Letters* 112.19 (May 2014). ISSN: 1079-7114. DOI: 10.1103/physrevlett.112.191801. URL: http://dx.doi.org/10.1103/PhysRevLett.112.191801.

[155] Jiajie Ling. "A study of muon neutrino disappearance in the MINOS detectors and the NuMI beam". PhD thesis. 2010. DOI: 10.2172/983987.

[156] U.S. KamLAND Collaboration. *Proposal for US Participation in KamLAND*. 1999. URL: http://kamland.stanford.edu/Technical/KamLAND.US.Proposal.pdf.

[157] Th. A. Mueller et al. "Improved predictions of reactor antineutrino spectra". In: *Phys. Rev. C* 83.5 (May 2011), p. 054615. DOI: 10.1103/PhysRevC.83.054615. URL: https://link.aps.org/doi/10.1103/PhysRevC.83.054615.

[158] Japan Nuclear Energy Safety Organization. "Operational status of nuclear facilities in Japan". In: *Operational Status of Nuclear Facilities in Japan* (2004-2013). One edition per year except 2007 which was missing. ISSN: 1347-0493.

[159] Japan Atomic Industrial Forum inc. *Operational Record of Nuclear Power Plants in Japan*. Last accessed: 2024-03-08. URL: https://www.jaif.or.jp/category/npp.

[160] P. Vogel and J. F. Beacom. "The angular distribution of the reaction $\bar{\nu}_e + p \to e^+ + n$". In: *Physical Review D* 60.5 (July 1999). ISSN: 1089-4918. DOI: 10.1103/physrevd.60.053003. URL: http://dx.doi.org/10.1103/PhysRevD.60.053003.

[161] Núria Vinyoles et al. "A New Generation of Standard Solar Models". In: *The Astrophysical Journal* 835.2 (Jan. 2017), p. 202. ISSN: 1538-4357. DOI: 10.3847/1538-4357/835/2/202. URL: http://dx.doi.org/10.3847/1538-4357/835/2/202.

[162] Martin Asplund et al. "The Chemical Composition of the Sun". In: *Annual Review of Astronomy and Astrophysics* 47.1 (Sept. 2009), 481–522. ISSN: 1545-4282. DOI: 10.1146/annurev.astro.46.060407.145222. URL: http://dx.doi.org/10.1146/annurev.astro.46.060407.145222.

[163] N. Grevesse and A. J. Sauval. "Standard Solar Composition". In: *Space Science Reviews* 85 (May 1998), pp. 161–174. DOI: 10.1023/A:1005161325181.

[164] John N. Bahcall, Aldo M. Serenelli, and Sarbani Basu. "New Solar Opacities, Abundances, Helioseismology, and Neutrino Fluxes". In: *The Astrophysical Journal* 621.1 (Jan. 2005), L85–L88. ISSN: 1538-4357. DOI: 10.1086/428929. URL: http://dx.doi.org/10.1086/428929.

[165] K. Abe et al. "Solar neutrino measurements using the full data period of Super-Kamiokande-IV". In: *Physical Review D* 109.9 (May 2024). ISSN: 2470-0029. DOI: 10.1103/physrevd.109.092001. URL: http://dx.doi.org/10.1103/PhysRevD.109.092001.

[166] Artur Adam Sztuc. "Standard and non-standard neutrino-antineutrino oscillation analyses and event reconstruction studies using Markov chain Monte Carlo methods at T2K". PhD thesis. Imperial Coll., London, 2020. DOI: 10.25560/91769.

[167] T. Wester et al. "Atmospheric neutrino oscillation analysis with neutron tagging and an expanded fiducial volume in Super-Kamiokande I–V". In: *Physical Review D* 109.7 (Apr. 2024). ISSN: 2470-0029. DOI: 10.1103/physrevd.109.072014. URL: http://dx.doi.org/10.1103/PhysRevD.109.072014.

[168] T2K Collaboration. *The T2K data release page*. Last accessed: 2024-08-25. URL: https://zenodo.org/communities/t2kexperiment.

[169] NOvA Collaboration. *The NOvA data release page*. Last accessed: 2024-08-25. URL: https://novaexperiment.fnal.gov/data-releases/.

[170] Durham University. *HEPData website*. Last accessed: 2024-08-25. URL: https://hepdata.net/.

[171] Stephen Bailey et al. *Data and Analysis Preservation, Recasting, and Reinterpretation*. 2022. arXiv: 2203.10057 [hep-ph]. URL: https://arxiv.org/abs/2203.10057.

[172] LHC Collaborations. *Forum on the Interpretation of the LHC Results for BSM studies*. Last accessed: 2024-08-22. URL: https://twiki.cern.ch/twiki/bin/view/LHCPhysics/InterpretingLHCresults.

[173] Kyle Cranmer et al. "Publishing statistical models: Getting the most out of particle physics experiments". In: *SciPost Physics* 12.1 (Jan. 2022). ISSN: 2542-4653. DOI: 10.21468/scipostphys.12.1.037. URL: http://dx.doi.org/10.21468/SciPostPhys.12.1.037.

[174] Jack Y. Araz et al. *Les Houches guide to reusable ML models in LHC analyses*. 2024. arXiv: 2312.14575 [hep-ph]. URL: https://arxiv.org/abs/2312.14575.

[175] R. Fine et al. *Data Preservation at MINERvA*. 2022. arXiv: 2009.04548 [hep-ex]. URL: https://arxiv.org/abs/2009.04548.